

A COMPUTATIONAL IMAGE-BASED GUIDANCE SYSTEM FOR PRECISION LAPAROSCOPY

A Dissertation Presented to
the Faculty of the Department of Computer Science
University of Houston

In Partial Fulfillment
of the Requirements for the Degree
Doctor of Philosophy

By
Toan B. Nguyen
December 2016

A COMPUTATIONAL IMAGE BASE GUIDANCE SYSTEM FOR PRECISION LAPAROSCOPY

Toan B. Nguyen

APPROVED:

Dr. Nikolaos V. Tsekos, Chairman
Dept. of Computer Science, University of Houston

Dr. Ioannis Pavlidis
Dept. of Computer Science, University of Houston

Dr. Ricardo Vilalta
Dept. of Computer Science, University of Houston

Dr. Marc Garbey
Center of Computational Surgery, Houston Methodist Hospital

Dean, College of Natural Sciences and Mathematics

Acknowledgment

This dissertation would not have been possible without the generous funding from the Vietnam Education Foundation (VEF) and the National Science Foundation's Industry/University Cooperative Research Centers program [NSF 1060222 IUCRC Center CYBHOR].

I would like to express my gratitude to Dr. Vo Van Toi for introducing me to the program of Computational Surgery sponsored by VEF. The memories and motivation from when I worked in the Department of Biomedical Engineering of Vietnam National University – International University have brought me this far.

I would also like to thank the University of Houston for providing the Competitive Scholarship and the Department of Computer Science for assisting me with paperwork and procedures.

The MR and CT scan images used in this dissertation would not have been available without the hard work of the colleagues at MITTE, Houston Methodist Hospital.

The advisory committee, consisting of Dr. Marc Garbey, Dr. Nikolaos Tsekos, Dr. Pavlidis Ioanis, and Dr. Ricardo Vilalta has been excellent at giving me valuable feedback throughout the duration of this dissertation.

I would also like to thank the people at the lab of Computational Surgery for their help and support.

I was able to complete this dissertation under the guidance of my supervisors, Dr. Marc Garbey and Dr. Brian Dunkin. Their critiques and opinions about my work and trust in my abilities shall never be forgotten; I am grateful for the support they have provided me in all these years.

Finally, I would like to dedicate this dissertation to people who mean more to me than my life – my father, mother, brother, wife, and soon-to-be-born baby. Their patience, love, support and guidance throughout my life has made me the person I am today.

A COMPUTATIONAL IMAGE-BASED GUIDANCE SYSTEM FOR PRECISION LAPAROSCOPY

An Abstract of a Dissertation

Presented to
the Faculty of the Department of Computer Science
University of Houston

In Partial Fulfillment
of the Requirements for the Degree
Doctor of Philosophy

By
Toan B. Nguyen
December 2016

Abstract

This dissertation presents our progress toward the goal of building a computational image-based guidance system for precision laparoscopy; in particular, laparoscopic liver resection.

As we aim to keep our working goal as simple as possible, we have focused on the most important questions of laparoscopy - predicting the new location of tumors and resection plane after a liver maneuver during surgery. Our approach was to build a mechanical model of the organ based on a pre-operative image and register it to intra-operative data. We proposed several practical and cost-effective methods to obtain the intra-operative data in the real procedure. We integrated all of them into a framework on which we could develop new techniques without redoing everything.

To test the system, we did an experiment with a porcine liver in a controlled setup: a wooden lever was used to elevate a part of the liver to access the posterior of the liver. We were able to confirm that our model has decent accuracy for tumor location (approximately 2 mm error) and resection plane (1% difference in remaining liver volume after resection). However, the overall shape of the liver and the fiducial markers still left a lot to be desired.

For further corrections to the model, we also developed an algorithm to reconstruct the 3D surface of the liver utilizing Smart Trocars, a new surgical instrument recognition system. The algorithm had been verified by an experiment on a plastic model using the laparoscopic

camera as a mean to obtain surface images. This method had millimetric accuracy provided the angle between two endoscope views is not too small.

In an effort to transit our research from porcine livers to human livers, in-vivo experiments had been conducted on cadavers. From those studies, we found a new method that used a high-frequency ventilator to eliminate respiratory motion.

The framework showed the potential to work on real organs in clinical settings. Hence, the studies on cadavers needed to be continued to improve those techniques and complete the guidance system.

Contents

I. Motivation and background	1
1. Introduction.....	2
1.1 Laparoscopic surgery.....	2
1.2 Motivation	4
1.3 Dissertation overview	6
2. Background	8
2.1 Anatomy of the liver.....	9
2.2 Liver segmentation - Couinard system.....	13
2.3 Liver resection	15
2.4 Finite elasticity theory	20
2.5 Biomechanical properties of liver.....	28
2.6 Finite-element for finite elasticity	30
2.7 Image segmentation.....	33
2.8 Literature review.....	38
2.9 Dissertation proposal	41
II. Developing of the image-based guidance system	42
3. Building the framework	43

3.1	Main workflow of the framework	43
3.2	Description of the components	46
4.	Validation of the mechanics modeling framework	54
4.1	Problem statement and method.....	55
4.2	Experimental setup	57
4.3	Model and simulation	61
4.4	Validation and discussion	68
4.5	Conclusion	77
5.	New method for going from 2D-endoscope to 3D-acquisition of surface landmarks by software.....	78
5.1	State of the art.....	79
5.2	Smart Trocar	82
5.3	Method.....	87
5.4	Verification experiment.....	91
5.5	In vivo experiment and discussion	96
5.6	Discussion.....	100
6.	Transition to human liver	102
6.1	Experiments on cadavers	102
6.2	New method for respiratory motion correction	112

III. Dissertation review	116
7. Conclusion and future work	117
7.1 Validation of the tissue mechanics	118
7.2 Liver surface reconstruction using Smart Trocars.....	120
7.3 Future works	121
7.4 List of publications	122
Bibliography	123

List of figures

Figure I.1 Laparoscopic surgery (image taken from [3]).....	3
Figure I.2 Liver anatomy (image taken from [6]).....	9
Figure I.3 Surface and bed of liver (image taken from [7]).....	10
Figure I.4 Vascular supply (image taken from [6])	11
Figure I.5 Liver segmented by portal and hepatic veins (figure take from [8]).....	13
Figure I.6 Liver segmentation (image taken from [8])	16
Figure I.7 Clamping of right portal vein and right hepatic artery (image taken from [8])	18
Figure I.8 Body in reference and current configuration	21
Figure I.9 A Closed Active Contour Model (image taken from [9])	34
Figure II.1 Workflow of the framework	45
Figure II.2 Run the snake method to segment the liver from the scans.....	47
Figure II.3 Guide user interface for manual method.....	48
Figure II.4 Apply anisotropic filter to the image to reduce noise	49
Figure II.5 Apply white top-hat transform to the image	49
Figure II.6 Apply adaptive threshold with Otsu's method	49
Figure II.7 Apply new mask which comes from erosion transform of the old mask	50
Figure II.8 Do open operation with ball structure to remove small objects	50
Figure II.9 Tumor (black) location changes after lifting with a surgical tool.....	55
Figure II.10 Resection plane (green) changes after lifting with a surgical tool.....	55

Figure II.11 X-ray image of the liver showing guide wire, simulated tumor, and vessels	58
Figure II.12 Porcine liver in position A - stays flat down	58
Figure II.13 Porcine liver in position B - elevated. (a) Top down view (b) Side view	59
Figure II.14 Liver parenchyma and wire changes between the flat (a) and elevated (b). Position changes are visualized using the imaging modalities.	61
Figure II.15 Segmentation results of (a) fake simulated tumor (b) guide wire (c) liver boundary (d) 2D-top view of tumor (green), guide wire (red) inside the liver (blue).	63
Figure II.16 Geometry of liver's simulation in COMSOL (a) without liver (b) with liver	64
Figure II.17 Stage 1 of the simulation: Liver shape changes from A to B'	66
Figure II.18 Stage 2 of the simulation: Liver shape changes from B' to B	67
Figure II.19 Tumor centroid, guide wire, and liver upper curve comparison on same 2D- cut in position B (a) linear-elastic model and (b) hyper-elastic model.....	69
Figure II.20 Tumor-centroid error based on mesh type: Linear-elastic model vs. hyper- elastic model	71
Figure II.21 Tumor-centroid error based on mesh type: Young's modulus (high vs. low)	72
Figure II.22 Tumor-centroid error based on mesh type: Poisson's ratio (high vs. low)....	72
Figure II.23 Tumor-centroid error based on mesh type: Friction (high vs. low).....	73
Figure II.24 Resection plane in (a) position A (b) position B using simulated model (c) position B using CT images	75
Figure II.25 Concept of the Smart Trocar.....	83

Figure II.26 Smart Trocar prototype with camera attached and colored marker	84
Figure II.27 Smart Trocar can obtain its position in 3d-coordinate space by capturing trajectory of the crosses through the camera.....	85
Figure II.28 Setup of the concept.....	87
Figure II.29 Successive bijective transformations between the plane Ω and the image acquired by the laparoscope: first an homothety with scaling factor ξ to relate pixel size to physical size and then a rotation.	88
Figure II.30 Experiment setup using a clamp to hold the laparoscope. In right corner is 3D-printed model having the shape of a half-sphere	91
Figure II.31 The laparoscope took images of the model in 4 positions.....	93
Figure II.32 Six interest points on the model surface needs to be calculated	94
Figure II.33 Liver position and landmarks at (a) full exhalation and (b) full inhalation ...	96
Figure II.34 Time dependence of distance between two markers (purple and blue in Figure II.33) in (a) x-direction and (b) in y-direction.....	98
Figure II.35 Location of Smart Trocars on the patient abdomen.....	104
Figure II.36 Ventilator machine's display	106
Figure II.37 Grid of markers on liver surface	107
Figure II.38 Two laparoscopic cameras were used at the same time.....	107
Figure II.39 The Smart Trocars were set up to record the trajectories and location of the instruments and the camera.....	108
Figure II.40 Fake tumors and stent were deployed into the liver	108
Figure II.41 The liver lift with a wooden stick	109

Figure II.42 CT scan of the cadaver's liver	110
Figure II.43 Simulation in COMSOL software	111
Figure II.44 Markers on the liver surface were tracked with software.....	113
Figure II.45 Trajectory of one marker: High-frequency vesus normal ventilator	114
Figure II.46 Marker displacement versus respiratory rate in case of HFV.....	114

List of table

Table 1 Segments to be removed in different types of liver resection.....	17
Table 2 State of the art for surface imaging system.....	81
Table 3 Result of experiment on rigid model	95
Table 4 Effect of perturbation on the results from the verification experiment reported in the previous section.....	99

Part I

Motivation and background

Chapter 1

Introduction

1.1 Laparoscopic surgery

In traditional open surgery, to perform operations inside the abdomen, surgeons must make a large incision to insert the instruments, visualizing the procedure through the incision. Depending on the type of surgery, the incision can occur in many places on the outer wall of the abdominal. An average incision is approximately 8 inches long. These incisions can cause significant scarring which slowly heal, prolonging the patient's hospital stay and hinder them from getting back to their daily activities [1].

Laparoscopic surgery - also referred to as minimally invasive surgery (MIS) - is a modern surgical technique in which small incisions are made in the abdominal wall, and plastic tubes called ports are placed through these incisions. The laparoscope and other instruments can be pushed through those ports, allowing the surgeon to see and operate inside the patient's abdomen and pelvis [2].

This technique can help to avoid large incisions used in traditional open surgery. Therefore, it can reduce hemorrhaging and pain. Smaller incision also leads to less postoperative scarring and faster recovery times.

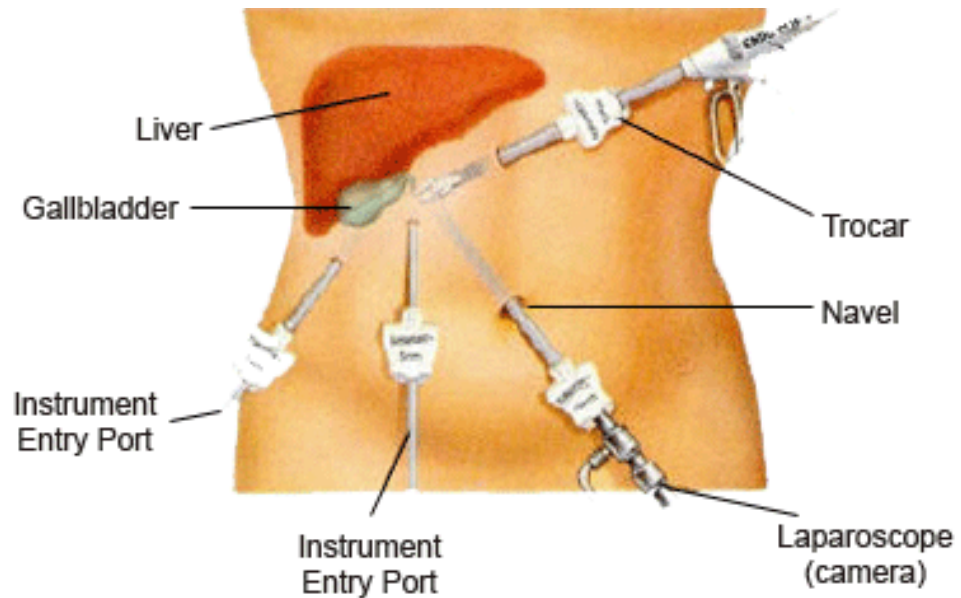


Figure I.1 Laparoscopic surgery (image taken from [3])

Laparoscopic surgery is now one of the most common surgical procedures performed in many parts of the world.

1.2 Motivation

The motivation comes from personal and technical aspects.

I am originally from Vietnam. Liver disease has a high prevalence in Vietnam due to chronic infection with hepatitis viruses and high consumption of alcohol. Chronic infection with hepatitis viruses, including hepatitis C virus (HCV), and hepatitis B virus (HBV) can lead to liver cancer and cirrhosis (liver damage). If it is not treated well, the risk of liver cancer considerably increases. When long-term high-consumption of alcohol is combined with viral infections, the risk of cancer and cirrhosis can be doubled. A nationwide study found that liver cancer is the most common cause of cancer death in Vietnam [29]. In America, liver cancer is the 10th most common cancer, the 5th most common cause of cancer death among men, and the 8th most common cause of cancer death among women [4]. Contributing to research which helps liver-cancer treatment feels like a natural way to give back to my original country and the country where I have been conducting this study.

From a technical aspect, laparoscopic solid-organ tissue resections are challenging. In open liver resection, most of the abdomen is exposed with the incision. A trained surgeon can quickly identify, dissect and divide the veins and arteries with his/her eyes. In laparoscopic liver resection, the surgeon can only look at the limited 2D-view from the laparoscope and operate through the trocars. Therefore, extensive pre-operative imaging must be performed before the surgery so that the surgeon can plan out the procedure. This works well until the actual resection begins and the coordinates in places are lost due to the

deformation of the liver. Traditionally, accuracy is restored by rescanning the patient – a difficult task in the middle of complicated surgery. Hence, there exists a need for dynamic, real-time tracking and recognition of internal structures and target tissues during a minimally invasive procedure.

Working on a computational image-based guidance system for precision laparoscopy, which first target is laparoscopic liver resection (LLR), fulfills both of the aspects. This system can help to increase favorable outcomes of minimally invasive surgery and thus support treatment of liver cancer in my country and America.

1.3 Dissertation overview

The work in this dissertation focuses on the development of the navigation system based on the finite-element models of the liver for accurate simulation of organ deformation. The model is registered to the intra-operatively data by using many overlapping techniques which will be represented in the next chapters.

This dissertation is divided into three major parts, each consisting of a set of chapters focused on a particular area of work. An overview of the parts and chapters in this dissertation is provided here, highlighting the contributions made by this body of work to the field of the surgical navigation system.

Part I: Motivation and Background

Chapter 1 provides introduction and motivation of the work in this dissertation
Chapter 2 presents background information on the anatomy of the liver, liver resection, the mechanic's theory and basic modeling framework used to predict liver deformation. The chapter concludes with a review of the literature in liver biomechanics modeling and describes the approach taken in this dissertation to address the problems in the literature.

Part II: Developing of the image-based guidance system

Chapter 3 establishes the framework for the system and its components.
Chapter 4 describes the work done to build a working validation of the model. It also gives detail about the experiment on a porcine liver-explant model and the simulation coming from it.

Chapter 5 introduces the new method of reconstructing the liver's surface using only a 2D-laparoscope and Smart Trocars.

Chapter 6 is about the transition from the porcine liver to the human liver. The experiments on cadavers are presented here along with a new finding about how to eliminate respiratory motion with the high-frequency ventilator.

Part III: Dissertation review

Chapter 7 concludes the dissertation by giving summaries about the work having done and indicating what needs to do in the future.

Chapter 2

Background

This chapter provides the necessary background information to develop the guidance system. Section 2.1 provides a description of the anatomy of the liver. It is followed by a classic definition of liver segmentation based on functional units of the liver in Section 2.2. Section 2.3 continues by explaining the type of liver resections and how our system can contribute to the surgical navigation field. Section 2.4, 2.5, 2.6 present the basic math of the computational model: the finite elasticity theory, biomechanical properties of the liver and finite-element method. Section 2.7 describes the image-processing technique to segment the liver from medical images to build the mesh for the model. Section 2.8 provides literature review about this dissertation's topic. Finally, Section 2.9 gives the conclusion about the contribution of this dissertation.

2.1 Anatomy of the liver

An understanding of the liver organization is critical for the mechanical model development. The liver is an organ of the digestive system, the biggest organ in the human body and accounts for approximately 2% of adult body weight, 5% of children body weight. The liver is fixed just under the diaphragm, in the top right portion of the abdominal cavity but protected by thorax skeleton and relates to chest more than abdomen [5].

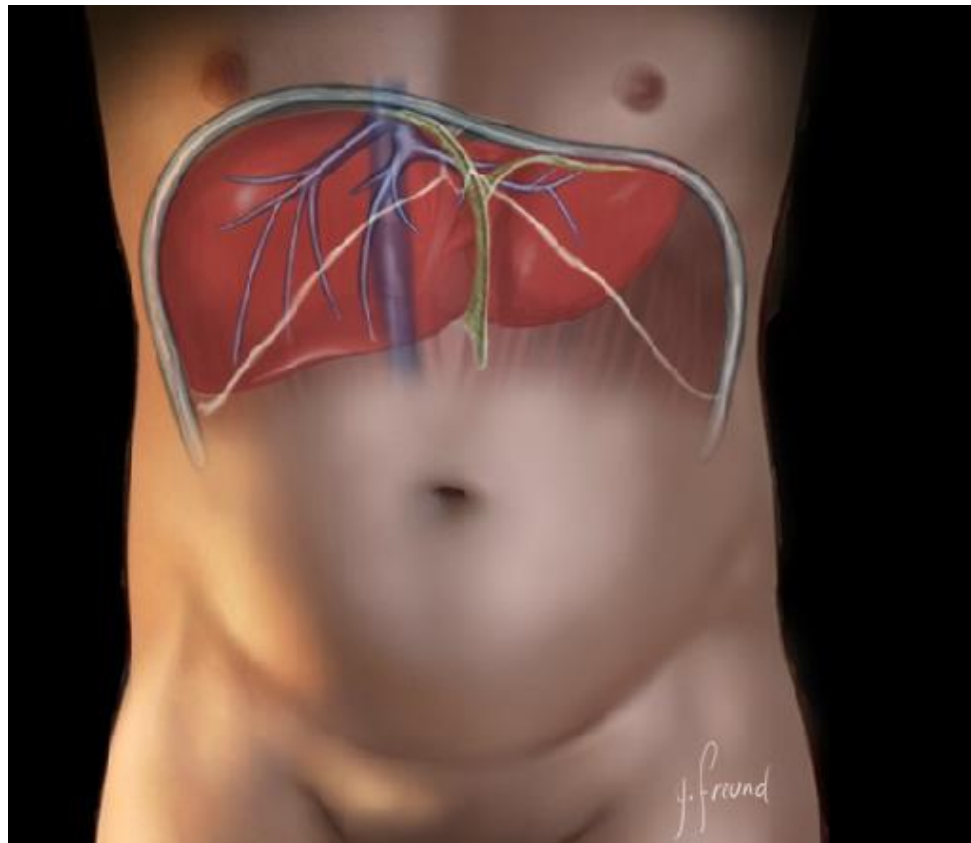


Figure I.2 Liver anatomy (image taken from [6]).

It is settled to the abdominal wall by those ligaments: the left and right triangular ligaments posteriorly, the left and right coronary ligaments and the falciform ligament, and located below the costal margin in the right subphrenic part.

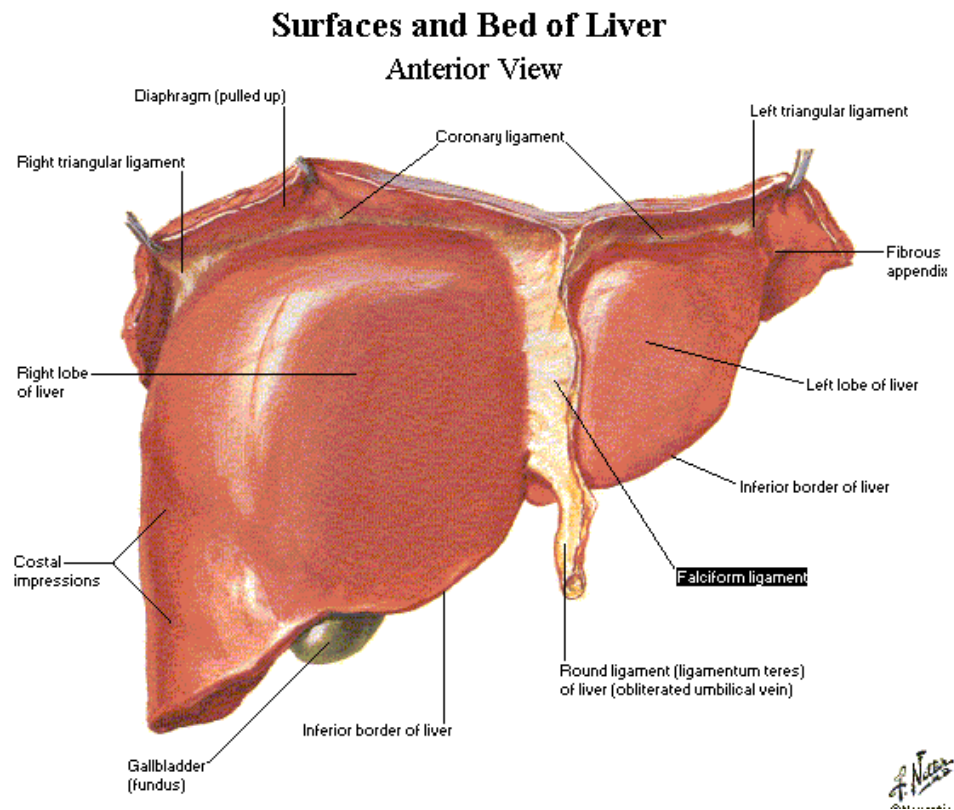


Figure 1.3 Surface and bed of liver (image taken from [7]).

It is placed directly antecedent to the inferior vena cava (IVC), attached to the IVC by the three main hepatic veins.

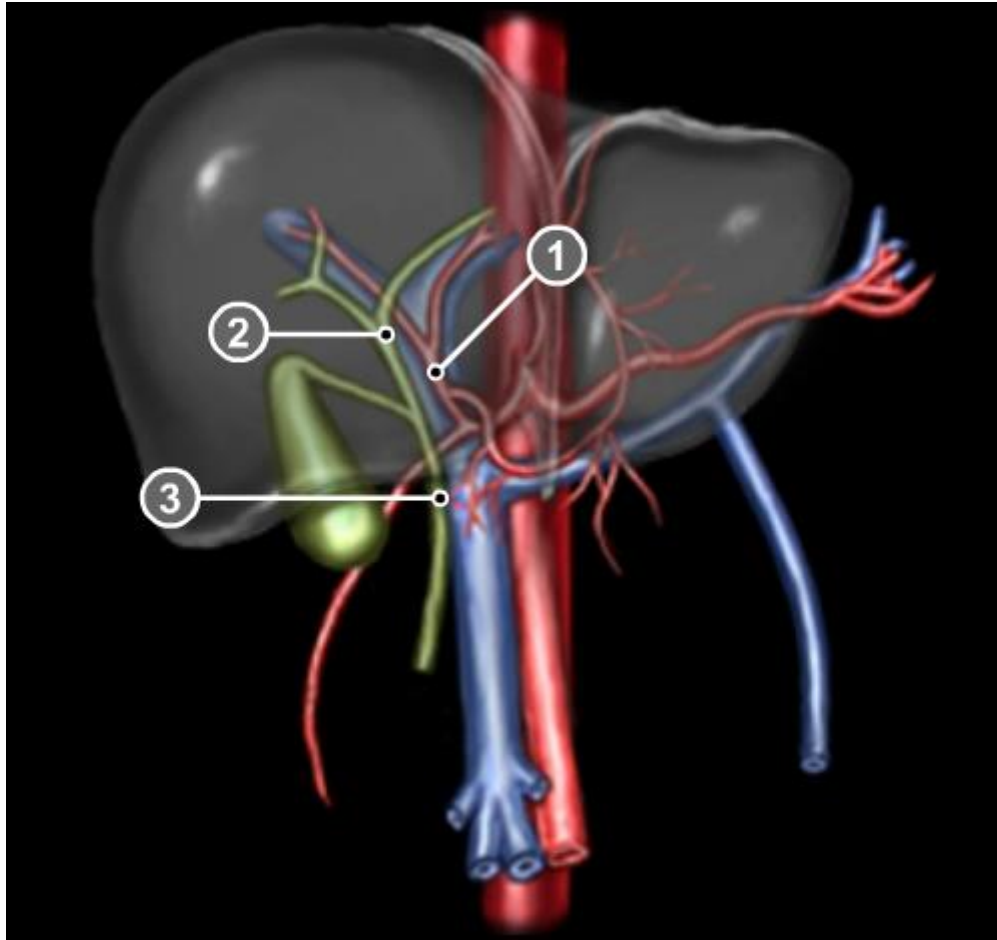


Figure I.4 Vascular supply (image taken from [6])
1. Hepatic artery 2. Portal vein 3. Common hepatic duct

The liver is supplied by the portal vein and the hepatic artery that drains blood from abdominal organs to the liver. The bile is provided by the common hepatic duct, which is the junction of the left hepatic duct and the right hepatic duct in the porta hepatis. The portal vein, the hepatic artery, and the common bile duct are parts of the porta hepatis which is attached to the liver on its inferior surface.

The liver is an exocrine gland which produces and discharges bile to pour into the duodenum, but it gets involved in many essential functions of the body such as glucose, protein, lipoprotein metabolism, especially glycogen storage,

regulation of blood sugar to eliminate poisons and supernumerary medicines out of the body through bile duct.

The liver is reddish-brown, shiny, and slippery. Although its density is relatively thick, it is easy to be crushed and broken when injured. Also, when cut, it bleeds very much. For dead people, the liver weighs 1.5 kg. For live people, the liver weighs about 2.3 kg. The liver has an average width of 28 cm, anterior - posterior surfaces of about 18 cm and the average height of 8 cm.

2.2 Liver segmentation - Couinaud system

The Couinaud classification of liver anatomy is the most commonly used segmentation of the liver. It splits the liver into eight segments that function independently. Each unit has its own vascular inflow, outflow, and biliary drainage.

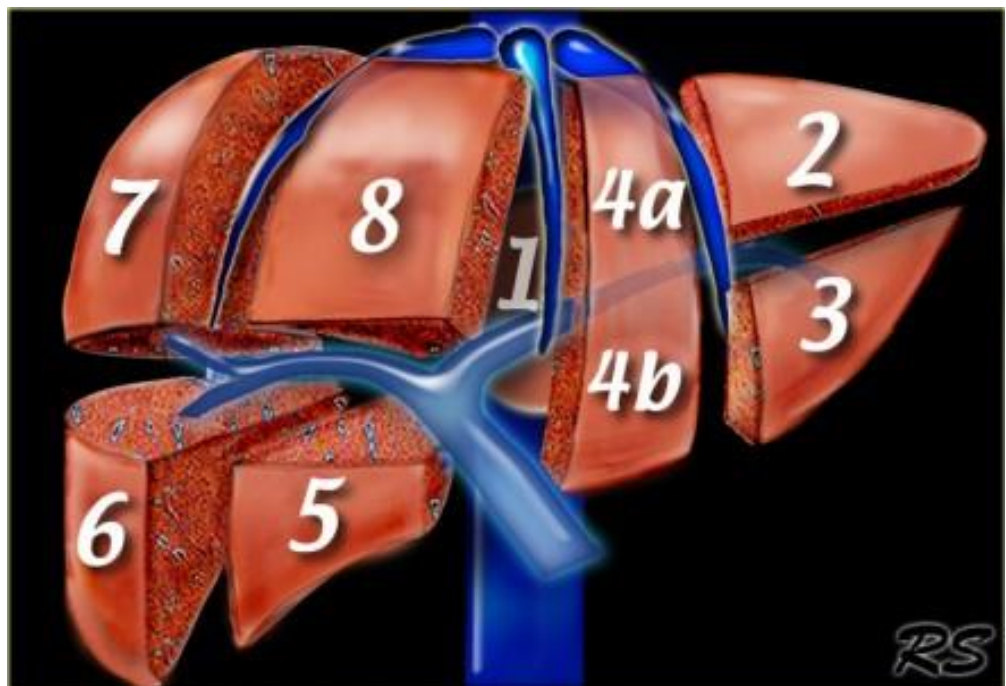


Figure I.5 Liver segmented by portal and hepatic veins (figure take from [8])

Middle hepatic vein separates the liver into left and right lobes from the IVC to the gallbladder. The right lobe is divided by the right hepatic vein into anterior and posterior segments. The left lobe is divided by the left hepatic vein into medial and lateral parts. Portal vein separates the liver into upper and lower

segments. The left and right portal veins grow up and down into the center of each segment. The segments are numbered from 1 to 8 as in Figure I.5.

To remove a segment of the liver, parenchymal division follows the inter-lobar gap while keeping slightly to the right of the middle hepatic vein. So the middle hepatic vein needs to be localized to make the right resection, and the model should show every segment of the liver based on veins' positions.

2.3 Liver resection

The technique of liver resection has profited recently from an improved knowledge of both surgical and radiological liver anatomy. Nowadays, it is possible to resect any single or multiple segments of the liver, using methods to decrease blood loss during surgery and new procedures to divide liver parenchyma. New research in intra-operative monitoring and general anesthesia have also reduced operative risks.

Nevertheless, significant intra-operative or postoperative complications related to the surgical procedure directly can still occur. Therefore, following a step-by-step technique is essential to minimize these risks [6].

2.3.1 *Types of liver resection:*

The types of liver resection are based on Couinaud's classification. Right liver resection and left liver resection are the most commonly executed procedures. Any procedure that involves the resection of three or more segments is called a major procedure. In left liver resection, segments 2, 3, and 4 are cut out. It can extend to involve segment 1, segment 5, segment 8. In right liver resection, segments 5, 6, 7, and 8 are extracted. It can extend to involve segment 4 or segment 1, or both. The last case is one of the largest liver resections, as only the right posterior lateral segment is left untouched.

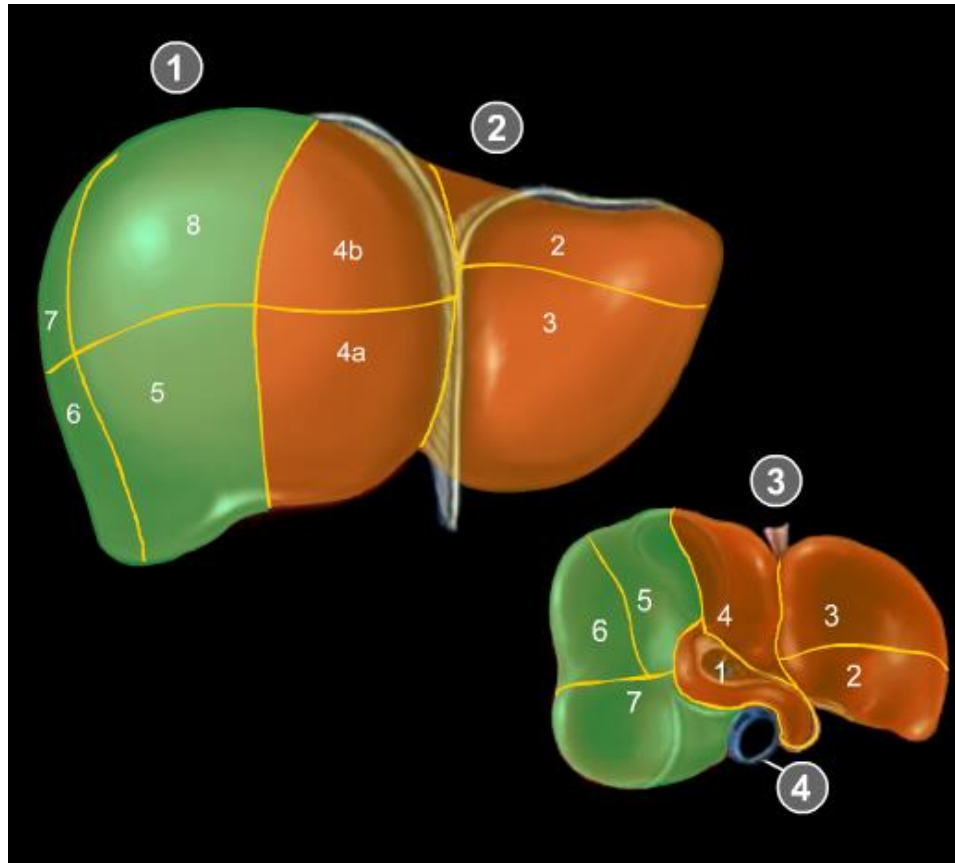


Figure I.6 Liver segmentation (image taken from [8])
 1. Right liver 2. Left liver 3. Caudal surface 4. IVC (inferior vena cava)

In minor liver resection, only one liver segment or two adjacent segments are removed. Each liver segment may be resected separately or in combination with an adjacent segment. Bisegmentectomy 2 and 3 corresponds to the left lobectomy. Resection of posterior segments is harder than resection of anterior segments (3, anterior 4, 5).

Segment	1	2	3	4	5	6	7	8
Right liver resection	E			E	R	R	R	R
Left liver resection	E	R	R	R	E			E
Bisegmentectomy		R	R					

***R**: removed segments **E**: extendable removed segments*

Table 1 Segments to be removed in different types of liver resection

In liver surgery, the key point is controlling the portal branch, hepatic vein, branches of the hepatic artery, and hepatic duct. Therefore, liver anatomy and vascular supply need to be understood.

Therefore, landmarks are required on the portal vein and its branches for the segmentation model. The number and position of the markers might depend on which type of liver resection of the application.

2.3.2 Open liver resection versus laparoscopic liver resection

In open liver resection, most of the liver is exposed with the incision. A trained surgeon can quickly identify, dissect, and divide the veins and arteries with his eyes. The need for navigation systems might only come from the difficulty in determining the left lobe and the right lobe as veins go under the surface of the liver. Even so, the surgeon can still clamp the portal vein and the hepatic artery of one liver side. It results almost instantaneously discoloration of the corresponding side of the liver and demarcation of both lobes of the liver. The surgeon then can proceed to parenchymal division follows the differentiation. Therefore, the navigation system is not useful in open surgery.



Figure I.7 Clamping of right portal vein and right hepatic artery (image taken from [8]).

Laparoscopic liver resections (LLR) are replacing open liver resection with over 3000 cases performed worldwide for benign disease, malignancy, and hepatectomy [30]. While minimally invasive surgery has been welcomed in other fields, there are several difficulties to make LLR widespread. Mobilization and transection techniques in open resection do not work the same in LLR. There is concern about not being able to control hemorrhaging and gas embolism. In spite of that, the technological advances in laparoscopic devices, radiologic imaging, and patient demand have made the number of LLR cases increase recently.

In laparoscopic liver resection, the field of view is limited. The current navigation system for this kind of liver resection is video feedback which is a 2D-view. Moreover, the surgeon cannot contact directly with the liver. Some of the methods to identify and separate the veins and arteries in open surgery cannot be applied here including clamping techniques. Therefore, a 3D-navigation system is urgently needed for laparoscopic liver resection. It will help the surgeon gain the whole view of the organ and its surroundings, the sense of depth, the inner structure of the liver, and essential features needed for laparoscopic liver resection.

2.4 Finite elasticity theory

With the liver anatomy and resection described, this section introduces the mechanical modeling of liver tissue. This section first outlines the kinematics that describes the equations relating strain tensors to displacement gradient [11, 12]. We then present the stress equilibrium equation for a linear and hyper-elastic material. These equations constitute the connection between stress and strain of the material. We conclude with a discussion on the computational implementation of these mechanical models on commercial software.

2.4.1 Kinematics

For the coordinates system, we consider the body, Ω_0 has been subjected to a deformation now in a deformed state, Ω_x . We refer the current state of the body as the current configuration and the initial, non-deformed state, as the reference configuration. For these two configurations, two types of coordinate systems are used to analyze stresses and strains:

Material coordinates (X_1, X_2, X_3) are used to link each material point from the reference configuration to the deformed configuration. When the body deforms, the material coordinate axes deform in a similar manner. Hence the coordinate values of a material point do not change during the deformation. This coordinate system is called a Lagrangian description.

Spatial coordinates (x_1, x_2, x_3) are used to link the material point to a specific global position in space. As the body deforms, this point can be associated with

a different material point. A spatial coordinate system is a fixed coordinate system in space. This coordinate system is often called a Eulerian description.

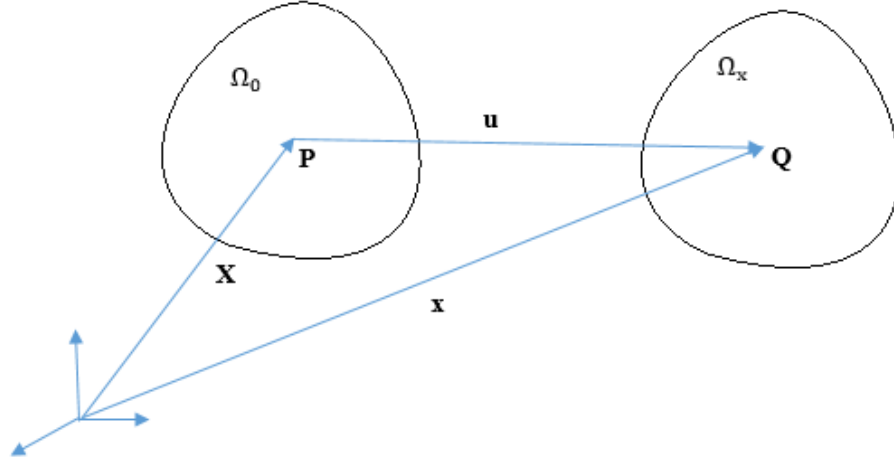


*Figure I.8 Body in reference and current configuration
(image reproduced from [10]).*

The measure of strain requires a relationship between the material coordinates of the material points in the reference configuration and the spatial coordinates of material points in a deformed body. Let the position of material points in the current configuration, x , is functions of their position in reference configuration, X . The deformation can be represented by a mapping $f: \Omega_0 \mapsto \Omega_x$ where $x = f(X)$.

Consider a line element dX in the reference configuration being deformed into dx in the current configuration. Then a deformation gradient tensor, F , relating the line element in the non-deformed state to the line element in the current state is defined by the relationship $dx = FdX$, where

$$F = \frac{\partial x}{\partial y} \quad (2.1)$$

The deformation gradient tensor also responded for the mapping of differential volumes and areas. It is expressed as

$$dv = JdV \quad (2.2)$$

where J is the Jacobian of the deformation gradient tensor.

The entire deformation, including the strain and rigid body motion, is represented by the deformation gradient tensor. It can be decomposed according to the polar decomposition of the tensor as $F = RU$ where R is an orthogonal rotation tensor, and U is a symmetric tensor, known as the right stretch tensor, representing the material strain independent of the rigid body rotation. Because U is a positive and symmetric tensor, there exists a basis in which U is diagonal. These are the principal direction of U and by definition, the positive diagonal components $\lambda_1, \lambda_2, \lambda_3$ of U in the principal axes called the principal values of U, presenting the principal stretches. In continuum mechanics, it is usually good to use rotation-independent measures of deformation since a pure rotation should not induce any stresses in a deformable body.

We derive another tensor that is independent of the rigid body rotation, the right Cauchy-Green tensor, C, defined as:

$$\begin{aligned}
\mathbf{C} &= \mathbf{F}^T \mathbf{F} \\
&= \mathbf{R} \mathbf{U}^T \mathbf{R} \mathbf{U} \\
&= \mathbf{U}^T \mathbf{R}^T \mathbf{R} \mathbf{U} \\
&= \mathbf{U}^T \mathbf{U}
\end{aligned} \tag{2.3}$$

In three-dimension, \mathbf{C} is a 3 x 3 matrix and possesses 3 principal invariants under coordinate change:

$$I_1 = \text{tr}(\mathbf{C}) = \lambda_1^2 + \lambda_2^2 + \lambda_3^2 \tag{2.4}$$

$$I_2 = \frac{1}{2} [(\text{tr} \mathbf{C})^2 - \text{tr} \mathbf{C}^2] = \lambda_1^2 \lambda_2^2 + \lambda_2^2 \lambda_3^2 + \lambda_3^2 \lambda_1^2 \tag{2.5}$$

$$I_3 = \det \mathbf{C} = \lambda_1^2 \lambda_2^2 \lambda_3^2 = J^2 \tag{2.6}$$

They are usually used to express strain energy density functions. When there is no deformation or motion, the deformation gradient tensor will be equal to the identity tensor \mathbf{I} . Therefore, the right Cauchy-Green deformation tensor is as well. To get a strain tensor such that no motion or deformation yields the zero tensor, 0, the Green Strain tensor, \mathbf{E} , was introduced, satisfying this property:

$$\mathbf{E} = \frac{1}{2} (\mathbf{C} - \mathbf{I}) \tag{2.7}$$

2.4.2 Stress equilibrium

The equilibrium equations are derived from the following three conservation laws:

1. Conservation of mass indicates that the mass of the body is the same in Ω_0 and Ω_x . This creates a relationship between the mass density, ρ_0 , in the initial state and the mass density, ρ , in the deformed state:

$$\rho_0 = J\rho; J = \det(F) \quad (2.8)$$

2. Conservation of linear momentum indicates that the time rate of change of linear momentum must balance all the forces that act on the body. Consider an equilibrium state of a body under the body force, \mathbf{b} , per unit of volume and the traction forces, \mathbf{t} , per unit area, one can establish the momentum balance:

$$\int_a \mathbf{t} da + \int_v \mathbf{b} dv = 0 \quad (2.9)$$

Using the Gauss theorem and definition of the Cauchy stress tensor, σ , we can write

$$\int_v (\nabla \cdot \sigma + \mathbf{b}) dv = 0 \quad (2.10)$$

3. Conservation of angular momentum indicates that the time rate of change of momentum of the body must balance the applied moments.

The Cauchy stress tensor refers to the force measured per unit area in the deformed configuration. Another measurement of stress include P and S , respectively the 1st and 2nd Piola-Kirchhoff stress tensor defined by:

$$P = J\sigma F^{-T} \quad (2.11)$$

$$S = JF^{-1}\sigma F^{-T} \quad (2.12)$$

At this equilibrium state, if the body undergoes an arbitrary, small, virtual displacement $\delta \mathbf{u}$ (not caused by prescribed external forces), the equation 2.9 can be rewritten as

$$\delta W = - \int_S \mathbf{t} \cdot \delta \mathbf{u} ds + \int_v \mathbf{b} \delta \mathbf{u} dv = 0 \quad (2.13)$$

2.4.3 Constitutive equation

In the previous section, the stress equilibrium equations and the kinematic equations have been expressed. Therefore, a mathematical relationship between strains and the stresses must be established. This relationship is called constitutive relation.

The form of the constitutive relation is not the same for every material. It is material-behavior specific. Hence, it may be necessary to develop more than one constitutive relation for material if there is an interest in different conditions. A class of constitutive relations can be theorized in which the stress is a function of the deformation gradient tensor $\sigma = f(F)$, where F are the components of the deformation gradient tensor, σ , represent components of a

stress tensor (Cauchy stress) and f are the functions. This formulation represents a behavior known as elasticity. For the liver model, we only pay attention to linear elastic and hyper-elastic material.

Linear elasticity has assumptions: the deformations are small, and the relationships between the components of stress and strain are linear. In direct tensor form, the equations for this kind of material are

$$\nabla \cdot \delta + F = \rho \ddot{u} \quad (2.14)$$

$$\varepsilon = \frac{1}{2} [\nabla u + (\nabla u)^T] \quad (2.15)$$

$$\delta = \mathbf{C} \varepsilon \quad (2.16)$$

where δ is the stress tensor, ε is the strain tensor, u is the displacement vector, \mathbf{C} is the fourth-order stiffness tensor, F is the body force per unit volume, and ρ is the mass density.

Hyper-elasticity is a special case of an elastic material which the stress –strain relationship derives from a strain energy density function, W . Stresses are calculated by differentiating the strain energy function on a measure of deformation of strain:

$$S = \frac{\partial W(E)}{\partial E} \quad (2.17)$$

Additionally, if the material's characteristic is isotropy then the strain energy function, W , may be expressed regarding the principal invariants:

$$W = W(E) = W(I_1, I_2, I_3) \quad (2.18)$$

To model the behavior the liver, we used the Neo-Hookean model which has the strain energy density function:

$$W = C_1(\bar{I}_1 - 3) + D_1(J - 1)^2 \quad (2.19)$$

where $\bar{I}_1 = J^{2/3}I_1$

C_1 and D_1 are the material constants expressed in Pa. For consistency with linear elasticity,

$$C_1 = \frac{\mu}{2} \quad (2.20)$$

$$D_1 = \frac{\kappa}{2} \quad (2.21)$$

where μ is the shear modulus and κ is the bulk modulus. These parameters are fit by performing tension compression tests. The values of these will be discussed in the next section.

2.5 Biomechanical properties of liver

The organization, composition, and structure of the liver directly contribute to the mechanical function of it. Although measurement of soft tissue mechanical properties is an established research area, the variation in mechanical properties of the liver across individuals offers a significant challenge in developing anatomically realistic models of the liver. Moreover, soft biological organs have complex mechanical behavior including the nonlinear, anisotropic, inhomogeneous, and rate-dependent response. To build a surgical simulation, ideally, we need to measure the liver *in vivo*. However, the current efforts are either intended at employing animal models such as pigs which have essential differences in anatomy and tissue consistency compared to humans [13, 33-35], or acquiring *ex vivo* properties [27, 31, 32], which are mostly different from *in vivo* conditions.

In *ex vivo* techniques, liver samples are extracted and tested with various devices and procedures such as dynamic loading tests or stress relaxation tests. Still, the act of extraction changes liver conditions drastically from factors such as hydration, temperature, loss of blood supply, and break down of proteins. Besides, the sample has different boundary conditions from *in vivo* states.

In *in vivo* techniques, several experimental devices have been specifically developed to acquire biomechanical properties of soft tissues under various conditions: tissue elongation, indentation, puncture forces, rotary shear, tissue grasping, and tissue cutting.

The use of human cadavers is a safe alternative to live human experiments. However, depending on the time of preservation, the cadaver liver loses the elasticity and consistency characteristic of a fresh human liver. Therefore, it is essential to use of fresh, unfrozen cadavers.

From these studies, we can conclude that fresh human cadaver liver properties are much closer to in vivo mechanical properties of humans than porcine tissues. The mean elastic modulus of a human liver can be computed to be around 7 kPa [36], while it is about 6 kPa [14] on fresh human cadavers compared to 13 kPa for a pig liver [34].

Nevertheless, as will be outlined in the following section, previous studies show promise in the use of the finite-element method to predict liver deformation.

2.6 Finite-element for finite elasticity

Differential equations 2.9 described in Section 2.4.2 are nonlinear and do not have analytical solutions. We solve these partial-differential equations in their weak form in equation 2.13 by using the finite-element method. This section presents the finite-element technique that was used in simulating liver mechanics.

Consider a set of nonlinear-differential equations, $A(u)$, where u is a set of unknown functions; that satisfies the following equations in a domain

$$A(u) = 0 \quad (2.22)$$

A set of boundary conditions, $B(u)$, are related to differential equations on a boundary Γ of the domain Ω represented as

$$B(u) = 0 \quad (2.23)$$

The finite-element technique approximates the unknown function as

$$u \approx \hat{u} = \Phi_n \hat{u}_n \quad (2.24)$$

where \hat{u}_n are values of u at n points in Ω and Φ_n are called shape functions, used to approximate u . The shape functions are typically defined locally for each element. The next step is to express the set of differential equations in an integral form so the equations can be satisfied element by element. There are two methods available to obtain the integral form - the variational method and the weighted-residuals method.

2.6.1 Weighted residuals method

The set of differential equations, (2.22) and (2.23), can be rewritten in an integral form as

$$\int_{\Omega} v^T A(u) d\Omega = 0 \quad (2.25)$$

$$\int_{\Omega} v^T B(u) d\Omega = 0 \quad (2.26)$$

where v is a set of arbitrary functions same. This integral form guarantees that the set of equations (2.13) are satisfied as long as equation (2.26) is satisfied for all functions v .

While u was approximated by equation (2.25), v is approximated by

$$v \approx \hat{v} = \omega_n \hat{v}_n \quad (2.27)$$

Substituting equations (2.27) and (2.24) into equation (2.25), (2.26) gives

$$\int_{\Omega} \omega_n \hat{v}_n^T A(\Phi_n \hat{u}_n) d\Omega = 0 \quad (2.28)$$

$$\int_{\Gamma} \omega_n \hat{v}_n^T B(\Phi_n \hat{u}_n) d\Gamma = 0 \quad (2.29)$$

Since \hat{v}_n are arbitrary, the only unknown is the original set, u . Therefore the integral form of the original set of differential equations (2.25) and (2.26) is

$$\hat{v}_n^T \int_{\Omega} \omega_n A(\Phi_n \hat{u}_n) d\Omega = 0 \quad (2.30)$$

$$\hat{v}_n^T \int_{\Gamma} \omega_n B(\Phi_n \hat{u}_n) d\Gamma = 0 \quad (2.31)$$

2.6.2 Additional constraints - Lagrange Multipliers

A set of additional constraints may be necessary to add to equation (2.30-2.31).

These constraints are usually added to the integral formulation via a Lagrangian multiplier formulation. Consider an additional set of differential equations constraining equation (2.25) in the domain Ω which is given by

$$C(u) = 0 \quad (2.32)$$

Equation (2.30) now has an additional integral to incorporate the constraints in equation (2.32)

$$\int_{\Omega} \omega_n A(\Phi_n \hat{u}_n) d\Omega + \int_{\Omega} \lambda^T C(u) = 0 \quad (2.33)$$

where λ is a set of independent variables in the domain Ω called Lagrange multipliers

2.7 Image segmentation

This section presents an introduction for image segmentation. The process of segmentation is to split the image into meaningful parts. The result of image segmentation is a set of contours extracted from the image or a set of segments spread over the entire image. Each of the pixels in a region has the similar characteristics such as intensity, color, or texture. This is a necessary initial step for image processing processes such as detection, tracking, shape analysis, and object recognition. When applied to a series of images, typical in medical scans, the resulting segments can be used to create a 3D-reconstruction.

The description below is mainly based on the books by Gonzalez and Woods [17], Blake & Isard [15], and Lankton [18]. We provide the mathematical background to perform active contour model and then describe the particular active contour model developed by Lankton that we implemented to perform liver-image segmentation.

2.7.1 *Active contour models*

Active contour models provide one of the tools to proceed image segmentation. Active contour models are often called snakes because they have the sharp that slithers across images. It is a variational method performing energy minimization on curves that deform to fit the image (see Figure I.9).

Active contour models are typically driven by a potential energy generated by processing the image data, and this energy is minimized by iterative gradient descent. Also, other energy sources can be implemented such as internal forces

producing tension and stiffness, or external forces which are specified by the human operator, constraining the behavior of the model. If the energy function is well chosen, the curve will come to rest when a meaningful segmentation has been achieved.

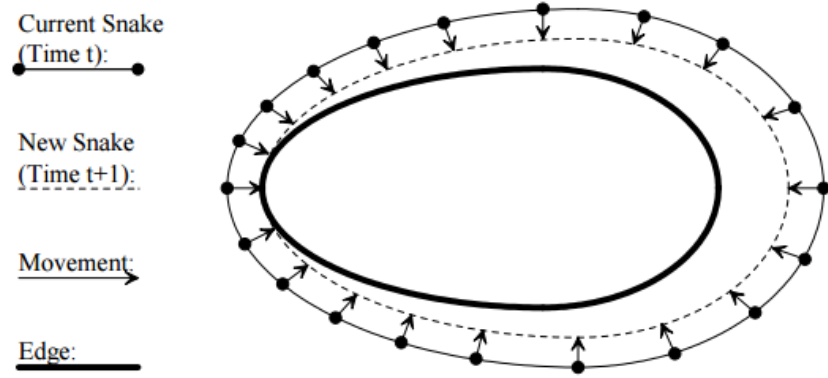


Figure 1.9 A Closed Active Contour Model (image taken from [9])

A simple snake is defined by a set of n points $x_i(s, t), i = 0..n - 1$ along the curve which depend on two parameters s (space) and t (time). The contour is influenced by the internal elastic energy term, the external edge-based energy term and by image forces. The purpose of the internal energy term is to give the model tension and stiffness. The purpose of the external energy term is to control the fitting of the contour. It usually comes from high-level sources such as users or automatic initialization process. The image force is used to drive the model towards notable features such as light and dark regions, edges, and terminations. We represent a snake as $x(s) = (x(s), y(s))$ where s usually has the value between 0 and 1. The energy function of the model E_{snake} is given by the sum of the energy for the single snake:

$$E_{snake} = \int_0^1 E_{intern}(x)ds + \int_0^1 E_{extern}(x)ds + \int_0^1 E_{image}(x)ds \quad (2.34)$$

The *internal energy* is defined as the sum of the continuity of the contour and the smoothness of the contour

$$E_{intern}(x) = \alpha(s)|x_s(s)|^2 + \beta(s)|x_{ss}(s)|^2 \quad (2.35)$$

The first-order term regulated by $\alpha(s)$ makes the snake contract like an elastic band under tension. The second-order term controlled by β makes it go against bending by introducing stiffness.

The *external energy* is usually the constraint forces introduced by the user to drive the snakes to or from particular features interactively.

The last energy, *image energy*, is a function of the characteristics of the image. There are three different image energy functionals that attract snakes to lines, edges, and terminations. The total potential energy can be represented as a weighted combination of these functionals:

$$E_{image} = w_{line}E_{line} + w_{edge}E_{edge} + w_{term}E_{term} \quad (2.36)$$

The line functional is the intensity of the image, which can be expressed as

$$E_{line} = I(x, y) \quad (2.37)$$

The edge functional is a gradient-based potential energy such as

$$E_{edge} = -|\nabla I(x, y)|^2 \quad (2.38)$$

An energy term based on curvature of level lines can find the ends of line segments and corners in a slightly smoothed image $C(x, y) = G_\sigma * I(x, y)$

where G_σ is a Gaussian with standard deviation, σ . The gradient angle is given

$$\text{by } \theta = \arctan\left(\frac{c_x}{c_y}\right) \quad (2.39)$$

Unit vectors along the gradient direction are

$$n = (\cos\theta, \sin\theta) \quad (2.40)$$

and unit vectors perpendicular to the gradient direction is

$$n_\perp = (-\sin\theta, \cos\theta) \quad (2.41)$$

The termination functional of energy can be represented as

$$E_{term} = \frac{\partial\theta}{\partial n_\perp} = \frac{\partial^2 C / \partial^2 n_\perp}{\partial C / \partial n} = \frac{c_{yy}c_x^2 - 2c_{xy}c_xc_{xy} + c_{xx}c_y^2}{(1 + c_x^2 + c_y^2)^{3/2}} \quad (2.42)$$

2.7.2 Localized active contour model

Lankton [18] developed a framework, where segmentation is based on information from the local interior and exterior regions along the contour rather than global regions. This replaces the assumption that the foreground and background regions are distinguishable based on their global statistics with the assumption that smaller regions will be different locally. The analysis of local statistics leads to the development of a family of local regions at each point of the curve. The motion of each point achieves optimization of the local energy to optimize the energy added from its local region. Each point's component of the overall energy is computed by splitting the local neighborhoods into the local interior and local-exterior using the evolving curve and a characteristic function.

Considering an image I defined on Ω , let C be a closed contour represented as the zero level set of a signed distance function ϕ such that $C = \{x | \phi(x) = 0\}$, the interior of C is specified by the following approximation of the smoothed Heaviside function:

$$H\phi(x) = \begin{cases} 1, & \phi(x) < -\epsilon \\ 0, & \phi(x) > \epsilon \\ \frac{1}{2} \left\{ 1 + \frac{\phi}{\epsilon} + \frac{1}{\pi} \sin\left(\frac{\pi\phi(x)}{\epsilon}\right) \right\}, & \text{otherwise} \end{cases} \quad (2.43)$$

Similarly, the exterior of C is defined as $(1 - H\phi(x))$.

Using these notations, Lankton defined the energy function for a generic force function, F , as such:

$$E(\phi) = \int_{\Omega_x} \delta\phi(x) \int_{\Omega_y} B(x, y) \cdot F(I(y), \phi(y)) dy dx \quad (2.44)$$

where $B(x, y)$ is a characteristic function defined by:

$$B(x, y) = \begin{cases} 1, & \|x - y\| < r \\ 0, & \text{otherwise} \end{cases} \quad (2.44)$$

with r as a predefined radius value. In this model, the energy is computed based on how we choose the region-based function, F . An appropriate choice of F can be the means-separation energy model by Yezzi et al. [19] assuming that foreground and background regions should have maximally separate mean intensities, or uniform modeling energy by Chan–Vese [16] assuming that the foreground and background are constant intensities represented by their means. This Ph.D. dissertation used an adapted version of Lankton model implemented in MATLAB to segment liver CT scans.

2.8 Literature review

Minimally invasive liver surgery is a complicated procedure potentially aided by image guidance. The technique requires fusing a pre-operative imaging set with live intra-operative laparoscopic images, rendering the target organ to appear transparent. Augmented reality (AR) is the method of superimposing segmented structures on a live video feed [37] or the tissue's surface [38] intra-operatively. AR acquired from pre-operative images can guide resection in laparoscopic surgery, highlighting the liver and its internal structures through virtual transparency. This construct works well until the actual resection begins and deformation of the liver degrades the accuracy of the image fusion.

Pessaux et al. [39] proposed a registration technique to combine with the augmented visualization. The delineated anatomical model was superimposed to the operative field and was manually registered by a computer scientist using a video mixer in real time. Even so, the elasticity of the liver was not taken into account in this approach. This made the registration in large deformation difficult.

Nicolau et al. [40] described two main strategies to account for tissue deformation: one is the non-rigid registration of pre-operative images to tissue surfaces reconstructed from laparoscopy information. The second is intra-operative imaging. For intra-operative imaging, laparoscopic ultrasound is mostly focused by most of the research due to the absence of radiation exposure and its low cost. It anticipates being used in navigated surgery [41]. However, ultrasound has many disadvantages such as dependence on the user's expertise,

poor-image quality, and the restriction of the field of view. Moreover, image acquisition has to be repeated during the procedure in this approach.

Shekhar et al. [42] addressed all these problems using a conventional CT scanner in laparoscopic liver surgery on animals. Low-dose CT scans allowed continuing registration of the pre-operative diagnostic CT scan to the live information on organ deformation. Unfortunately, a built-in CT scanner is often not existent in an operating room as it would require larger rooms and would limit the maneuver ability of the surgeons.

To increase the mobility at the operation table, Hannes et al. [20] used a commercially available AR guidance system employing intra-operative robotic C-arm cone-beam computed tomography for laparoscopic liver surgery. The main advantage of the method is the integrated environment which is provided by hybrid operating room. Nevertheless, the need to leave the room during performing a cone-beam computed tomography and the repeated radiation expose limit this technique.

Another strategy would be to register the pre-procedural image data to intra-operative data such as organ surfaces. One of the possible solutions is marker-based registration which requires a tracking system in the operating room. Available options for a tracking system are magnetic or optic tracking. Both have certain drawbacks. While magnetic systems are very susceptible to contortion and error due to magnetization, optical systems require a direct line of sight [43].

Haouchine et al. [22, 23] built the framework for augmented reality during hepatic surgery. In their approach, a biomechanical model of the liver was combined with an optical tracking method to provide constraints for the model. The biomechanical model could compute the deformation of the organ under the stretching forces induced by a tracked 3D-control point set. In the experiment, they used a stereoscopic camera to capture the liver surface which was an expensive equipment and had the need for unobstructed vision.

Wu et al. [21] used both surface data and subsurface data within the context of a non-rigid registration methodology to align deformed intra-operative surface data to the corresponding pre-operative liver model. They validated their work by using a liver phantom which had implanted CT-opaque target beads and was supported by small blocks to simulate the organ deformation that occurs when the surgeon uses padding to stabilize the tissue. After registration, they calculated the mean target error by comparing the intra-operative bead locations obtained in a CT scan to their registered pre-operative counterparts. For validation, they used a conoscope to take the surface data and used CT scan to simulate the subsurface data from an ultrasound scanning.

Intra-operative ultrasound and MRI are other alternatives to registering pre-operative data. Intra-operative ultrasound is more widely adopted [41]. Still, it can cause missing data due to deep location of metastases, the existence of air between target and risk structures, and the inexperience of the user. On another hand, intra-operative MRI requires non-ferromagnetic instruments as well as protective lead clothing.

2.9 Dissertation proposal

Our approach was also to build a mechanical model of the liver, based on the pre-operative images and simulate the deformation; however, we introduced several new ways to obtain additional boundary constraints for the model which is more practical and cost-effective in real surgery. Therefore, we were not limited by the drawback of one individual method of acquiring intra-operative data as our methods could support and compensate each other.

We set up an experiment using an explanted porcine liver to verify our model in a particular scenario which involves elevating the liver using surgical instruments to access and view the posterior aspect of the liver. We deployed a guide wire into the biliary duct as another mean of reference to register the model. We combined two successive views through the laparoscopes at different angles with the 3D-localization of a fixed tool at one single location to retrieve liver surface information. By using three overlapping localization techniques: the boundary conditions provided by the instrument, the surface information from the laparoscopes, and sub-surface information from the guide wire, we aimed to retrieve the liver location and the target tumor when a lobe of the liver is elevated during surgery.

Additionally, we integrated those methods into a framework which acts as the backbone of the guidance system. In this framework, we can add or replace the techniques of acquiring or processing data as long as they have the same functionalities.

Part II

Developing of the image-based guidance system

Chapter 3

Building the framework

3.1 Main workflow of the framework

Before surgery, pre-operative imaging data are usually taken to allow visualization and localization of the tumor and internal structure. X-Ray Computed Tomography (CT) and Magnetic Resonance Imaging (MRI) are two kinds of image modality that commonly employed due to their high spatial resolution and contrast. The images are invaluable in the surgical planning phase but are not often used during surgery due to organ shift and non-rigid deformations.

On the other hand, intra-operative imaging provides information on the fly. However, it is usually more costly and possibly inconvenient due to its

interference with other surgical instruments. Model-based registration methods can help to alleviate the problem by only using sparsely acquired intra-operative data to transform the pre-operative images into the current state during the surgery. A proper registration can assist the surgeon in tracking tumor location, define the resection plane and improve surgical outcomes.

Both pre-operative data and intra-operative data are needed as input for the mechanical model. The model then simulates the tissue motions and outputs information which can assist surgeons in decision making. We have built the framework based on this workflow so that it can accommodate the advances of the techniques. The framework contains four main components: Pre-operative, Intra-operative, Tissue mechanics, and Post-processing (Figure II.1).

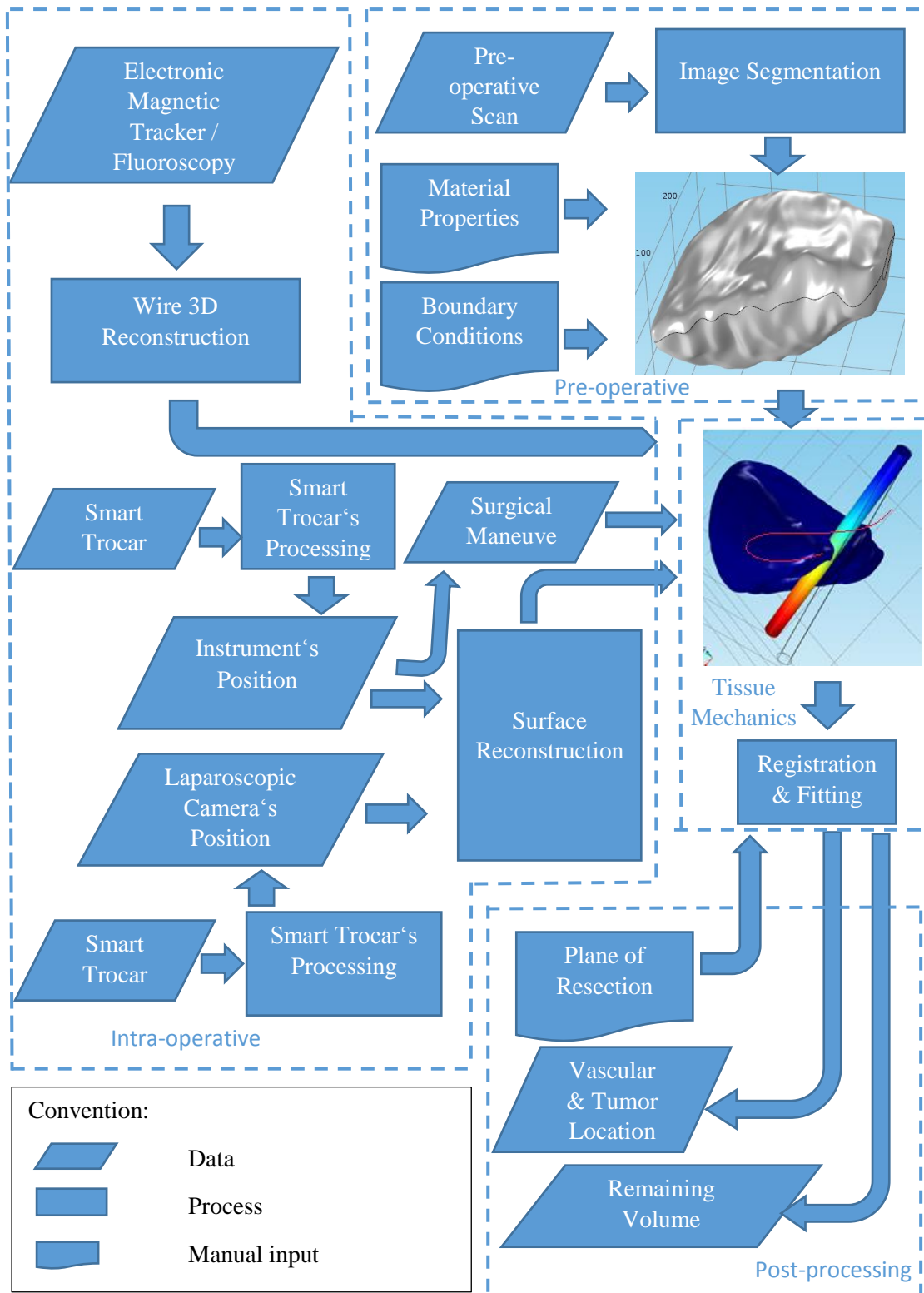


Figure II.1 Workflow of the framework.

3.2 Description of the components

3.2.1 *Pre-operative component*

The purpose of this component is to build the 3D-reconstruction and setup initial constraints for the tissue based on the pre-operative scans and prior knowledge about the tissue. To be extracted the liver and its vascular system, the images was put through the image segmentation process. From those segmentations, a 3D-geometry of the organ is built. Information about material properties of the liver (Young's modulus, Poisson's ratio, density) and constraints (attachments holding the liver) based on prior knowledge are also inputted to the model.

a. Liver segmentation

First, the liver boundary is extracted from the dataset automatically. Due to noises of the actual images, the automatic method does not yield perfect results. They need to be verified by experienced users to correct the segmentation using the manual method with a graphical user interface to refine the segmentation.

i. Automatic method:

This method has three steps:

(1) Determine the beginning slide and end slide of the liver in the data set

(2) Divide the slides into a smaller group (usually each 20 slides). In each group:

(i) Select one middle slide and make boundary of the liver as starting contour

(ii) Run the snake method using the starting outline as an initial contour

(3) Link the result of all the groups to obtain whole liver segmentation.

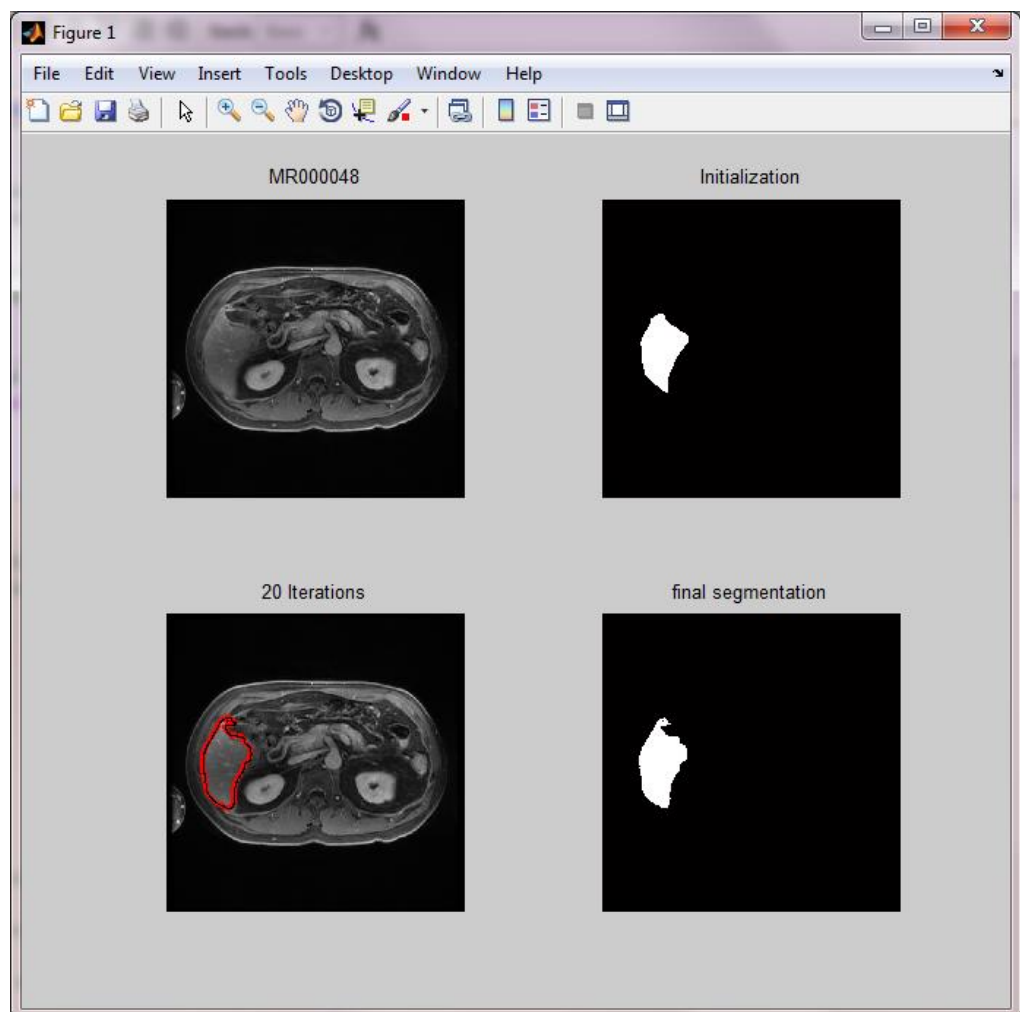


Figure II.2 Run the snake method to segment the liver from the scans

ii. Manual method:

A program with graphical user interface was developed to check and fix the result of the automatic method.



Figure II.3 Guide user interface for manual method

Each of the slides from the result of the automatic method is displayed on the right side along with the corresponding patient data slide on left side. If the result is not good enough, the user can select points on the liver's contour and have the program interpolated them into a new segmentation result. If the new result is satisfying, it will be saved into the database.

b. Biliary duct segmentation

With the extracted liver used as a mask for the region of interest, the biliary duct is obtained by using the following steps.

(1) Use the liver segmentation method to get the liver mask

(2) Apply anisotropic filter to reduce noise

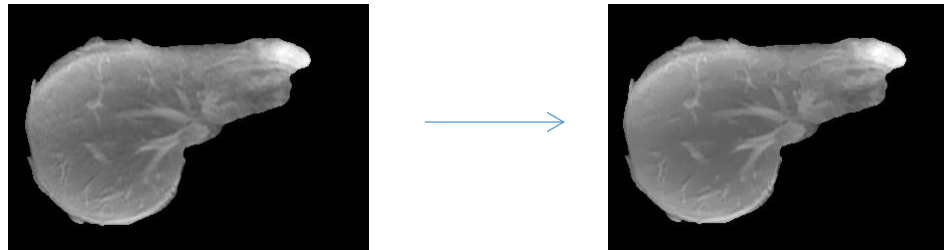


Figure II.4 Apply anisotropic filter to the image to reduce noise

(3) Apply white top-hat transform to obtain a new image containing the objects or elements that are smaller than the structuring element and are brighter than their surroundings.

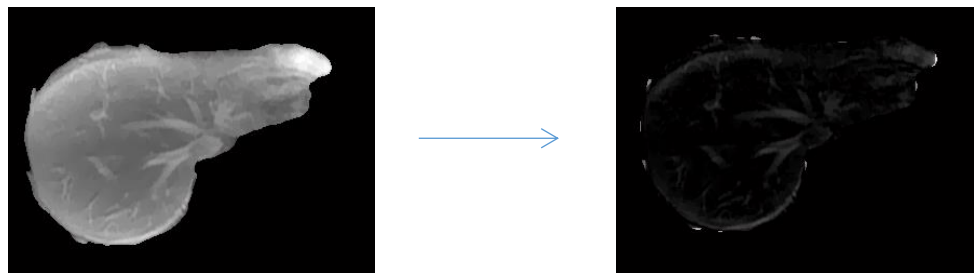


Figure II.5 Apply white top-hat transform to the image

(4) Use adaptive threshold with Otsu's method in 20 by 20 pixel window

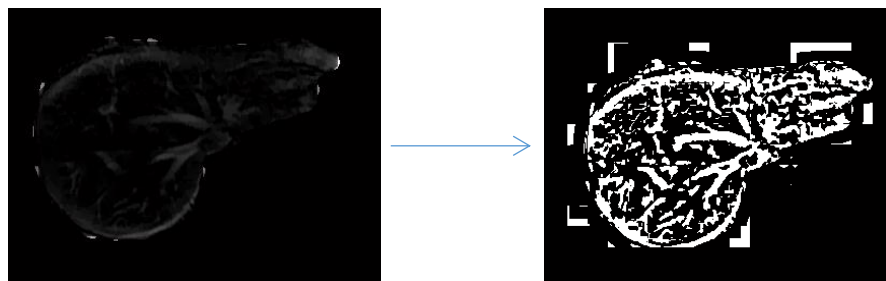


Figure II.6 Apply adaptive threshold with Otsu's method.

(5) Do erosion transform on the liver's mark to have a new mask and apply that mask for the segmentation

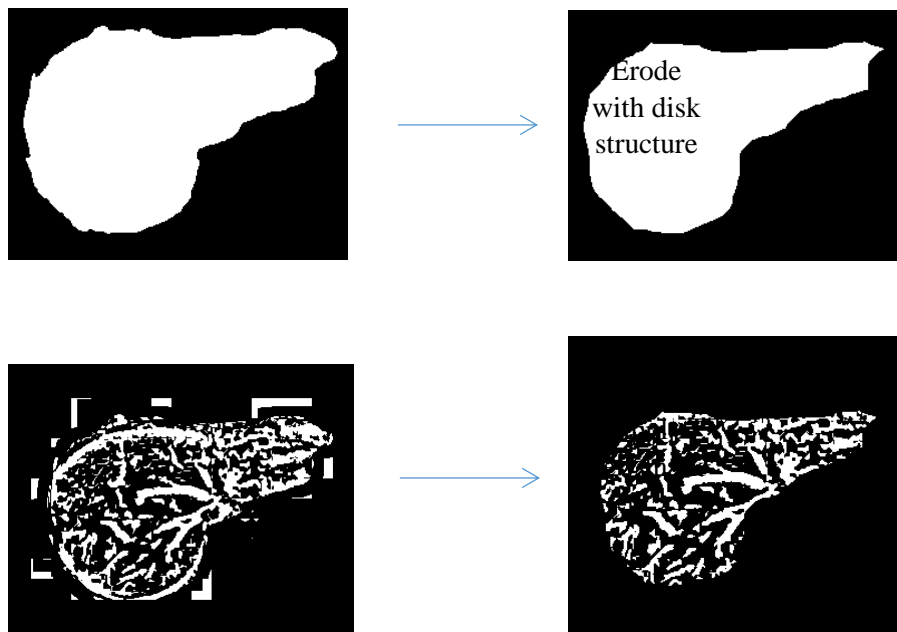


Figure II.7 Apply new mask which comes from erosion transform of the old mask

(6) Do open operation with ball structure and remove small objects

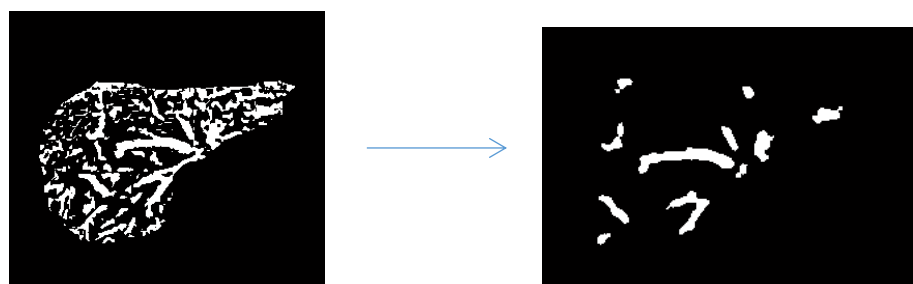


Figure II.8 Do open operation with ball structure to remove small objects.

After final step, the binary image is acquired with only the biliary duct segmentation.

c. Artery and vein segmentation

i. Artery segmentation:

The same technique was used for artery segmentation. First, apply the automatic method then refine it with the manual method.

ii. Vein segmentation:

The venous structures can be divided into two parts

- Inside the liver: apply the same method used for biliary duct segmentation
- Outside the liver: apply the same method used for liver segmentation

3.2.2 *Intra-operative component*

This component provides the constraints/reference for the deformable model during the surgery. It currently has three types of information:

- Location of the guide wire/stent: Dr. Brian Dunkin suggests that a simple pre-operative ERCP can be used to place markers or "fiducials" in the CBD which provides the surgeon a real-time map of the liver relative to an anatomically relevant set of coordinates, namely known locations in the biliary and hepatic ductal structures. The wire can be tracked during real-time surgery using the electromagnetic tracker or fluoroscopy.
- Surgical maneuver: the source of liver motion is mostly from its contact with the surgical instruments. If we can understand the location of the tool and how it manipulates the liver, we can simulate the same maneuver with our model. The location of the instrument can come from the Smart Trocar, a new surgical instrument recognition system, which is introduced in Chapter 5.
- Surface imaging: the surface information of the liver is one of the key intra-operative data for a registration system. In other image-guided systems, this information is usually obtained by using specific piece of high-tech equipment such as a stereoscopic camera. In this work, we present a new method to reconstruct the 3D-surface of the liver with only 2D cameras and the Smart Trocars. For detail, refer to Chapter 5.

3.2.3 *Tissue mechanics*

This component receives the input from pre-operative and intra-operative components, setups the physics of the model and runs the solver. The registration process here aligns pre-operative image information to the intra-operative setting by estimating the deformation parameters and calculating the fitting error. If the error is converged, the registration is completed. If not, it adjusts the parameters and repeats the loop until convergence.

In the scope of this dissertation, only linear-elastic and hyper-elastic model are used to build the finite-element model of the liver. But one can adapt any model or registration technique to the framework.

3.2.4 *Post-processing component*

This component used the result of the tissue mechanics component to predict the new location of the tumor and vascular system after the deformation. Moreover, if the plane of resection is defined on the pre-operative images, the component will show the new resection plane and the remaining volume of the liver after the cut. Our framework does not include a module to display augmented reality because it will take a lot of processing power and additional complexity to the system. Therefore, our goal of the system concentrates in solving practical problems of the surgical navigation: identifying the location of the tumor and plane of resection during surgery. Chapter 4 will present a showcase of the framework and our philosophy.

Chapter 4

Validation of the mechanics modeling framework

This chapter presents a method to localize the position of a liver and a tumor within the tissue during a minimally invasive liver operation. Section 4.1 introduces the problems and our method to solve the problems. Section 4.2 describes the experimental setup of the porcine explant model. Section 4.3 gives details about building the mechanical model and fitting it to intra-operative data. Section 4.4 is about validating our model and conducting sensitivity analysis. We also discuss the limitations of the model and how to improve it in the future. The content of this chapter comes from our publication [63].

4.1 Problem statement and method

We aim to solve the following practical surgical navigation issues:

- (1) Problem 1: The surgeon uses the laparoscopic tool to elevate a part of the posterior of the liver for access/visualization. In doing so, the tumor inside the liver also changes location compared to the pre-operative images. We now need to identify where is the new location of the tumor.

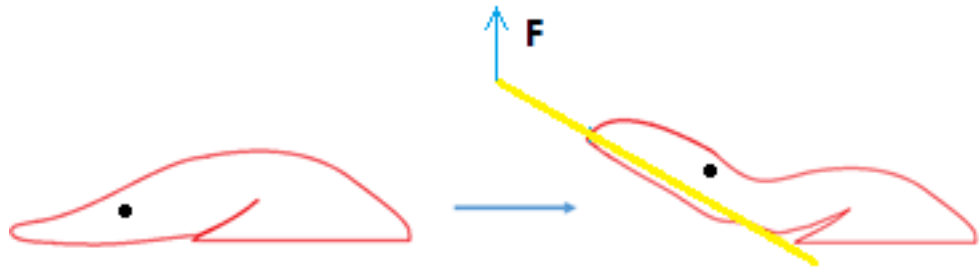


Figure II.9 Tumor (black) location changes after lifting with a surgical tool.

- (2) Problem 2: The surgeon has planned a resection plane to remove the tumor before the surgery. With the liver lobe elevated we need to identify where the new resection plane is, and what is the new volume of liver remaining after resection.

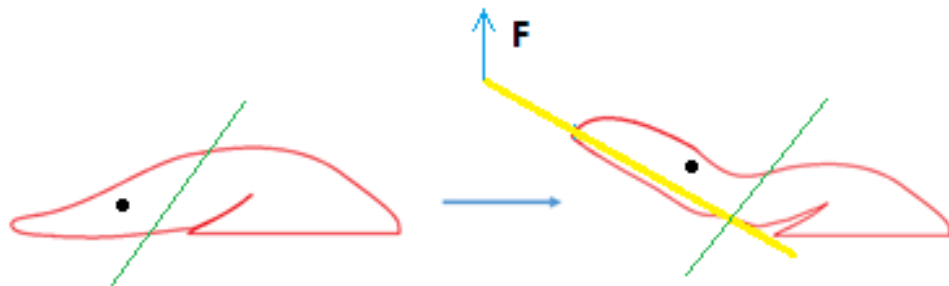


Figure II.10 Resection plane (green) changes after lifting with a surgical tool.

To solve these problems, we built a mechanical model of the liver based on the pre-operative images with the hypothesis that we can obtain the position of the lifting instrument and other constraints on the liver with other techniques. An additional reference that can be applied to the model is a guide wire placed into the biliary duct. Its location can be obtained quickly using almost all standard imaging methods. Radiocontrast agents also provide visualization of the vasculature to provide more dynamic landmarks.

4.2 Experimental setup

A fresh porcine liver (explanted from a heparinized and sacrificed animal) having all major hepatic vasculature identified and ligated, after flushing with water, was used for the experiment. A three-way stopcock was tied in place at the inferior vena cava to allow for contrast infusion while keeping the liver an enclosed system. For the CT images, the contrast used was Omnipaque 300 mg/ml diluted 50% with normal saline. Approximately 250 cc was injected to fill the vasculature.

A hollow radiopaque ball was implanted as a simulated tumor into the liver parenchyma under ultrasound guidance to ensure that it was adjacent to a major blood vessel in the liver lobe. After placement, the ball was sutured in place. A stiff guidewire was deployed into the biliary duct (via the common bile duct) until it reached the tip of the left lobe to provide an additional reference for the model.

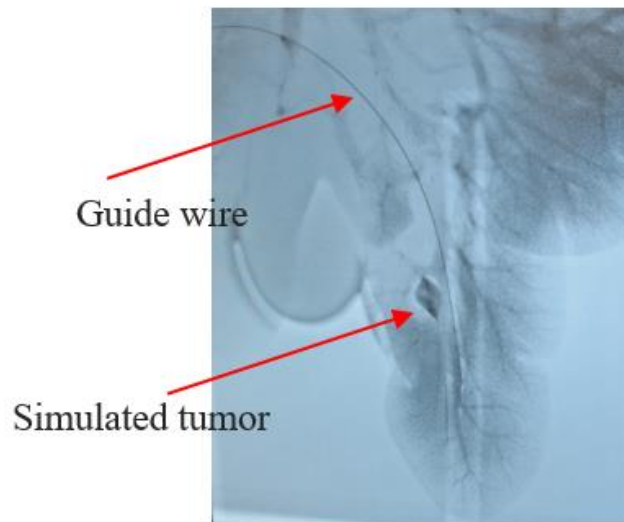


Figure II.11 X-ray image of the liver showing guide wire, simulated tumor, and vessels

The liver was set up in 2 different positions:

- (1) The liver in flat-down position – position A

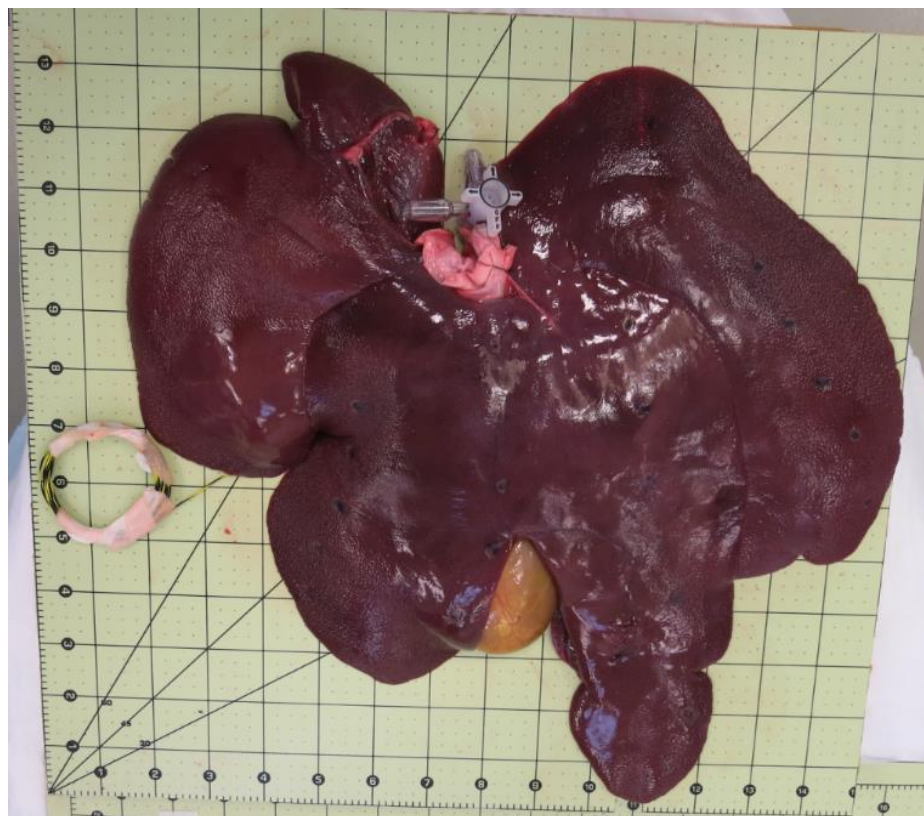
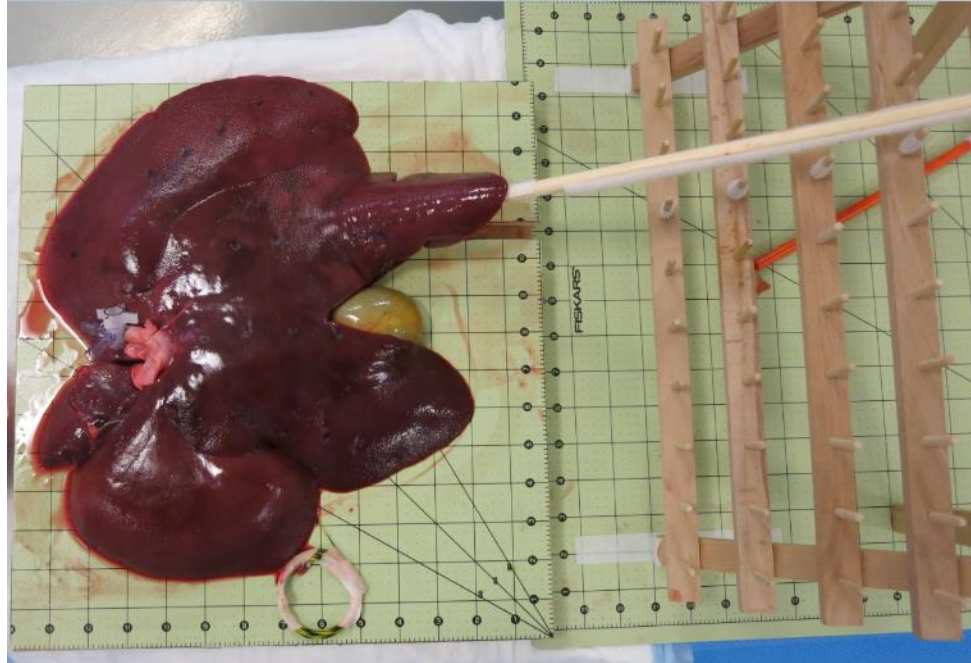


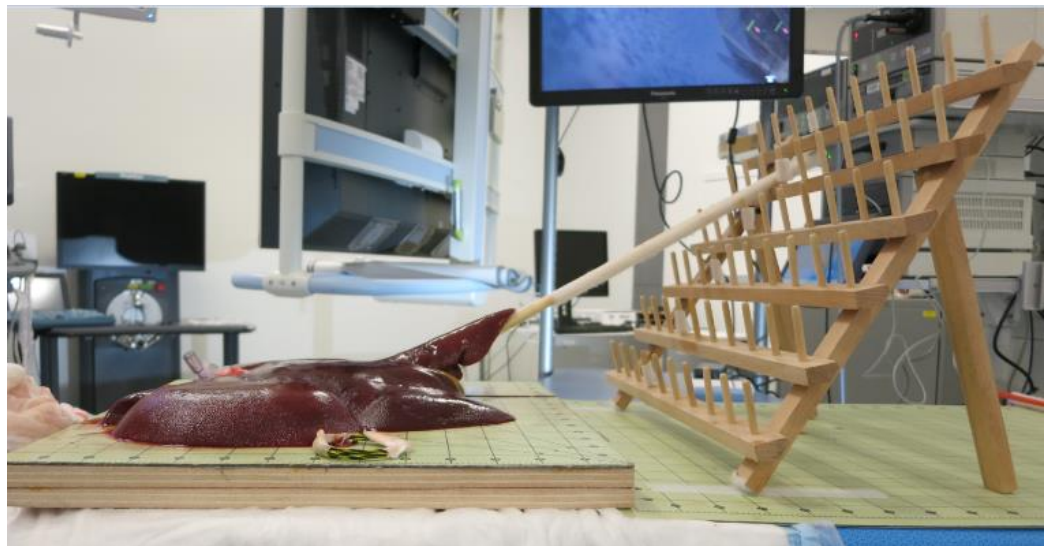
Figure II.12 Porcine liver in position A - stays flat down

The liver laid flat on the checkerboard, which was divided into 1-inch squares for measuring purposes.

(2) Liver in elevated position – position B



(a)



(b)

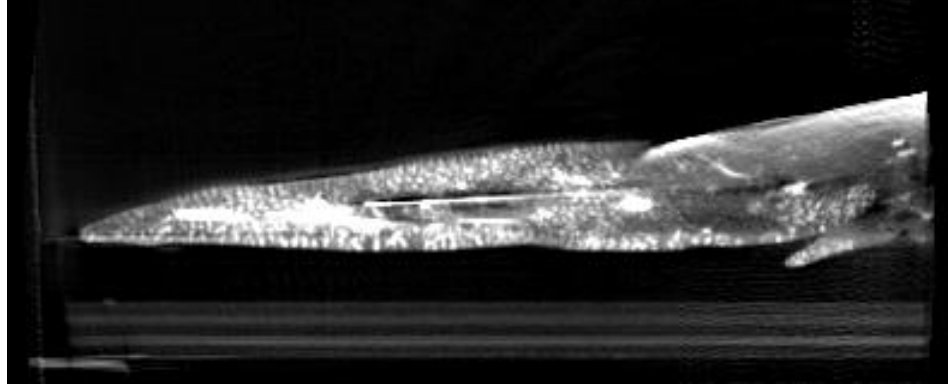
Figure II.13 Porcine liver in position B - elevated. (a) Top down view (b) Side view

The board had a slot cut into it matching the dimensions of the wooden lever so that it could be inserted under the left lobe of the liver without moving it. The lever was used to lift the left lobe of the liver up and hold the position for image acquisition. To keep the lever at a certain angle, a wooden rack was set up with fasteners to keep it in place. The angle of the lever was determined by the level of the rack it has been put on.

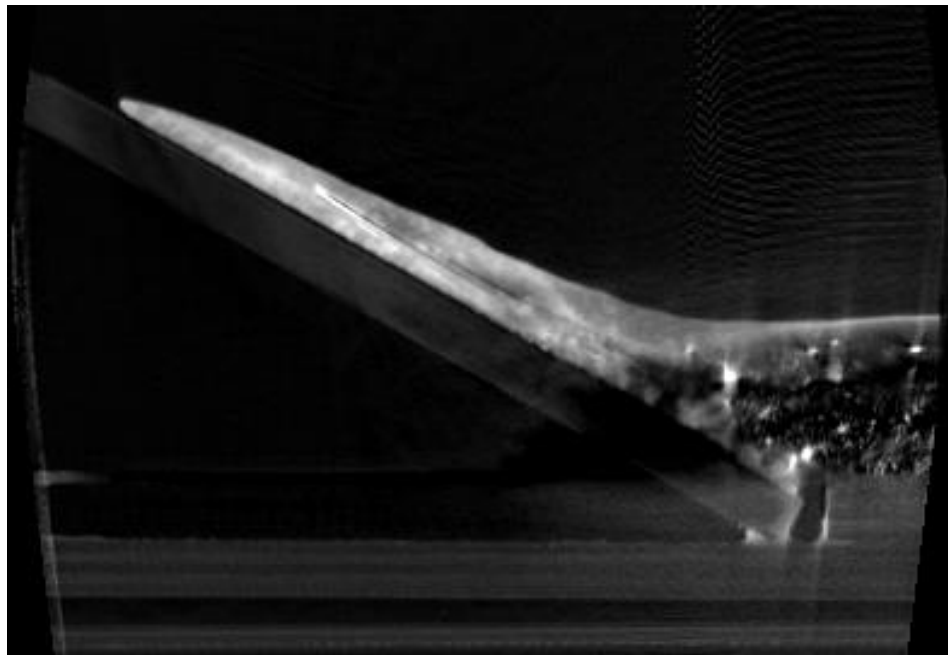
This setup was equivalent to using laparoscopic instruments to lift the liver and expose the posterior surfaces of the liver to visualize important structures. The rest of the liver remained in the same position as position A.

4.3 Model and simulation

First, we obtained a CT scan of the liver before and after the deformation using the Artis Zeego system.



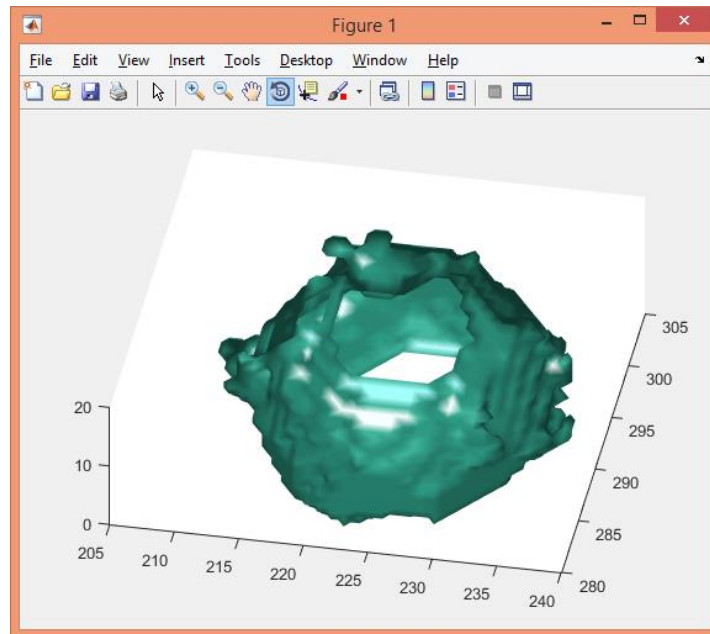
(a)



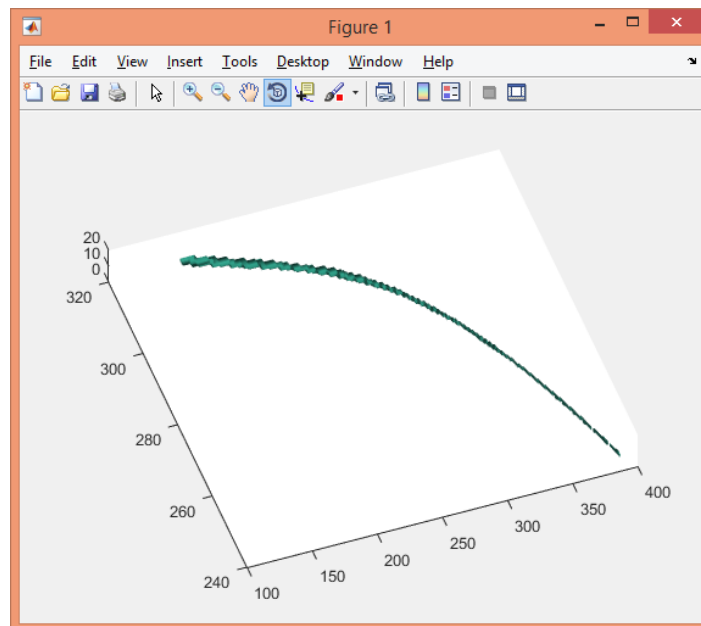
(b)

Figure II.14 Liver parenchyma and wire changes between the flat (a) and elevated (b). Position changes are visualized using the imaging modalities

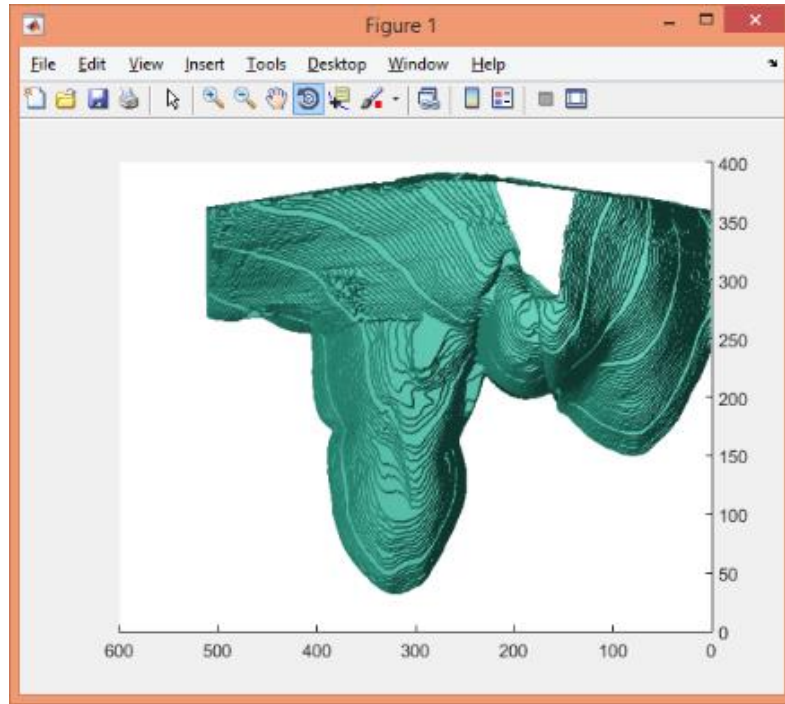
From the Dyna CT images, the liver boundary, guidewire, and tumor were extracted with a simple threshold and snake method in both positions A and B.



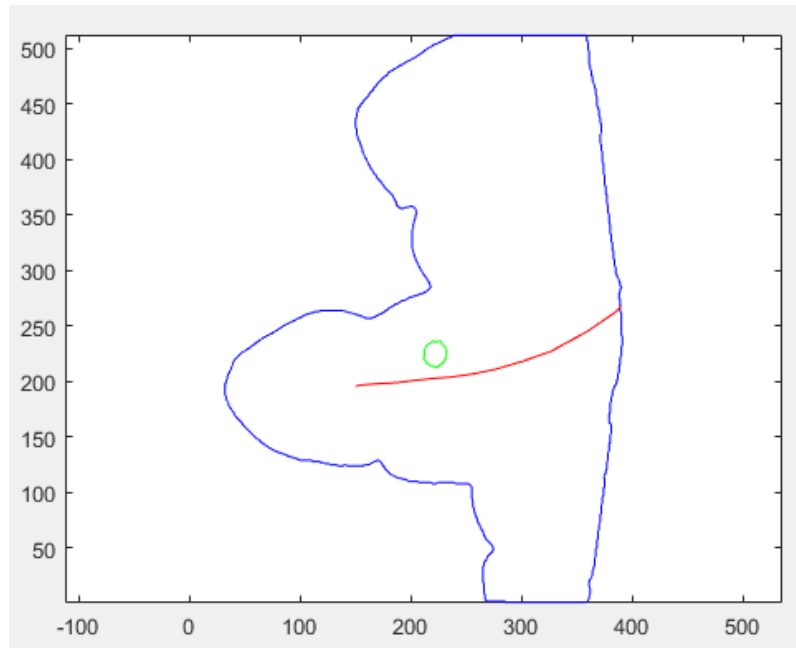
(a)



(b)



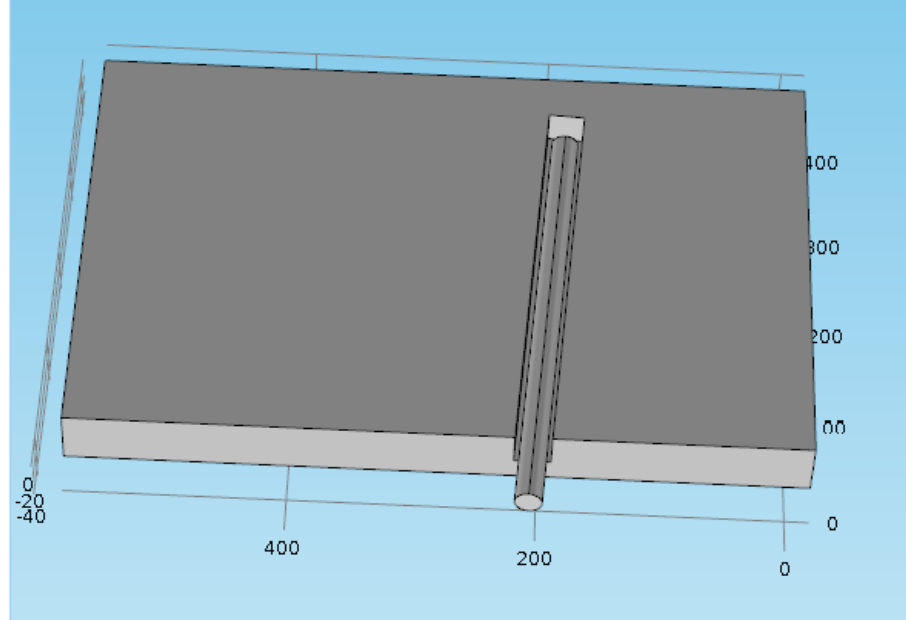
(c)



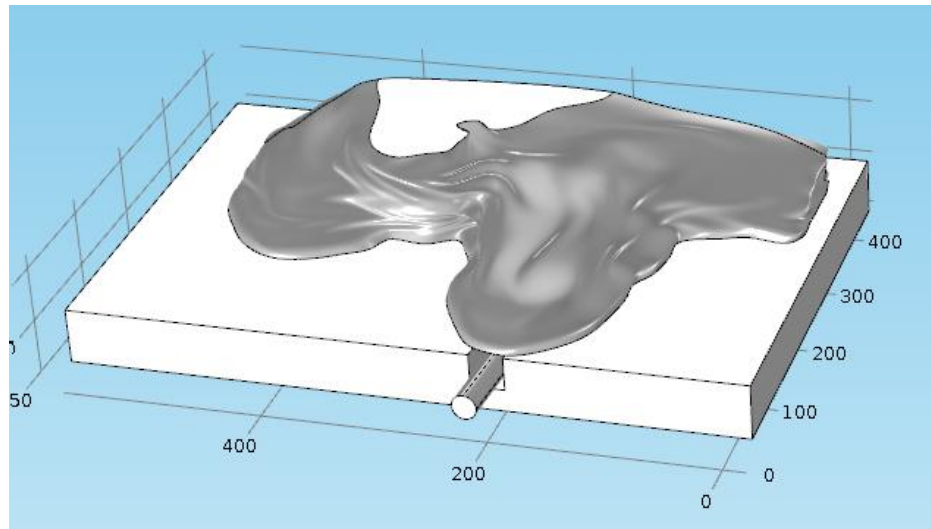
(d)

Figure II.15 Segmentation results of (a) fake simulated tumor (b) guide wire (c) liver boundary (d) 2D-top view of tumor (green), guide wire (red) inside the liver (blue).
The unit of the figure is a pixel of CT images (1 pixel = 0.5 mm)

We then built the deformable model based on segmentation of liver in position A. Using software program COMSOL, we were able to set up the same boundary conditions as the experiment.



(a)



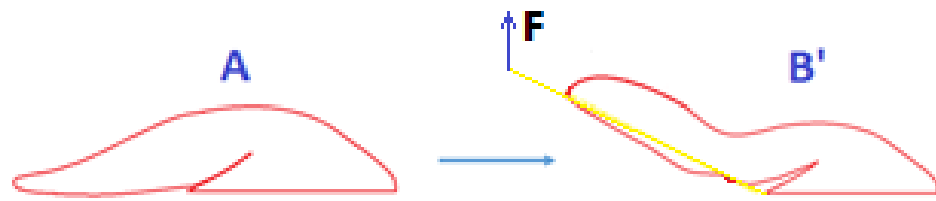
(b)

Figure II.16 Geometry of liver's simulation in COMSOL (a) without liver (b) with liver. The unit of the figure is a pixel of CT images (1 pixel = 0.5 mm)

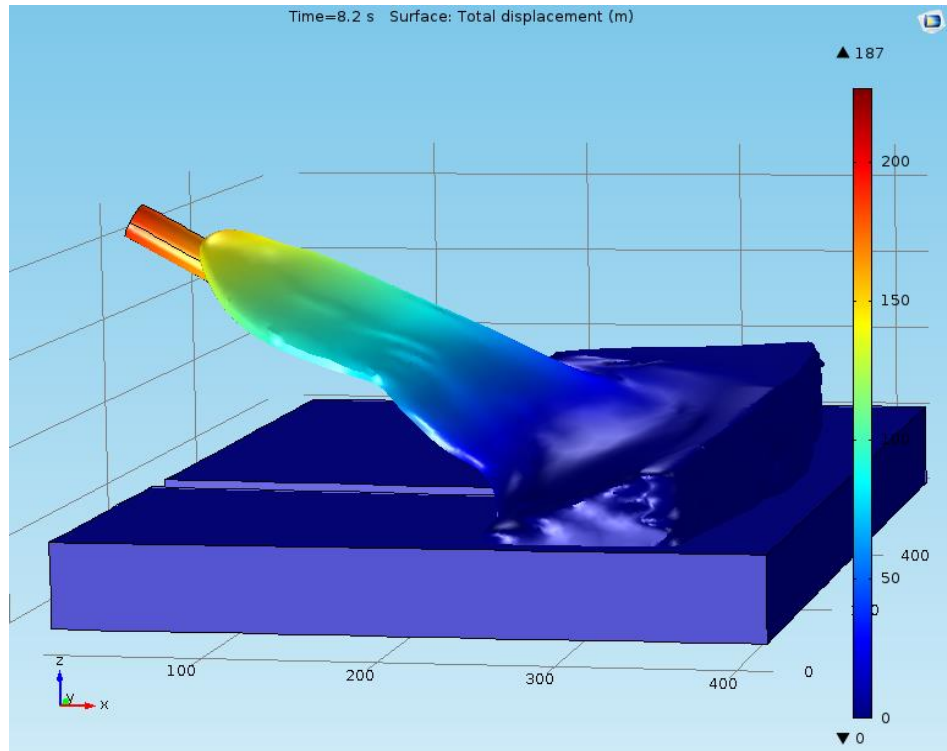
For the study, we used both linear elastic model and hyper-elastic model for the simulated liver. We chose the elastic parameters $\rho = 1150 \text{ kg/m}^3$, Young's modulus $E = 0.7 \text{ MPa}$, Poisson's ratio $\nu = 0.45$ (according to Haouchine et al. [23]). We used static Coulomb model for friction with coefficient 0.1 and cohesion sliding resistance 104 Pa. The model was solved using finite-element method with 238795 elements.

The simulation was a combination of 2 stages:

- Stage 1: The lever was lifted by applying F_{lift} on the cross-sectional area of the lever end. The other end of the lever was fixed and formed a hinge with the platform. The platform and the back side of the liver were also fixed. The lever would stop at the same angle as in the controlled environment.



(a)



(b)

Figure II.17 Stage 1 of the simulation: Liver shape changes from A to B' Color map shows the displacement of the model (a) Set up concept (b) Result of the simulation. The unit of the figure is a pixel of CT images (1 pixel = 0.5 mm).

- Stage 2: The lever was fixed, and the liver slid down a little along the length of the lever under gravity.

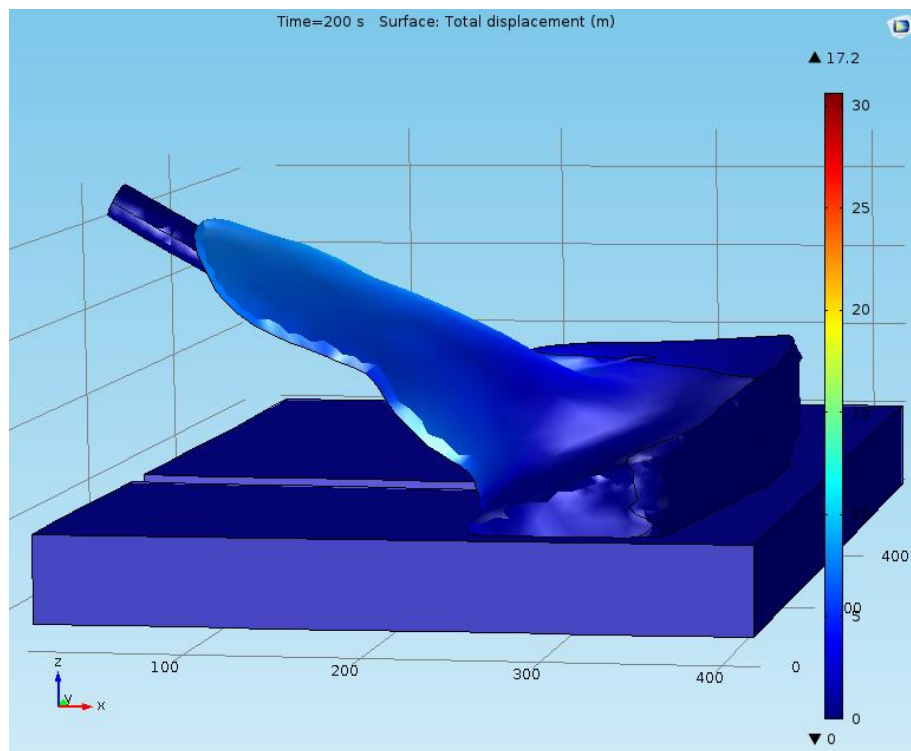
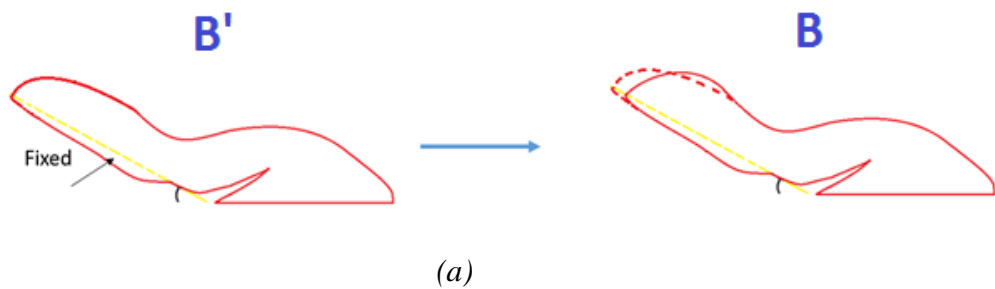
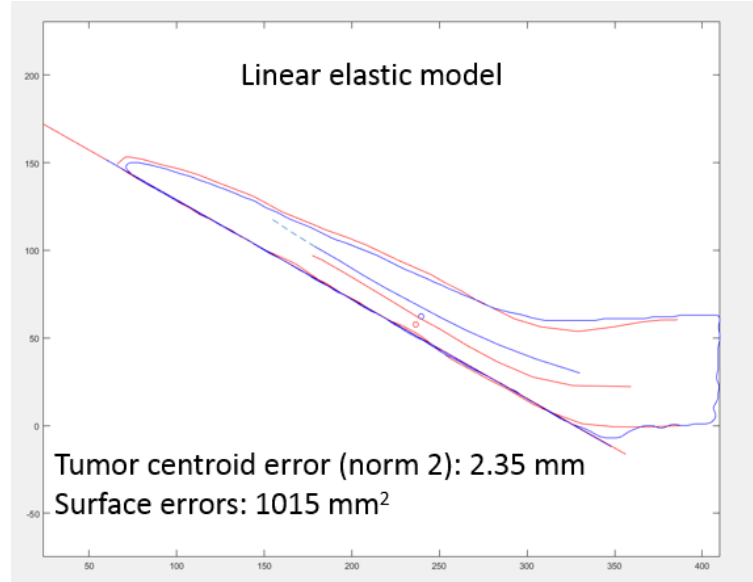


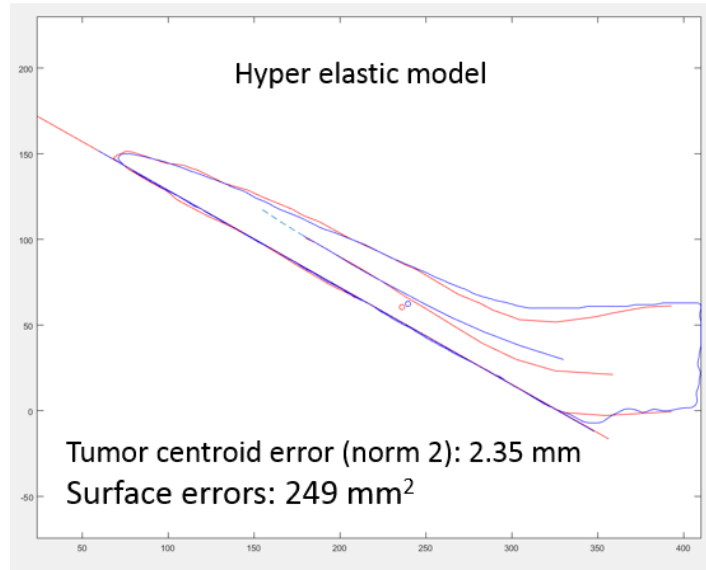
Figure II.18 Stage 2 of the simulation: Liver shape changes from B' to B. Color map shows the displacement of the model. (a) Setup concept (b) Result of the simulation. The unit of the figure is a pixel of CT images (1 pixel = 0.5 mm).

4.4 Validation and discussion

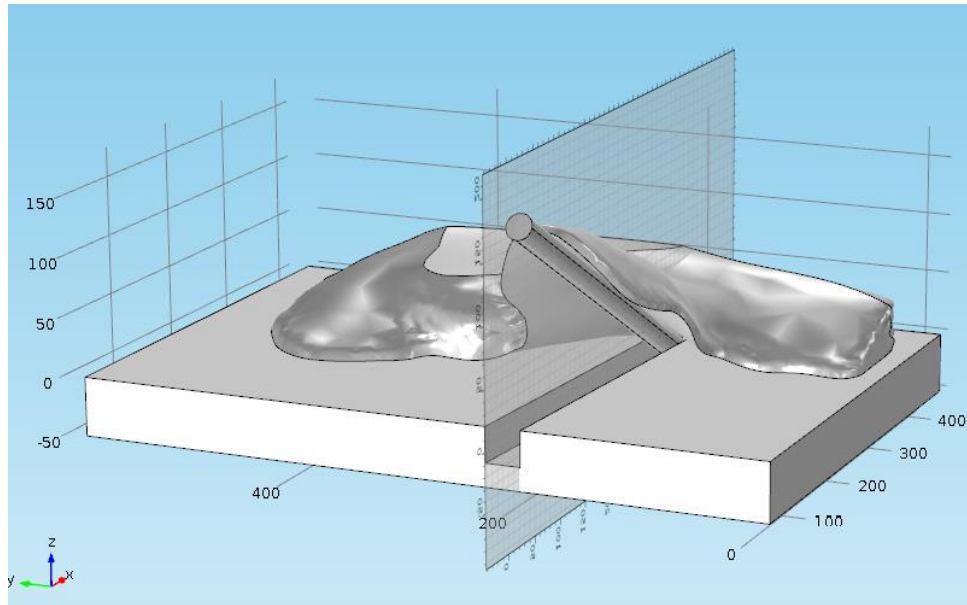
To verify the model, we took the same 2D-vertical cut at the location of the lever in position B on both the CT images and simulated model. The center of the tumor was calculated from tumor segmentation of the CT images. The liver curve was interpolated from the upper and lower surface of the simulated liver. Location of the wire and tumor were projected onto this 2D-slice for easier comparison. To check how well these two models performed on the sharp of the lobe compared to the ground truth, the surface errors of the lobe between the models and the CT images were computed by accumulating the errors of the upper curve from a series of 2D-vertical cuts along the length of the lobe from left to right.



(a)



(b)



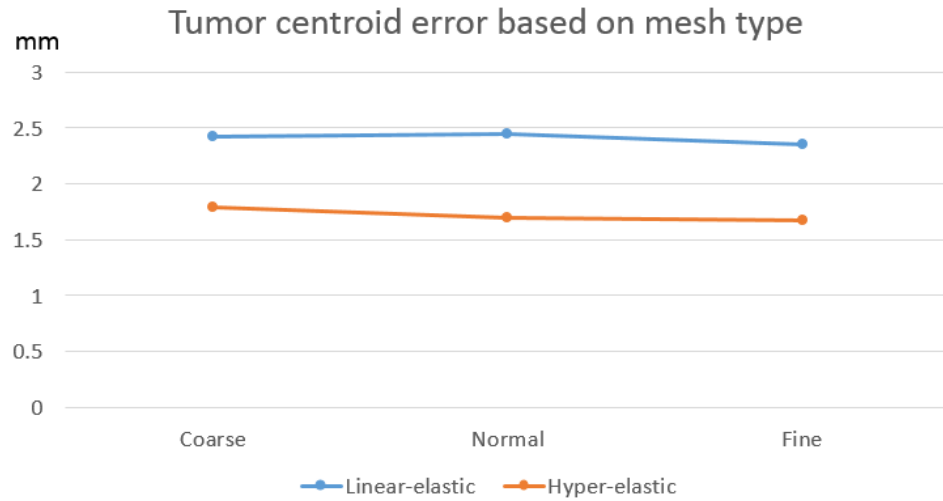
(c)

Figure II.19 Tumor centroid, guide wire, and liver upper curve comparison on same 2D-cut in position B (a) linear-elastic model and (b) hyper-elastic model (c) the position of the 2D cut
The unit of the figure is a pixel of CT images (1 pixel = 0.5 mm).

When comparing the distance from tip of the guide wire to the tip of the liver in position A to position B, the wire moved towards the tip of the liver approximately 10 mm when changing from position A to position B. Assuming that the wire moved along the duct inside the liver when the tissue was manipulated, the wire in the CT scan at position B should be cut down 10 mm from the tip to compensate for the wire movement when compared with the simulation wire. As figure II.19 showed, the simulated wire was bent in a different curve compared to the real wire, so its position did not tell much about the accuracy of the model. We assumed that the metal material property of the wire caused that much error on the simulated wire. Therefore, while the guide wire is an excellent reference for the registration, it needs to be modeled with the right material.

To go further on sensitivity analysis, we did several runs of the simulation using difference parameters on 3 type of meshing: coarse, normal and fine which has 4459 elements, 7965 elements, and 18599 elements, respectively. We then compared the error of the tumor centroid in pairs of simulations to see how the parameters affected those runs.

Figure II.20 showed the error of the tumor centroid when we used the linear elastic model and the hyper-elastic model with the same set of parameters: Young's modulus 0.7 MPa, Poisson's ratio 0.45, static Coulomb model for friction with coefficient 0.1 and cohesion sliding resistance 10^4 Pa.



*Figure II.20 Tumor-centroid error based on mesh type: Linear-elastic model vs. hyper-elastic model
The unit of the figure is one pixel of CT images (1 pixel = 0.5 mm).*

Figure II.21 showed the error of the tumor centroid when we used the hyper-elastic model with different Young's modulus values. Poisson's ratio and friction's coefficient stayed the same as previous runs.

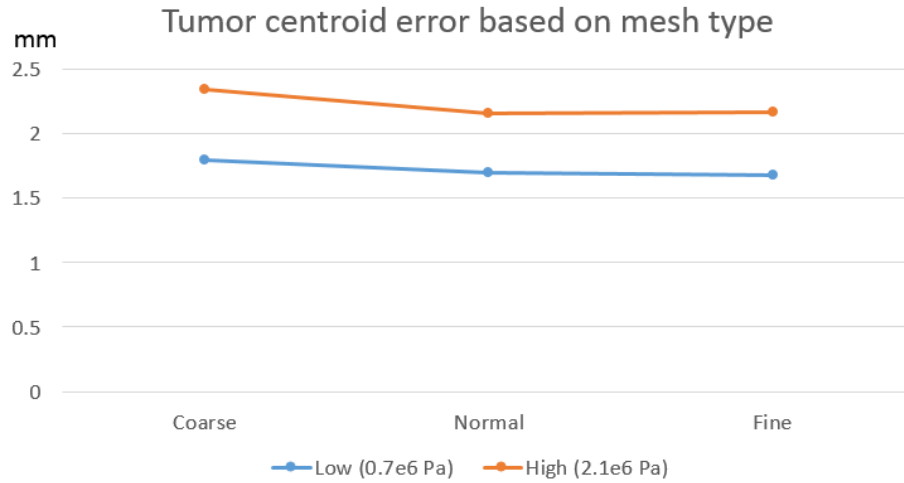


Figure II.21 Tumor-centroid error based on mesh type: Young's modulus (high vs. low)

The unit of the figure is one pixel of CT images (1 pixel = 0.5 mm).

Figure II.22 showed the error of the tumor centroid when we used the hyper-elastic model with different Poisson's ratio values. Young's modulus and friction's coefficient stayed the same as previous runs.

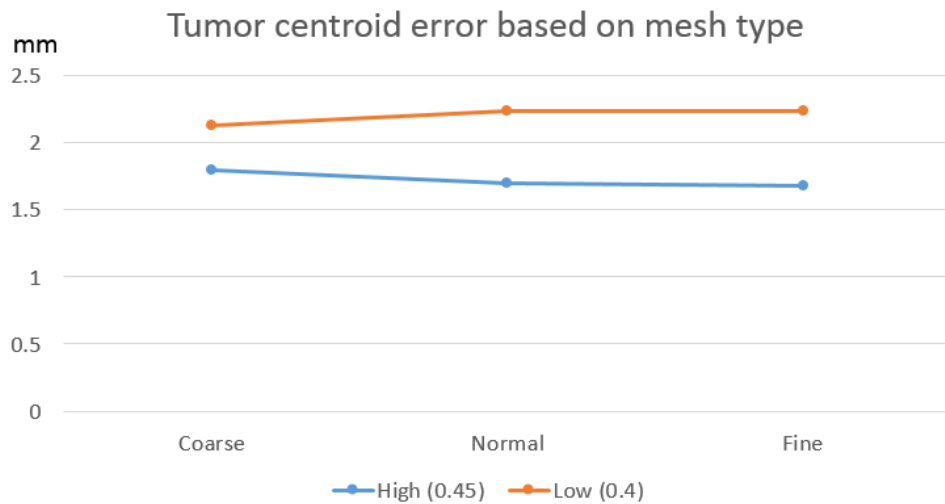
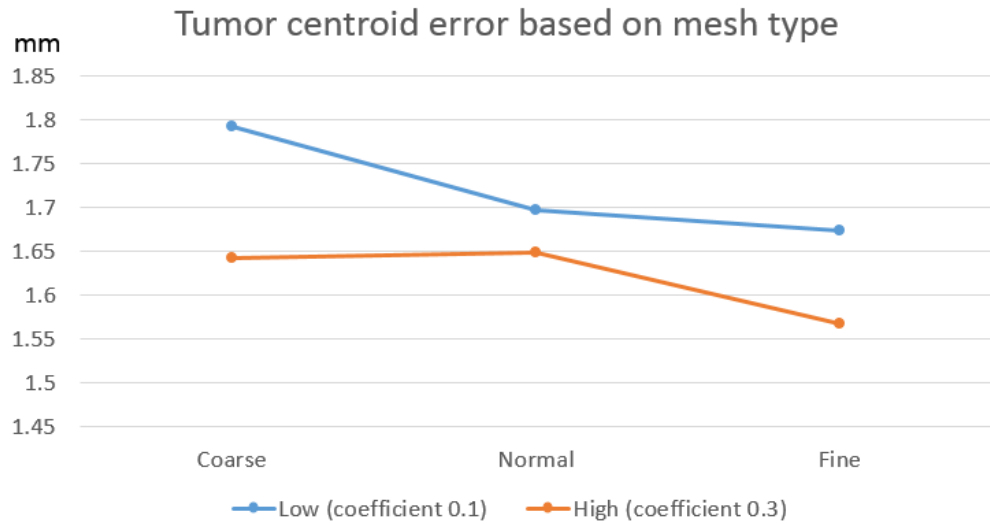


Figure II.22 Tumor-centroid error based on mesh type: Poisson's ratio (high vs. low)

The unit of the figure is one pixel of CT images (1 pixel = 0.5 mm).

Figure II.23 showed the error of the tumor centroid when we used the hyper-elastic model with different friction's coefficient values. Young's modulus and Poisson's ratio stayed the same as previous runs.

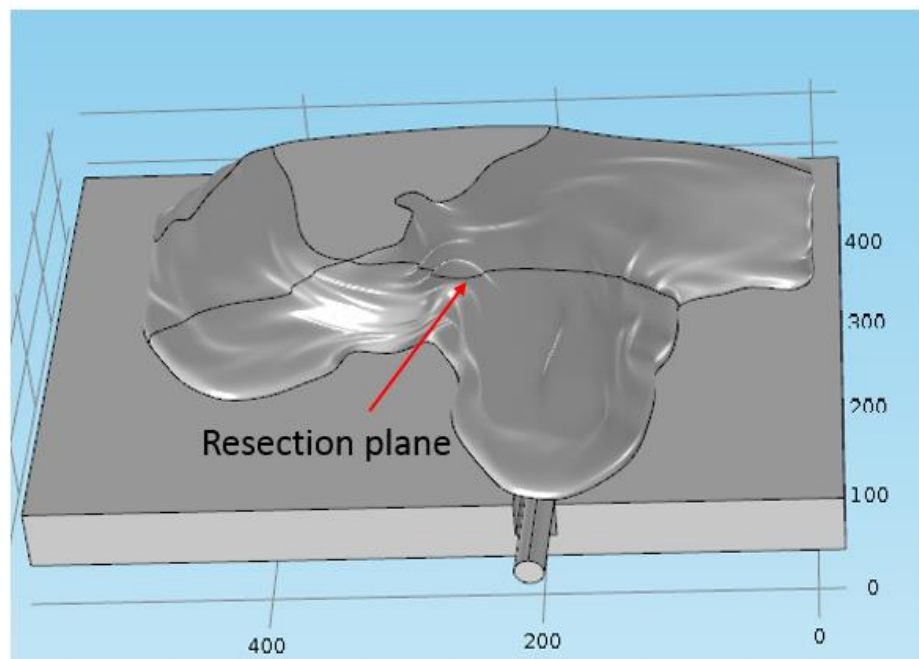


*Figure II.23 Tumor-centroid error based on mesh type: Friction (high vs. low)
The unit of the figure is one pixel of CT images (1 pixel = 0.5 mm).*

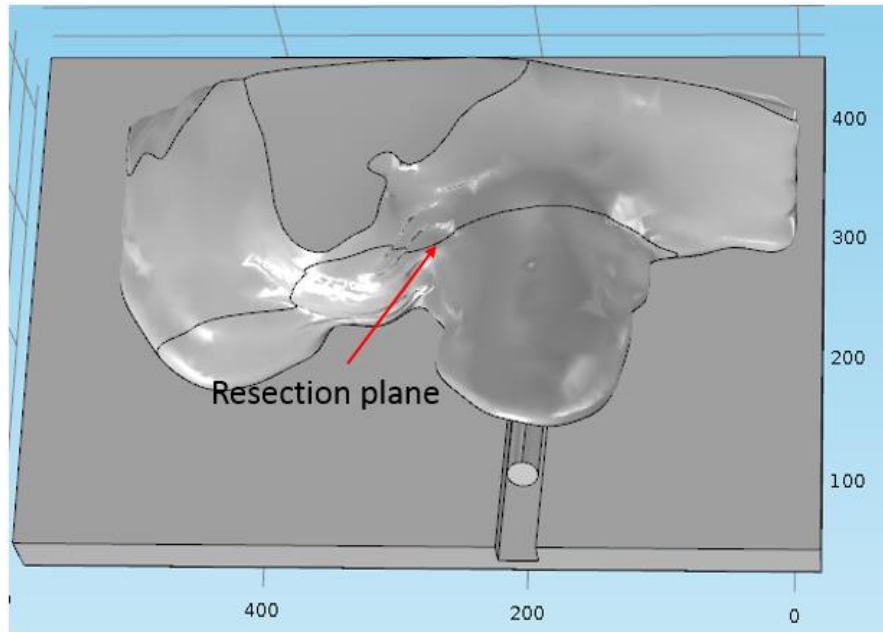
From the result, we confirm hyper-elastic model gave better accuracy than linear elastic model, especially when looked at the surface errors in figure II.19. Model type is the most significant factor affecting on the error of the model while modifying mesh type, Poisson's ratio or coefficient of friction could provide better result but not much. Decreasing Young's modulus could lead to convergence problems. We assumed it's because the liver's material at the contact points is the membrane, not the parenchyma of the liver as our model built.

The simulation model was used to solve the navigation problems in section 2:

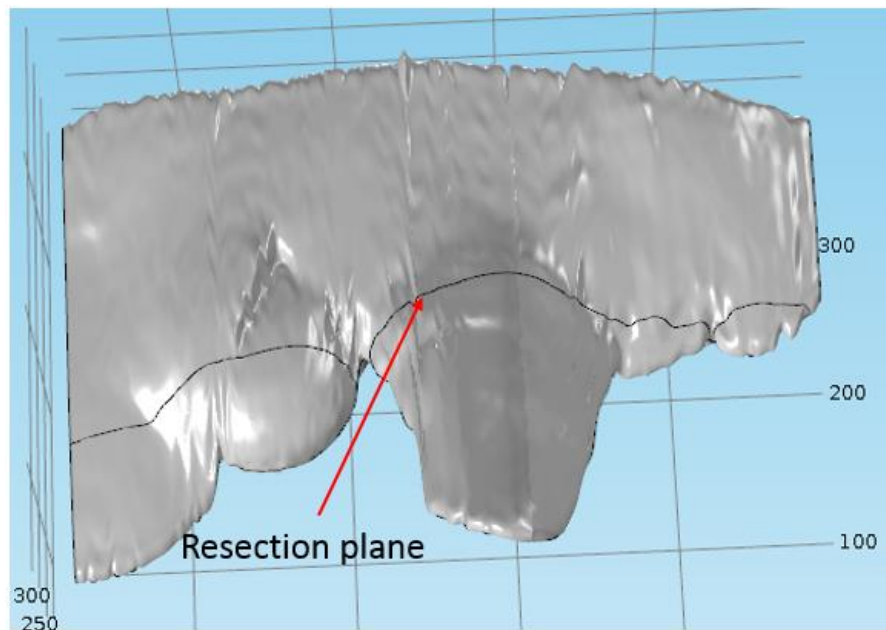
- (1) Addressing problem 1, we were able to reduce the-tumor centroid error to approximately 2 mm. The location of the tumor was also a boundary condition in problem 2.
- (2) For problem 2, we chose a resection plane that is perpendicular to the wire and 5 mm away from the tumor location in the inward direction. This virtual resection plane completely encompassed the left lobe of the liver containing the tumor only and continued across the gallbladder and the right side of the liver.



(a)



(b)



(c)

Figure II.24 Resection plane in (a) position A (b) position B using simulated model (c) position B using CT images

The percent volume of the tissue removed in position A was 15%. In position B using the simulated model, it was 16%, and in position B using CT images 17%.

The angle between the resection plane in the simulated model and the resection

plane in CT images was 4 degrees. Therefore, our model could predict the resection plane's position and the remaining volume of the resection quite close to the exact values.

Still, there are limitations to using the mechanical model to simulate the actual movement of the liver, as we do not yet fully understand the physics of the interaction between the liver and the lever. Moreover, the liver itself is heterogeneous in elastic properties. In our simulation, using a model with the same material for the membrane, parenchyma, vessels, and guidewire could not simulate the deformation properly. Though we assumed we could obtain intra-operative boundary conditions using the position of the lever and the guide wire, the experiment showed that getting them were challenging and they still did not provide enough information for the simulation. We planned to use other laparoscopic surgery techniques to rebuild the liver surface as an additional boundary condition.

4.5 Conclusion

Most of the current research using computational models for tissue deformation is attempting to solve the problem of liver motion tracking with new technology and algorithms. As we aim to keep our working goal as simple as possible, we have focused on the most important surgical questions – identification of tumor position, the optimal plane of resection and assessment of post-resection liver volume. Here we have presented one method that can be applied to liver resection operations and have shown that our model can track the liver and tumor with sufficient accuracy.

Our method still needs to be improved by using heterogeneous model and surface imaging so it can account for the changing conditions found during actual operations. The next chapter will introduce a new method to acquire liver surface information.

Chapter 5

New method for going from 2D- endoscope to 3D-acquisition of surface landmarks by software

This chapter presents a method to use the Smart Trocar to acquire intra-operative surface data. Section 5.1 introduces the topic and literature review. Section 5.2 describes the key instruments of the method, the Smart Trocars. Section 5.3 gives details about the method and mathematical theory of it. Section 5.4 and Section 5.5 are about validating our techniques in a controlled environment with plastic model and testing our hypodissertation about respiratory motion on a living pig model. The content of this chapter comes from our publication [64].

5.1 State of the art

Our approach to solving the problem of tissue deformation during surgery is to build a biomechanical model of the liver based on the pre-operative image, then register it to intra-operative data as boundary constraints for the model. Therefore, obtaining intra-operative data would be a crucial step in surgical procedures. A stereo laparoscope is a favorite tool for this task, but due to financial constraints, not many institutions can afford such expensive equipment. Hence, it is essential to consider low-cost techniques with the ability to perform the tasks of a 3D scanner.

Swabbing the surface with a tracked stylus can be used to collect patient data for anatomical structures. Ma et al. [44] used a six-degree-of-freedom mechanical pointer instrumented with a sharp tip probe (Faro Technologies, Lake Mary, Florida) to swab the anatomy. Logan W. Clements et al. [45] employed an optically tracked probe (OPTOTRAK 3020, Northern Digital, Waterloo, Ontario) to acquire anatomical fiducial data to initialize surface-based image-to-physical space registration. The advantage of this technique is the familiarity that the surgeons have with this tool, as it is already utilized in image-guided surgery. However, the accuracy of these registrations is compromised due to the deformation of the tissue from contact with the stylus or from the stylus losing touch with the surface while swabbing.

Instead of using a physical probe, laser range scanning (LRS) uses laser light to determine the position of three-dimensional points in space [46]. It creates a depth map of the tissue surface via the triangulation mechanism: a laser light is

projected onto the surface, its reflection is collected by a sensor called charge-coupled device (CCD) and the location of the surface can be computed using the trigonometric relationship between the laser emitter and CCD. The accuracy of LRS is comparable to traditional fiducial-based registration, and LRS can be used in laparoscopic surgery [47].

Conoscopic holography is another non-contact technique to measure the distance to the surface. The conoprobe emits a laser light and immediately receives its reflection along the same ray path through a conoscopic crystal. The diffraction pattern between emitted and reflected laser light can be analyzed to compute the surface location [48]. This technique can also be deployed through a laparoscopic port [49].

Structured-light 3D-scanners project stripes of light onto a surface. By analyzing the distortion of those lines, the geometry of the surface can be reconstructed [24]. The advantage of this technique is its ability to scan the entire field of view at once instead of sequentially scanning one point at a time. Therefore, it provides the results faster and reduces the confounding effect of the surface's motion. To predict the organ deformation during breathing, Luc Soler et al. at IRCAD used structured light to track skin surface movements [50].

Technique	Field of view	Cost	Accuracy
Laser scanner	Local	Moderate	~0.01 mm
Stereo-laparoscope	Non-local	High	~0.1 mm
Conoscope	Local	High	~0.01 mm
Structured light	Non-local	Low	~1 mm
Our method	Non-local	Very low	~1 mm

Table 2 State of the art for surface imaging system

Those techniques usually require specific pieces of high-tech equipment or make significant changes to the OR setup. Our method, which combines the inexpensive Smart Trocar [26] technology with standard 2D laparoscope, can do the same work without altering the conventional surgical instruments. Specifically, we use the capacity of the Smart Trocar to localize laparoscopic instruments going through the trocar in the three-dimensional coordinate space of the operating room [25]. (We could have used alternative technology based on ultrasound or accelerometer [51-53] that would provide the same level of accuracy on instrument localization.) The salient feature of our method is to combine two successive views through the laparoscope at different angles with the 3D-localization of a fixed tool at one single location to emulate a stereotactic system and compute the 3D-coordinates of surface landmarks. Our focus is to provide a depth map of a region of interest and measurements in the three-dimensional space to estimate the volume of tissue removal thus assisting the surgeon with a plan of resection at a critical time point during surgery (see [54, 63] and its references), rather than to offer real-time 3D-vision companion via virtual reality.

5.2 Smart Trocar

The Smart Trocar was developed initially as a simple solution to identify laparoscopic instruments to reconstruct the timeline of high volume standard laparoscopic surgery such as cholecystectomy, appendectomy, and bariatric surgery accurately. The idea was to use computer vision from the trocar point of view to avoid line view of obstruction [26].

Practically the Smart Trocar can be a ring fitting all trocar sizes that contains the camera, the battery and the electronic components for wireless communication with the computer system that analyze the data in real time – see Figure II.25. For instrument recognition, a separate perforated color marker is attached to a standard laparoscopic hand instrument near the handle. Each marker is color-coded for a particular instrument. By using a computer vision algorithm developed in our lab, the computer recognizes the pattern of color markers and correlates it to a library of registered instruments [26]. It is important to acknowledge that the system is unobtrusive to the operator.

We eventually found some additional services that can be provided by the same hardware system. First, because the size of the wheel is known, the distance between the wheel and the trocar can be computed based on the size of the wheel in the image. Therefore, we can calculate the position of the surgical instrument in the coordinate system attached to the trocar, including the small angle formed by the tool axis and trocar. Second, since the trocar has identified the instrument, we know the length of the tool and can compute the position of the tip of the instrument in the coordinate system of the trocar.

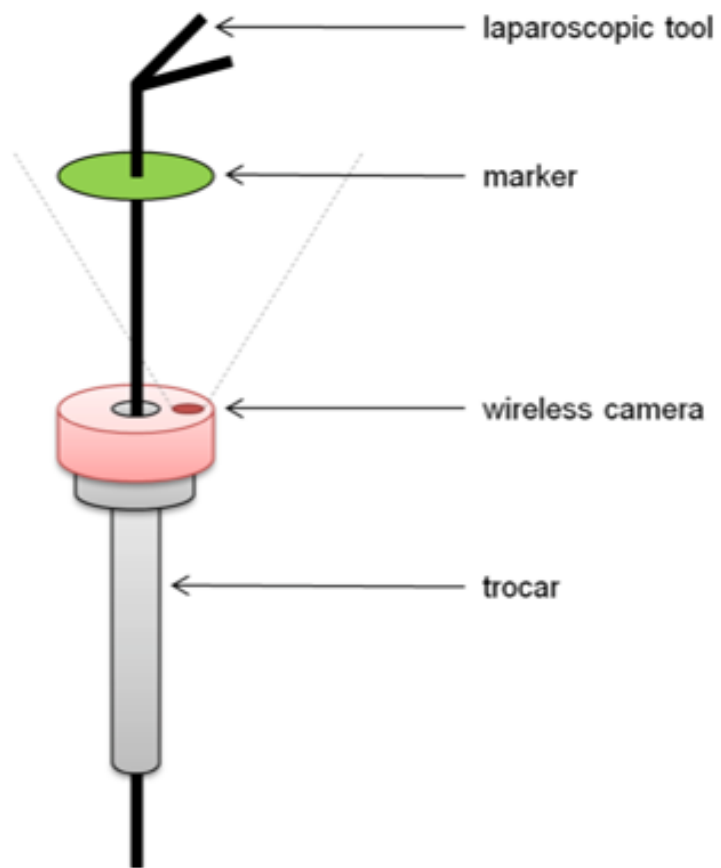


Figure II.25 Concept of the Smart Trocar

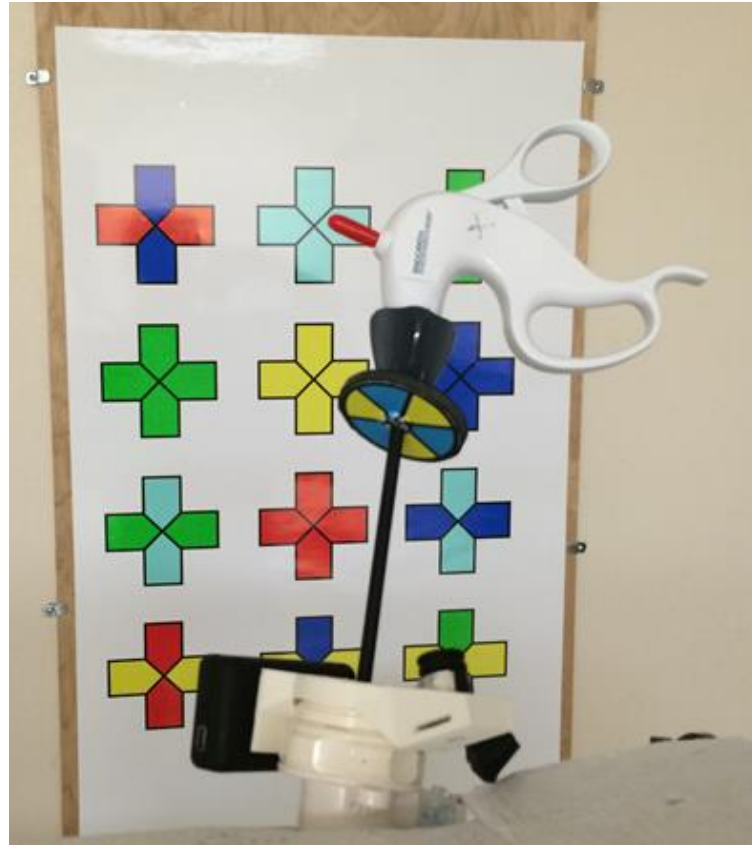


Figure II.26 Smart Trocar prototype with camera attached and colored marker

Third, the camera can monitor external fixed features of the OR environment that would be in the field of view of the camera independently of the laparoscopic instrument itself. To take advantage of this feature, we place specific landmarks that are easily recognized by a camera, such as standardized images of crosses, on the ceiling or the wall – see Figure II.26-. By capturing the crosses through the camera, we can extract from the video the trajectory of four fixed points in the operating room coordinate system that correspond, for example, to the corners of the crosses. This trajectory corresponds to the motion of the trocar. Based on trigonometry, we can quickly calculate the location and angle of the trocar between two camera views. Assuming a pinhole camera

model, the paper written by Yuan in 1989 [55] demonstrates that there is a unique solution to this problem, however, in practice our algorithm only works in a robust and reliable manner if we have an initial guess that is close enough to the solution. Hence, we have set up an initial database that covers all the possibility of the crosses' position. The Smart Trocar works therefore on video and can be considered as a GPS system for the OR.

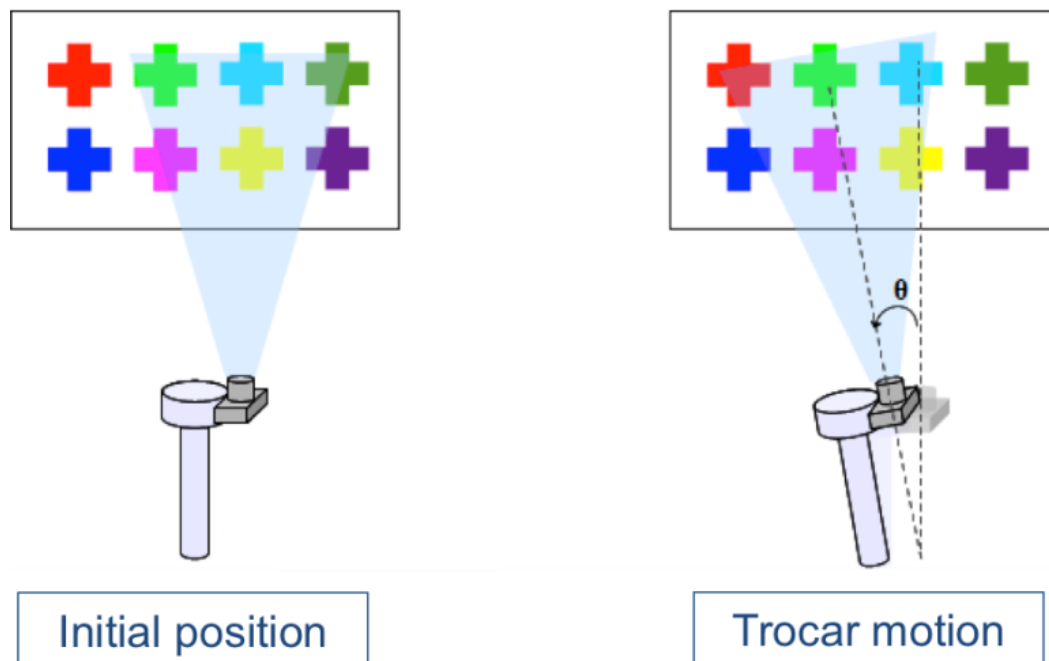


Figure II.27 Smart Trocar can obtain its position in 3d-coordinate space by capturing trajectory of the crosses through the camera

We found the system relatively robust to obstruction of the view since only a few of the landmark points were needed for registration of the system. It was also confirmed that the position of the trocar in the operating room's three-dimensional coordinate space is accurate within a millimeter and the angular orientation of the trocar is within two degrees. More detailed can be found in the master dissertation of Guillaume Joeger [25].

Combining all features, we can obtain the coordinate of the tip of the laparoscopic instrument in the three-dimensional system of the operating room.

We also notice that it is feasible to get an accurate localization of the trocar with a wireless gyroscopic electronic system or ultrasound system [51-53, 55]. However, our computer vision system can simultaneously provide the identification of the instrument and its localization.

In the following sections, we will assume, once and for all, that the tool localization system is available through our technology or any other means and will show that we can derive from this a standard two-dimensional laparoscope the 3D surface reconstruction of the soft tissue surface that is in the field of view of the laparoscope.

5.3 Method

5.3.1 Basic Principle and Set Up

Our method is based on the following basic principle: if we know one fixed point on the surface of the Region Of Interest (ROI), direction and head of the laparoscope camera in two different positions taking the images of the fixed point, then we can compute coordinates of any point on that surface. For the method's setup, two Smart Trocars are deployed on two sides of the patients. A surgical instrument having a color marker (M1) is inserted through one of the trocars (T1). It plays the role of a stylus in this setup. A laparoscope having another marker (M2) is inserted through the other trocar (T2).

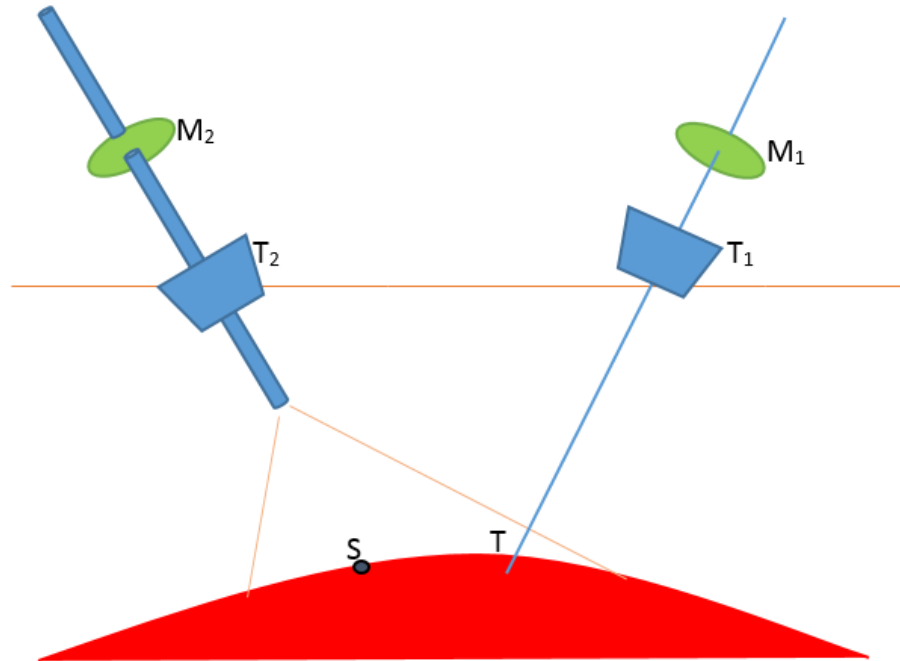


Figure II.28 Setup of the concept

To obtain the coordinates of a point of interest (S) on the tissue's surface, the user first touches the surface at point T using the surgical tool and records the first image. Then s/he moves the laparoscope so that it can capture the image of the tool and the surface again at a different angle as the second image. This allows the computer to determine the location of those interest points using the two images and data from the Smart Trocar. The method works for any specific landmark that can be identified in both images. In the next section, we will provide the mathematical construction of the 3D-surface reconstruction.

5.3.2 Mathematics of the concept

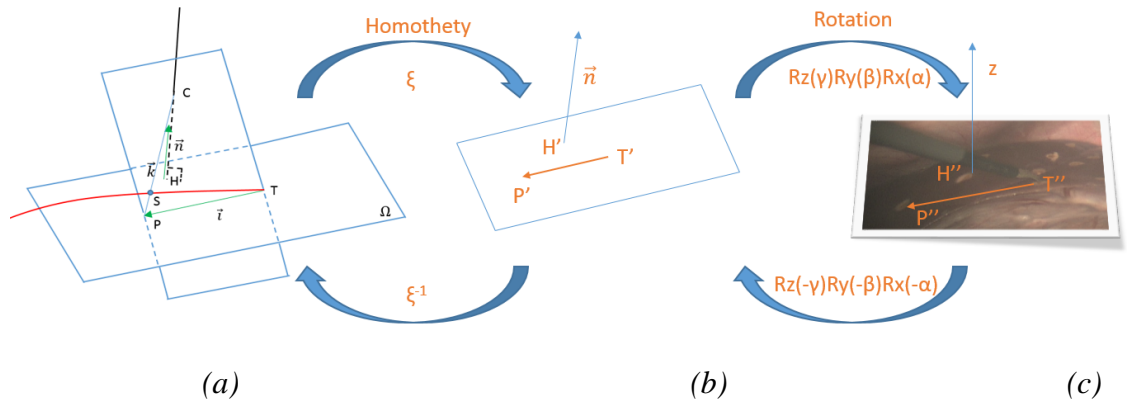


Figure II.29 Successive bijective transformations between the plane Ω and the image acquired by the laparoscope: first an homothety with scaling factor ξ to relate pixel size to physical size and then a rotation.

The Smart Trocars and the laparoscope provide first the:

- coordinates of the tool tip $T(T_x, T_y, T_z)$
- coordinates of the laparoscope tip $C(C_x, C_y, C_z)$
- direction vectors of the camera stick $\vec{n} \vec{l}(n_x, n_y, n_z)$

Let HT be the segment in the physical space that connects the projection H of the point C which is the “head of the laparoscope” along direction \vec{n} on the surface to the tip denoted T of the instrument laying on the surface. HT can be easily computed from the Smart Trocar information above. Let (S_x, S_y, S_z) the coordinate in the three dimensional space attached to the OR that we would like to compute.

We retrieve first the scale of the homothety from the (pixel) coordinate of segment $H'T'$ in the laparoscope image – see Figure II.29c, with:

$$\xi = \frac{|\overline{HT}|}{|\overline{H'T'}|}$$

To be more specific, H' is the center point of the image, and T' corresponds to the pixel that is the closest to the tip of the laparoscopic tool.

From the direction \vec{n} of the laparoscope instrument, we can compute the element of the rotation to go from Figure II.29b to Figure II.29c.

Let P be the projection of S along direction \vec{n} on plane Ω , and P'' the corresponding point in the laparoscope image. The plane Ω in the physical space is perpendicular to the laparoscope axis and go through the fixed point T provided by the tip of the laparoscopic tool. Using the inverse of the successive transformations defined in Figure II.29, we can compute the segment TP and therefore the three dimensional coordinate in the physical space of the projection point P . S is now standing on the straight line PC that is completely known.

For any position of the laparoscope, we have then an algorithm to compute the projection point P of S along the direction of the laparoscope and in the plane perpendicular to that direction that goes through the fixed point T .

It takes then two different positions of the laparoscope C , let's say C_1 and C_2 to obtain the position of the landmark S as an intersection of the corresponding straight lines P_1C_1 and P_2C_2 reconstructed by the procedure given above.

While this algorithm is quite simple, it requires that point T remains at the same position for these two images. It is also anticipated that the uncertainties of the image acquisition of the various key landmarks used in the process may affect the quality of the 3D-reconstruction.

We have proceeded then with a rigorous experiment using a solid surface that has significant curvature. In the next section, we report our experimental results.

5.4 Verification experiment

5.4.1 Setup

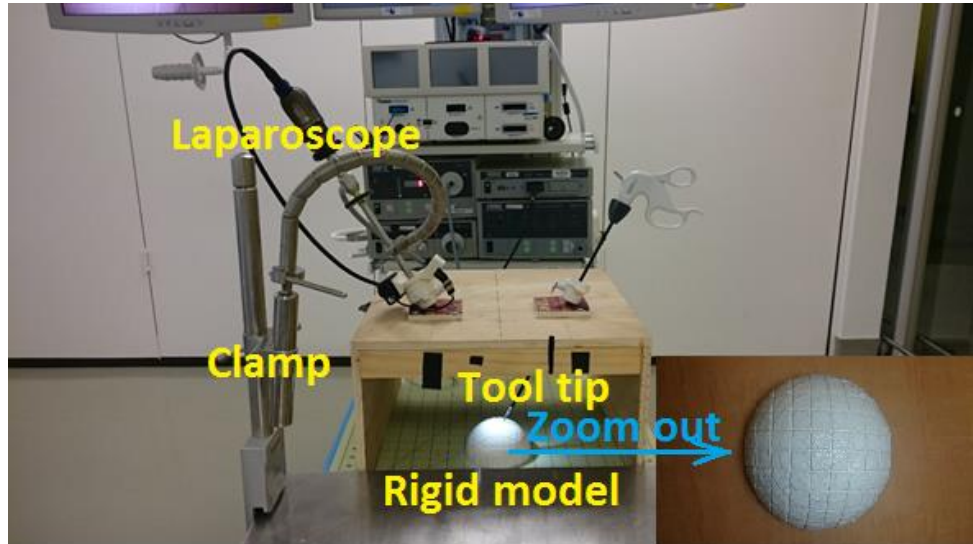


Figure II.30 Experiment setup using a clamp to hold the laparoscope. In right corner is 3D-printed model having the sharp of a half-sphere.

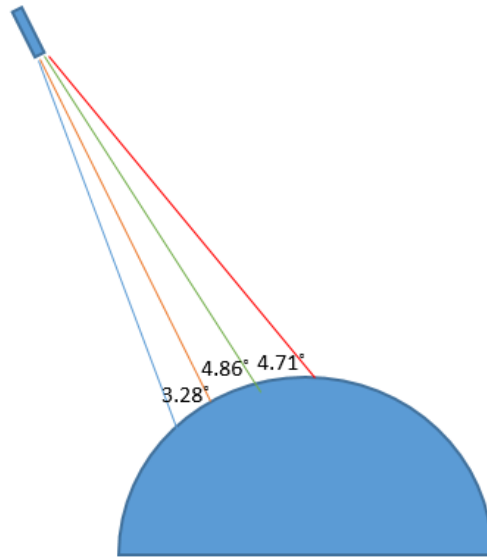
We built a box very similar to the standard Fundamental Laparoscopic Surgery (FLS) kit [56]. The FLS box was placed firmly on a measuring mat. Its edges were parallel to the table edge. A half 3D-printed plastic sphere model was put inside the box. The surface of the model was divided into 1-cm squares using vertical and horizontal lines for reference measurements. The coordinates of the model and interest points on it can be calculated based on the measuring mat and its geometry.

A surgical instrument and a laparoscope were inserted into the FLS box through the Smart Trocars. The tool pointed at the model and was able to maintain stable balance on its own. The laparoscope was held at a fixed position using a clamp.

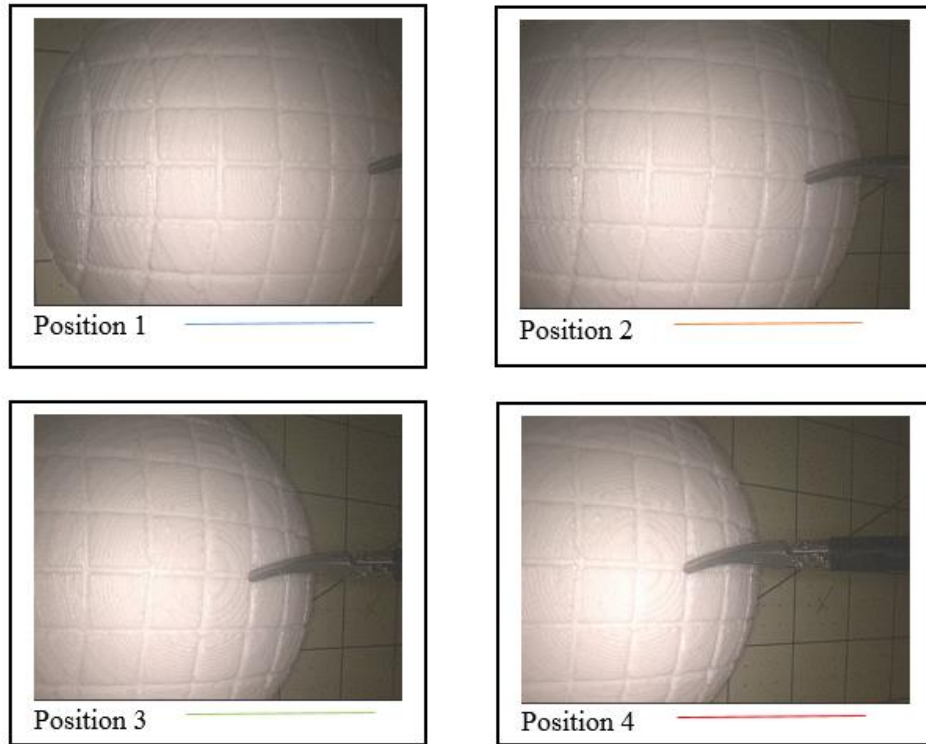
The laparoscope was used to take a series of images at different angles, making sure both the tooltip and most of the model can be seen in the images. The dimensions of images provided by the laparoscope are 1440 x 1080. In this setup, coordinates of the tool's tip, laparoscope's tip and angle of the laparoscope were extracted and computed using the Smart Trocars' video.

5.4.2 Results

The laparoscope took images of the model in 4 different positions. It was moved by an angle of 3.28 degrees from position 1 to position 2, 4.86 degrees from position 2 to position 3 and 3.71 degrees from position 3 to position 4.



a) Center lines from the laparoscope tips to the model in 4 different positions of the laparoscope



b) Images seen from laparoscope in 4 different positions
Figure II.31 The laparoscope took images of the model in 4 positions

For each position, six points of interest on the model surface were calculated using combinations of image pairs 1-2, 1-3, 1-4 then compared them with ground truth.

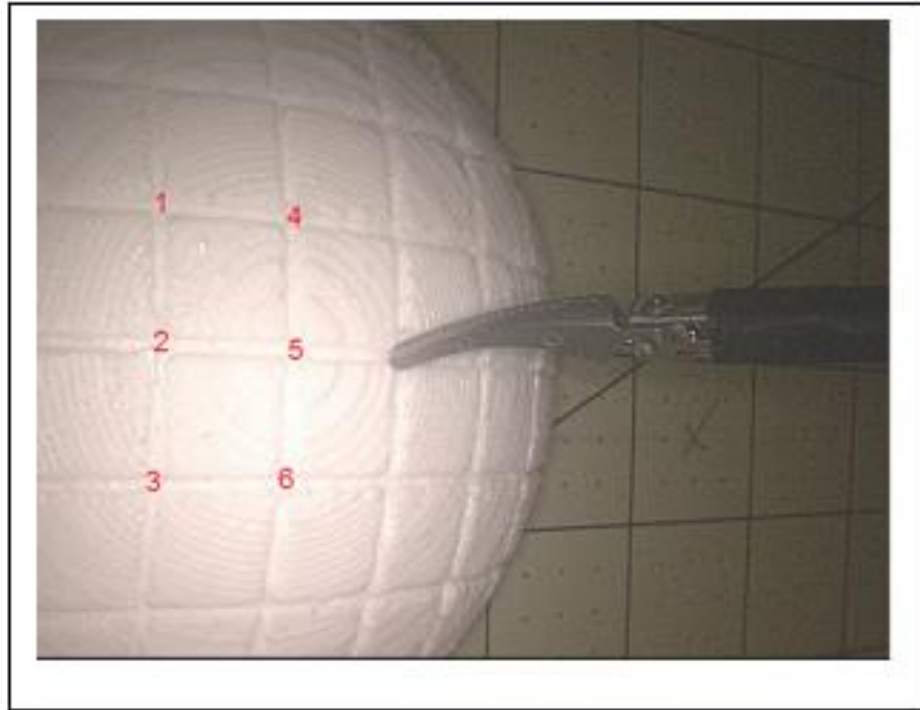


Figure II.32 Six interest points on the model surface needs to be calculated.

The result is displayed in Table 3. The absolute error of the interest points' coordinates was less than 2 mm on pair 1-3, 1-4 and around 6 mm on pair 1-2 due to the small angle of the laparoscope movement. Therefore, we can say this method had millimeter accuracy provided that the angle between two laparoscopic views is not too small. In real clinical conditions, we can anticipate, however, that the laparoscope is not entirely fixed in both positions, the surface of the tissue may move due to dynamic fluctuations of patient respirations and many other sources of perturbation. We will discuss these elements in the next section.

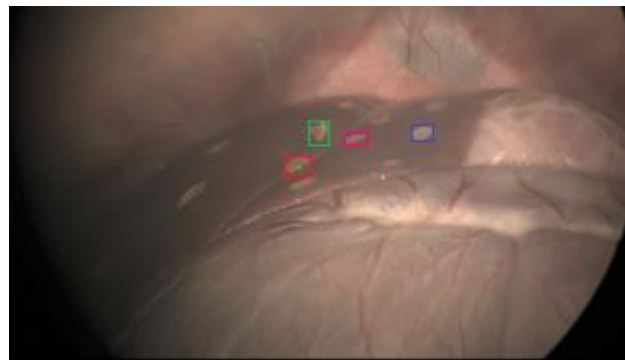
Pair	Point	Absolute error		
1-2		X(mm)	Y(mm)	Z(mm)
	1	1.9768	2.2111	7.5828
	2	1.0365	0.1778	6.4199
	3	1.6729	1.7831	8.0494
	4	3.0732	1.4165	5.4391
	5	2.4649	0.1361	4.4614
	6	3.2529	1.2773	6.0865
1-3		X(mm)	Y(mm)	Z(mm)
	1	0.205	0.0384	1.926
	2	1.7084	0.3689	0.3844
	3	1.1562	0.9459	1.0335
	4	0.152	0.1196	1.7845
	5	0.7377	0.0816	0.7914
	6	0.4847	0.5937	1.4029
1-4		X(mm)	Y(mm)	Z(mm)
	1	0.6378	0.1499	1.154
	2	2.0022	0.1379	0.1591
	3	1.5459	1.4729	0.3259
	4	0.5143	0.1504	1.2894
	5	0.232241	0.2094	0.4479
	6	0.9997	0.8683	1.0207

Table 3 Result of experiment on rigid model

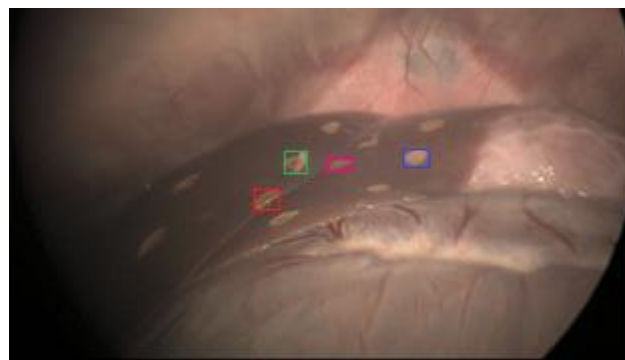
5.5 In vivo experiment and discussion

To test the method in vivo, we did an experiment with a living porcine model and the same setup of two Smart Trocars and a 2D laparoscope. The landmark points on the surface of the liver were marked using an electrosurgical unit so they could be recognized during different frames of the video.

Our primary concern was to assess the impact of breathing on the surface liver motion. It is well known that this movement can be quite significant but also unevenly distributed [50]. Figure II.33 below shows a representative example of two snapshots of the video at the endpoint of the breathing cycle.



(a)

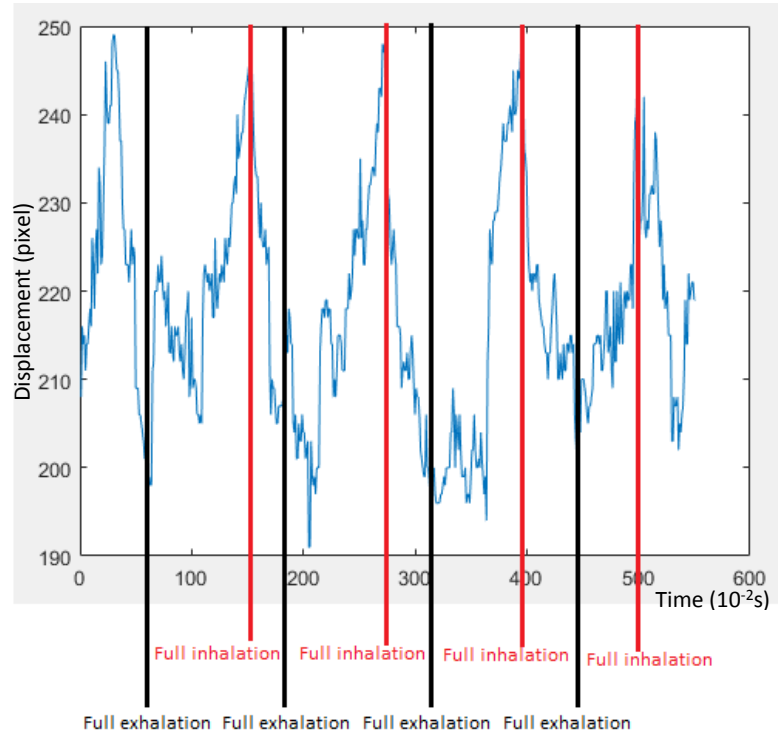


(b)

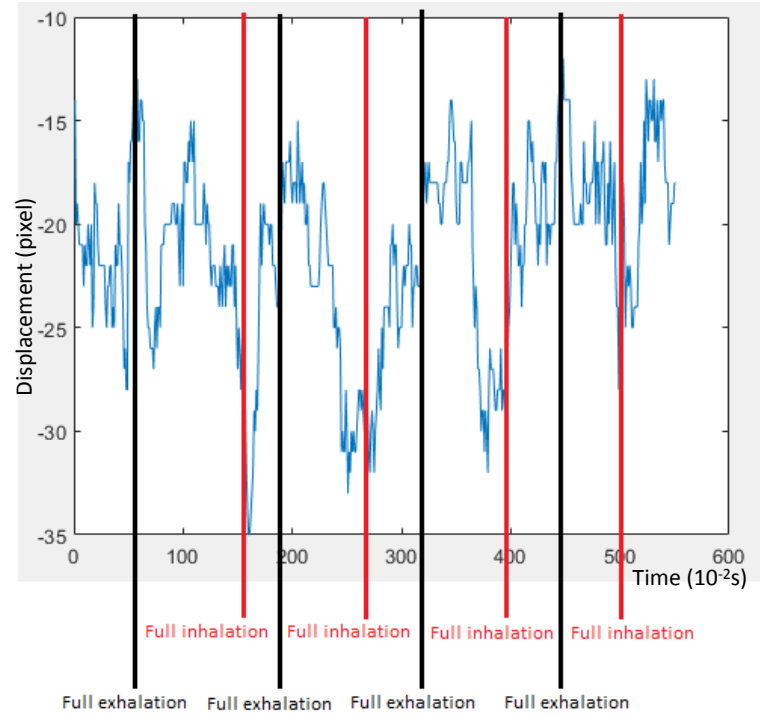
Figure II.33 Liver position and landmarks at (a) full exhalation and (b) full inhalation

There have been a number of publications that report innovative methods to reconstruct proper respiratory motion and its impact on internal organs in radiotherapy conditions [57-61]. However, here we observe the periodic motion from the laparoscopic camera directly. We hypothesized that the liver surface at a particular time frame in one period stayed about the same in that time frame in other periods. For example: whenever the pig exhales completely, the liver surface is always at one position. So by selecting only the images in that time frame of the period with different camera angles, we could apply our method and compute the location of those interest points.

Using our object tracking software on the video, we were able to collect the trajectories of the markers during the respiratory cycle.



(a)



(b)

Figure II.34 Time dependence of distance between two markers (purple and blue in Figure II.33) in (a) x-direction and (b) in y-direction

The displacement of the markers was about 2 mm between a full cycle of respiration (full exhalation to full exhalation) and 20 mm between a half cycle of respiration (full exhalation to full inhalation). To study the effect of these displacements on our method, we applied the same percentage of perturbation on the coordinates of images from the verification experiment reported in the previous section. Then we computed those six interest points again and compared the results to non-perturbation ones.

Non-perturbation	Point	Absolute error (mm)		
		X(mm)	Y(mm)	Z(mm)
	1	0.6378	0.1499	1.154
	2	2.0022	0.1379	0.1591
	3	1.5459	1.4729	0.3259
	4	0.5143	0.1504	1.2894
	5	0.232241	0.2094	0.4479
	6	0.9997	0.8683	1.0207
Half period of respiratory (perturbation 6.9%)	Point	Absolute error (mm)		
		X(mm)	Y(mm)	Z(mm)
	1	2.714	4.3976	0.9704
	2	3.452419	3.631768	0.609343
	3	3.3072	2.7025	0.9048
	4	2.2096	4.5727	2.2235
	5	2.8224	3.865	0.9032
	6	2.7129	2.6893	1.5485
Full period of respiratory (perturbation 0.7%)	Point	Absolute error (mm)		
		X(mm)	Y(mm)	Z(mm)
	1	1.3092	1.4058	0.3192
	2	2.3554	0.5236	0.0066
	3	1.8904	0.5641	0.2645
	4	0.8788	1.3533	1.7385
	5	1.4856	0.5235	0.529
	6	1.3616	0.6669	1.2116

Table 4 Effect of perturbation on the results from the verification experiment reported in the previous section

We have observed that an angular perturbation of the order of the one observed in the pig model mostly affected by the error in x and y directions because the perturbation only happened on the images which were nearly parallel with the Oxy surface. The robustness of this result is encouraging. In other words, if we take in account the respiratory motion and only use the images that correspond

roughly to the full inhalation or exhalation period, the error of our method might still be acceptable for a navigation system.

5.6 Discussion

This chapter discusses a new method of acquiring surface information by using a straightforward and inexpensive setup. This method can be applied to a significant number of surgical applications as a guidance system on its own or in conjunction with other navigation techniques. Laparoscopic liver surgery is probably one of the most challenging operations in that context. A standard set up should have even more than two Smart Trocars that we needed in our algorithmic construction.

Our method has three important functions for laparoscopic surgery:

- Using the instrument tip as laparoscopic navigation pointer: The instrument tip can localize visible features during the surgery such as the falciform ligament, round ligament, or inferior ridges. It can also palpate vessels, tumors, and organs to reveal information below the surface for control and guidance with location data.
- Drawing lines on tissue with accurate 3D-location: The surgeon can draw virtual resection line on the tissue to compute remaining tissue volume after resection. He/she can measure the distance between two points by drawing a line in between them and have it computed.
- Recovering 3D-surface information: The result of the method is a point cloud belonging to the surface. A registering technique can be used to

map the pre-operative data to these points thus creating a depth map of the tissue surface.

The preliminary testing result is encouraging, but it needs to be further verified with functional Smart Trocars in a surgical setting.

Chapter 6

Transition to human liver

6.1 Experiments on cadavers

To come closer to the goal of bringing our system to real liver surgery, we decided to transit to human liver experiments after achieving adequate accuracy on the porcine liver explant model. Additionally, we could also test our method of reconstructing the surface of the liver in Chapter 5 in a clinical setting. The only option to study the human liver at this stage of research is to use cadavers.

6.1.1 Method

The study took place in the hybrid operating room of the Houston Methodist Institute for Technology, Innovation & Education (MITIE). An Artis Zeego system can conduct the intra-operative robotic C-arm cone-beam computed

tomography (DynaCT) which can obtain the 3D-scans of the cadaver anytime during the experiment. It is also equipped with fluoroscopy imaging which can display the movement of the guidewire when it is inserted into the biliary duct.

Dr. Aman Ali, a resident of the Houston Methodist hospital, planned out the steps of the procedure as below:

1. Set-up laparoscopic towers and confirm that all equipment is functional
2. Obtain baseline pre-operative imaging
3. Endotracheal intubation:
 - a. Intubate the cadaver
 - b. Set up ventilator machine
4. Establish pneumoperitoneum
 - a. Use the Hassan technique to gain intra-peritoneal access using a supraumbilical 12 mm port.
 - i. If Hassan technique is unsuccessful, then use Veress needle in the LUQ of the abdomen.
 - b. Insert 2nd trocar for 2nd camera position (LUQ site)
 - c. Insert additional trocars for dissection

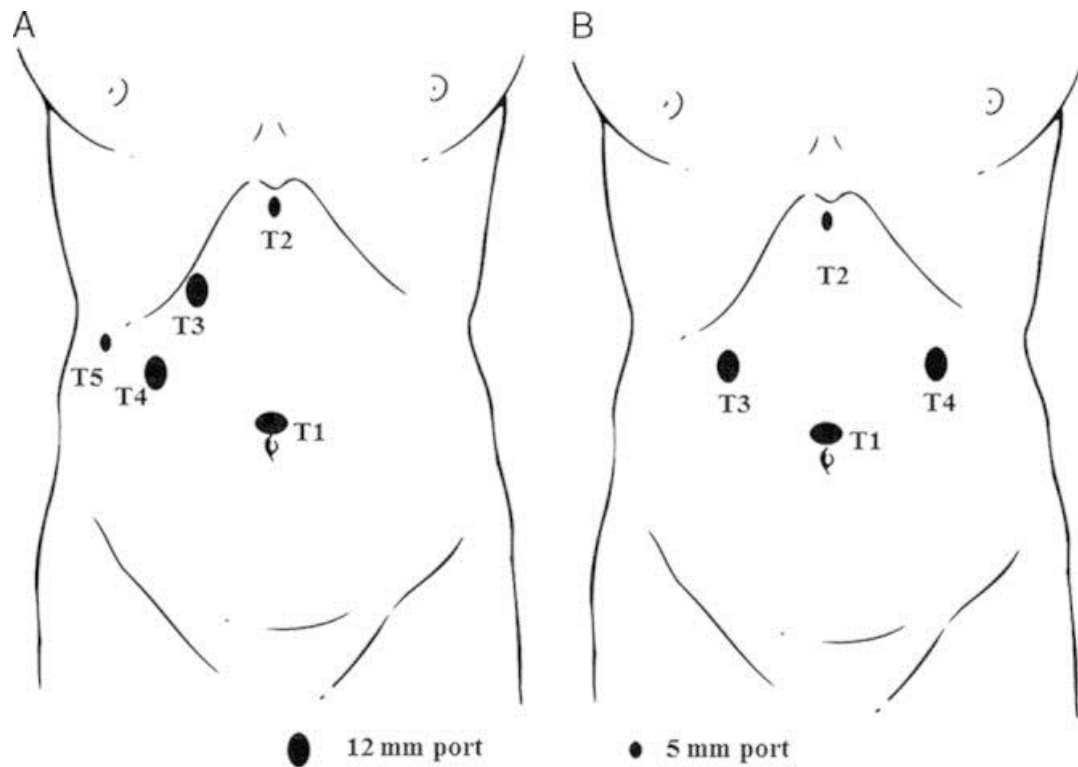


Figure II.35 Location of Smart Trocars on the patient abdomen

(A) right liver mobilization (B) left liver mobilization

5. Using electrocautery, mark the liver in a grid fashion to help account for respiratory variation. Record laparoscopic video for at least 1 minute to complete 8 respiratory cycles.
6. Perform duodenotomy to insert guidewire through papilla
 - a. Obtain imaging with guidewire
 - i. Perform fluoroscopy first to confirm desired wire position before obtaining CT scan.
 - b. Close duodenotomy with vicryl suture
 - c. If duodenotomy technique is unsuccessful, then find common bile duct and insert guidewire.

7. Right Liver Dissection:

- a. Medial to lateral approach: Dissecting cranial ligamentous attachment after identifying inferior vena cava and hepatic veins provides better exposure and prevents bleeding complications.
 - i. Dissection of falciform ligament to expose IVC.
 1. After dissection of the ligamentum teres and falciform ligament, the liver is gently pushed downward using an Endo-paddle
 - ii. Medial-to-lateral approach for cranial dissection of the liver.
 - iii. Caudal and posterior dissection of the liver to expose IVC. After completion of right lobe mobilization, the right side of the retrohepatic IVC is exposed.
8. Obtain imaging (x2) while mobilizing the liver at different angles at 0 degree and 30 degrees. The liver mobilization NEEDS to be recorded on two laparoscopic camera views simultaneously.
9. Resect desired portion of the right liver
10. Obtain post-resection imaging

Along with the experiment about the liver deformation and Smart Trocars surface reconstruction, we also tested the hypothesis of using a high-frequency ventilator to correct the respiratory motion. Please refer to Section 6.2 for detail.

6.1.2 Study in hybrid room

To simulate the breathing motion of the patient, a ventilator machine was used to keep the respiratory motion and the pressure in the abdomen at a fixed rate.



Figure II.36 Ventilator machine's display

Several landmarks were created on the surface of the liver using electrocautery for registration purpose.

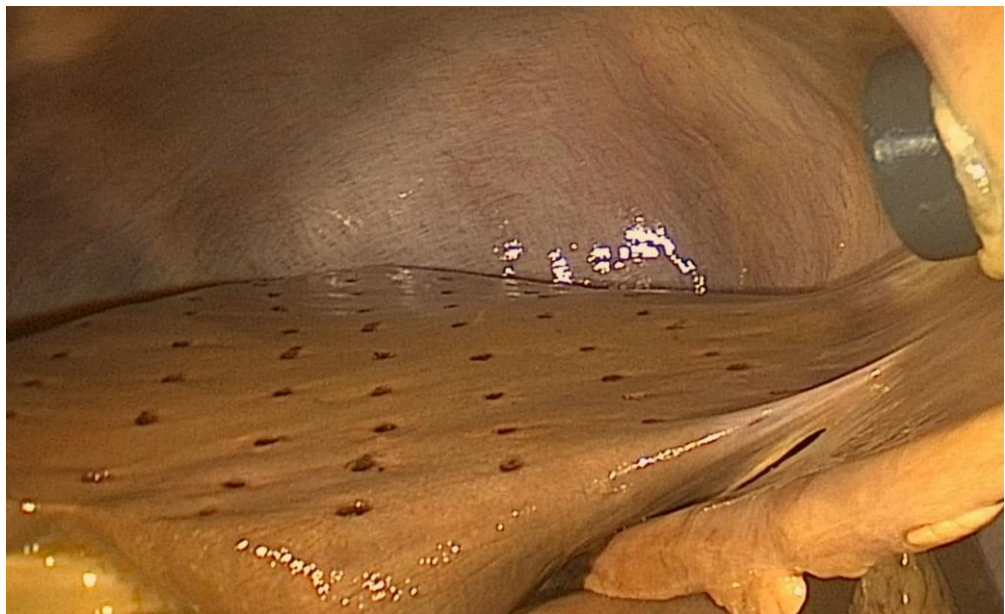


Figure II.37 Grid of markers on liver surface

Two laparoscopic cameras were used at the same time to take video of the liver surface during the respiratory motion.

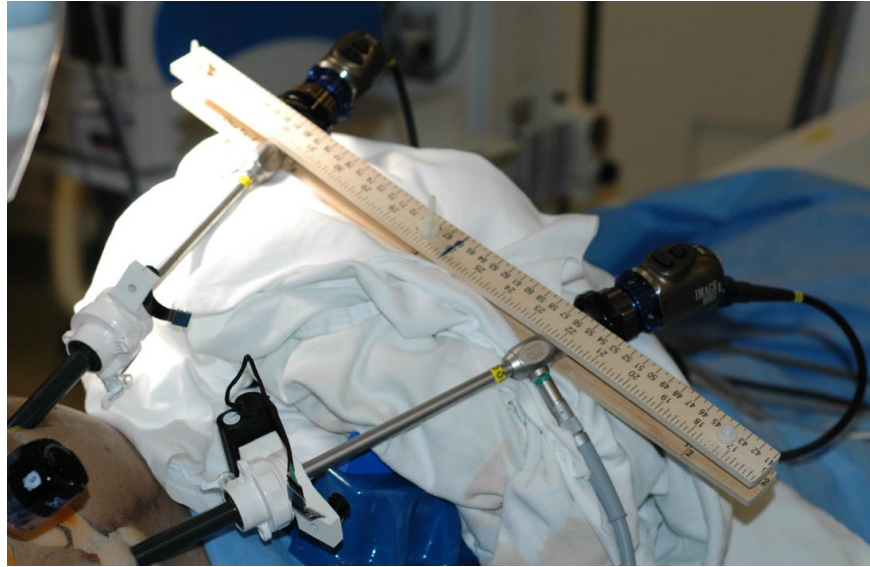


Figure II.38 Two laparoscopic cameras were used at the same time

The Smart Trocars were setup along with the posters to record the trajectories and locations of the instruments and the camera.



Figure II.39 The Smart Trocars were set up to record the trajectories and location of the instruments and the camera

The stent was inserted into the bile duct using an endoscope and deployed fully. The fake tumors were punctured through the liver surface, into the deformable portion of the liver.



Figure II.40 Fake tumors and stent deployed into the liver

The liver was lifted using a wooden stick and the stick position was recorded with the Smart Trocars. 3D scans of the liver were taken using the C-arm of the Zeego system at both states of the organ – before and after lifting.



Figure II.41 The liver lift with a wooden stick

6.1.3 Preliminary result

Even though it is difficult to see the organ boundary in the CT scans due to the artifact coming from the metallic instruments (stent, endoscope) and the gas within the cadaver, we were able to segment the liver from the rest of the images.



Figure II.42 CT scan of the cadaver's liver

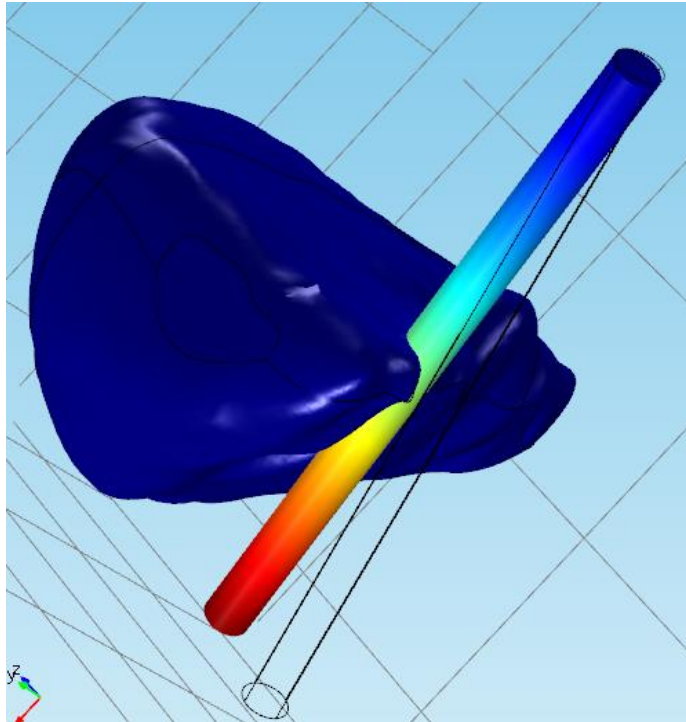


Figure II.43 Simulation in COMSOL software

We have started to build the deformable model of the liver based on segmentation of liver images in the neutral position. Using the software COMSOL, we were able to set up the same boundary conditions during the experiment.

6.2 New method for respiratory motion

correction

The content of this section mainly comes from our publication [65].

6.2.1 *Hypodissertation*

Many image-guided surgery techniques suffer from respiratory motion artifacts. Numerous studies have attempted to correct breathing motion using sophisticated computational methods. In Section 5.5, we tried to compensate the breathing motion by using the image at only full exhalation or full inhalation of the breathing cycle. But that method still added another layer of complexity on top of our deformable method, creating unnecessary overhead computation and error. Hence, we chose another approach that addressed the problem using a conventional surgical equipment. Our hypodissertation is that high-frequency ventilation (HFV) will minimize the effect of respiratory motion on image guided surgery.

6.2.2 *Method*

We compared standard ventilation versus HFV on a cadaver during simulated minimally invasive liver surgery. Landmark points on the liver surface were created to allow tracking during different video frames (Figure II.44).

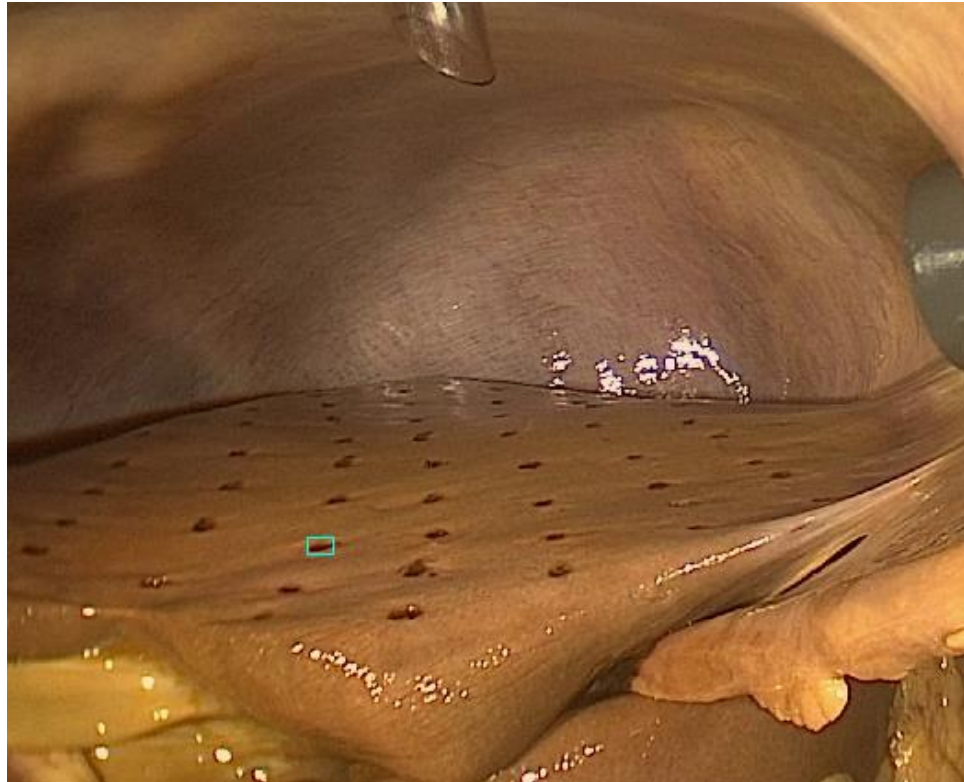


Figure II.44 Markers on the liver surface tracked with software

The cadaver was then ventilated using varying modes of conventional ventilation (tidal volume, respiratory rate) versus varying frequencies of HFV. Novel tracking software was used to analyze the videos and record the trajectories of the liver markers throughout the respiratory cycle. The liver motion was measured in millimeters (Figure II.45) and, in the case of HFV, plotted against the respiratory rate (Figure II.46).

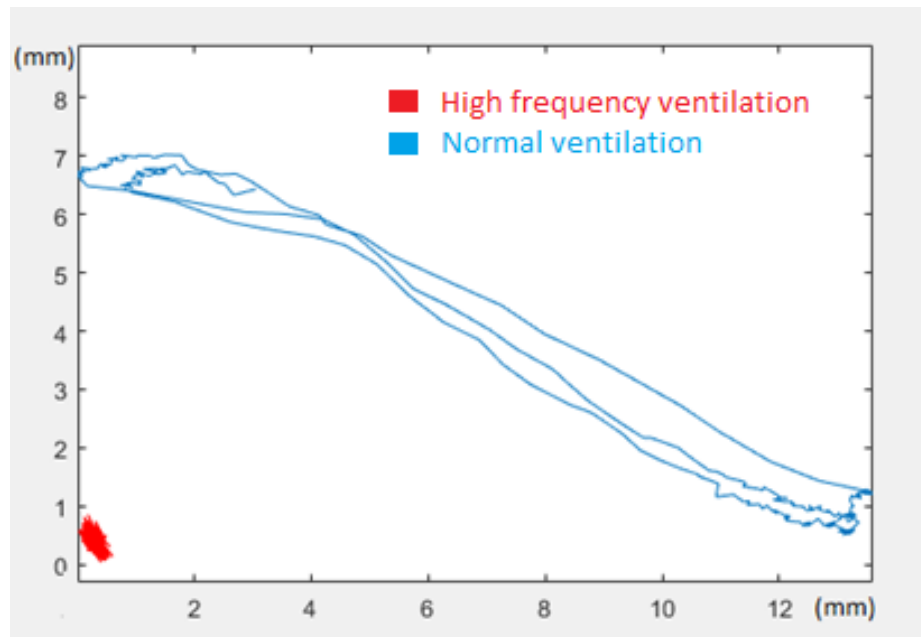


Figure II.45 Trajectory of one marker: High-frequency versus normal ventilator

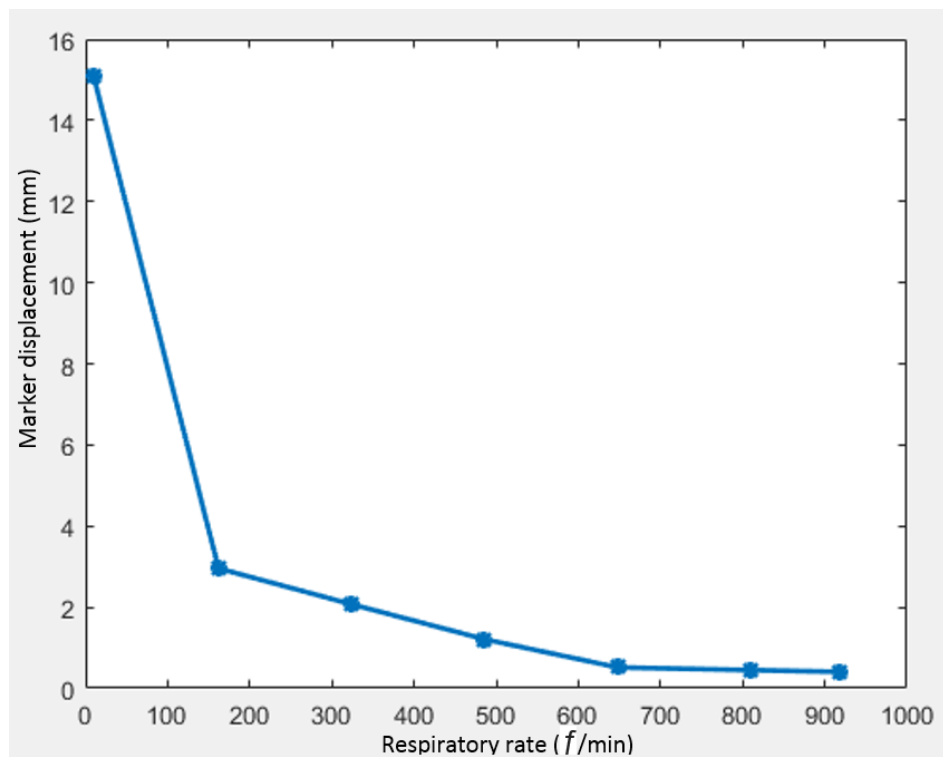


Figure II.46 Marker displacement versus respiratory rate in case of HFV

6.2.3 Result

Displacement of the liver markers from full inhalation to full exhalation was 15 ± 2 mm using the lowest respiratory rate during standard ventilation ($tV = 800$ mL, rate = 10 b/min, PEEP = 10 cmH₂O). When using HFV, the displacement decreased as the respiratory rate increased with a clinical plateau at greater than 648 breaths/min or 10.8 Hz (Figure C). Above this frequency, the markers appeared stagnant on the laparoscopic view.

6.2.4 Conclusion

High-frequency ventilation (HFV) eliminates respiratory motion and can be maintained for many hours. It has the potential to revolutionize image guided surgery because it can be applied on top of many techniques that suffer from breathing motion. Our method to reconstruct the liver surface using the Smart Trocar can benefit from this finding.

Part III

Dissertation review

Chapter 7

Conclusion and future work

The aim of this work was to develop an image-guided system that helps surgeons to align the points within the organ across multiple imaging modalities. For this purpose, the dissertation focused on the development of finite-element models of liver deformation under operational conditions. These predictive tools are of potential use in the clinical setting for tracking internal tissue movement and decide the resection plane during the surgery.

This dissertation established the framework for the guidance system which components are combined in a workflow that goes from input data to output results. We focused first on developing experiments on the porcine liver explant to validate the modeling techniques, then on obtaining the surface reconstruction of the liver as intra-operative data, and finally on the analysis of in-vivo human liver studies.

7.1 Validation of the tissue mechanics

The development of finite-element models of liver deformation under operational conditions is the core of the guidance system. In this dissertation, we show a method for the localization of the position of both the liver and a tumor within it during a minimally invasive liver operation. From pre-operative CT scans, the liver volume, and its internal structures were segmented using image-processing techniques. Based on these segmentations, a three-dimensional mechanical model was built to compute the liver volume and the internal structures displacement under boundary conditions aimed to mimic the influence of external forces imposed by the surgical instrument. This greatly facilitates the surgeon in the understanding of the motion of internal structures while manipulating the liver.

To validate our method, an experiment on a porcine liver explant was performed to assess the difference between actual tissue motion and the mechanical model. We based the validation on the comparison of two key aspects: the simulated tumor position and the distance between resection planes. The results showed that the mechanical model could predict the position of the simulated tumor during liver deformation with a 2 mm accuracy compared to the real-time fluoroscopic imaging. On the other hand, the difference between the resection plane in the simulated model and the resection plane on rotational images is 4 degrees.

The use of internal fiducial markers and computer modeling allowed us to successfully track the position of a liver tumor with millimetric accuracy during organ deformation. We also succeeded in maintaining an accurate prediction of the

plane of surgical resection and in calculating the mass of residual liver following the resection correctly. The use of this model during minimally invasive liver surgery has the potential to maintain the accuracy of the fused images longer than the current conventional methods making the procedure safer and reducing the need for repeated intra-operative scanning.

7.2 Liver surface reconstruction using Smart Trocars

In order to enrich the deformable model with another intra-operative information, we developed a method to use the Smart Trocar to acquire intra-operative surface data. Due to its ability of instruments localization, a system of two Smart Trocars and one 2D laparoscope pointed out visible features during the surgery and acquired their location in 3D for the registration system. A single reference point obtained with this method allowed the computation of a depth map within the region of interest. Consequently, our method based on the Smart Trocar technology transformed a standard laparoscope system into a system with three-dimensional registration capability.

An experiment on a plastic model using the FLS box was performed to assess the accuracy of the method. The results showed that we attained millimetric accuracy when the angle between two laparoscopic views was not too small. Also, this method was proved to be robust even if we took in account the respiratory motion when we only selected the images at a particular time frame in one period.

This method can be applied to a significant number of surgical applications such as laparoscopic-navigation pointer, 3D-pen for drawing lines for measuring purpose, etc.

7.3 Future works

At the current stage, we have conducted two studies on cadavers. Due to the complexity of the in-vivo experiments, we still need to repeat the study using improved protocol that can be performed by:

- Using endoscopically placed biliary internal fiducial markers, surface markers, and a novel surface contrast to verify the deformable model
- Investigating high-frequency ventilation versus standard ventilation to eliminate respiratory motion during image guided surgery
- Investigating the resolution of rotational imaging by using HFV versus standard ventilation
- Using HFV to quantify improved image resolution during image guided surgery
- Further investigating novel surface contrast to highlight boundaries between abdominal structures

For the tissue mechanics and registration process, the idea is to reduce the region of interest of the liver by using invariant planes. In this way, the complexity of the model will be significantly reduced while the fundamental problems of surgical navigation: the location of tumor and plane of resection will still be addressed.

7.4 List of publications

[63] T. Nguyen, A. Huang, V. Fikfak, B. Dunkin and M. Garbey, “Image-guided simulation of tissue deformation using a mechanical model on a surgical application,” *Computer Methods in Biomechanics and Biomedical Engineering*, DOI:10.1080/10255842.2016.1214269, 2016.

[64] M. Garbey, T. Nguyen, A. Huang, V. Fikfak, B. Dunkin, “A method for going from 2D endoscope to 3D acquisition of surface landmarks by software,” *submit to International Journal of Computer Assisted Radiology and Surgery*, 2016.

[65] Aman B. Ali, Toan B. Nguyen, Marc Garbey, Brian J. Dunkin, “High frequency ventilation eliminates the need of respiratory motion correction in image-guided surgery,” *submit to SAGES*, 2016.

[66] Toan B. Nguyen, Aman B. Ali, Marc Garbey, Brian J. Dunkin, “Use of internal fiducial markers and computer modelling to aid image-guided liver surgery,” *submit to SAGES*, 2016.

Bibliography

- [1] W. S. Eubanks, L. L. Swanstrom and N. J. Soper, *Mastery of Endoscopic and Laparoscopic Surgery*, Lippincott Williams & Wilkins, 2000.
- [2] T. Young Fadok, "Advanced Laparoscopic Colorectal Surgery," in *The ASCRS Textbook of Colon and Rectal Surgery*, Springer, 2011, pp. 597-623.
- [3] I. L. S. Site. [Online]. Available: <http://www.indialaparoscopysurgerysite.com/>.
- [4] A. C. Society, "Cancer Statistics Center," [Online]. Available: <https://cancerstatisticscenter.cancer.org/#/>.
- [5] "Liver Anatomy at eMedicine," [Online]. Available: <http://emedicine.medscape.com/>.
- [6] Websurg, "Websurg the e-surgical reference," [Online]. Available: <http://www.websurg.com/>.
- [7] F. H. Netter, *Atlas of Human Anatomy*, 2014: Saunders.
- [8] R. Assistant, "Anatomy of the liver segments," [Online]. Available: <http://www.radiologyassistant.nl/en/p4375bb8dc241d/anatomy-of-the-liver-segments.html>.
- [9] J. Invins and J. Porril, "Everything you always wanted to know about snakes (but were afraid to ask)," Sheffield, England, 2000.
- [10] N.H.Kim, *Introduction to nonlinear finite element analysis*, Springer, 2012.
- [11] G.A.Holzapfel, *Nonlinear solid mechanics: A continuum approach for engineering*, Wiley, 2000.
- [12] L.Malvern, *Introduction to the mechanics of a continuous medium*, Prentice-Hall, 1969.
- [13] E. Samur, M. Sedef, C. Basdogan, L. Avtan and O. Duzgun, "A Robotic Indenter for Minimally Invasive Measurement and Characterization of Soft Tissue Behavior," *Medical Image Analysis*, vol. 11, no. 4, p. 361–373, 2007.
- [14] Y. Lim, D. Deo, T. P. Singh, D. B. Jones and S. Suvaranu De, "In Situ Measurement and Modeling of Biomechanical Response of Human Cadaveric Soft Tissues for Physics-Based Surgical Simulation," *Surg Endosc*, vol. 26, no. 3, p. 1298–1307, 2009.
- [15] A. Black and M. Isard, *Active contours*, Springer, 2000.

- [16] T. F. Chan and L. A. Vese, "Active contours without edges," *IEEE Transactions on Image Processing*, vol. 10, no. 2, pp. 266-277, 2001.
- [17] R. C. Gonzalez and R. E. Woods, *Digital image processing*, Prentice Hall, 2008.
- [18] S. M. Lankton, "Localized statistical models in computer vision," PhD Dissertation, School of Electrical and Computer Engineering, Georgia Institute of Technology, 2009.
- [19] A. Yezzi, A. Tsai and A. Willsky, "A fully global approach to image segmentation via coupled curve evolution equations," *Journal of Visual Communication and Image Representation*, vol. 13, pp. 195-216, 2002.
- [20] H. G. Kenngott, M. Wagner, M. Gondan and F. Nickel, "Real-time image guidance in laparoscopic liver surgery: first clinical experience with a guidance system based on intraoperative CT imaging," *Surg Endosc*, vol. 28, p. 933–940, 2014.
- [21] W. Y., D. C. Rucker, R. H. Conley, T. S. Pfeiffer, A. L. Simpson, S. K. Geeverghese and M. I. Miga, "Registration of Liver Images to Minimally Invasive Intraoperative Surface and Subsurface Data," *SPIE Proceedings*, vol. 9036, 2014.
- [22] N. Haouchine, J. Dequidt, I. Peterlik, E. Kerrien and M.-O. Berger, "Image-guided Simulation of Heterogeneous Tissue Deformation For Augmented Reality during Hepatic Surgery," *IEEE International Symposium on Mixed and Augmented Reality*, p. 199 – 208, 2013.
- [23] N. Haouchine, J. Dequidt, I. Peterlik, E. Kerrien and M.-O. Berger, "Towards an Accurate Tracking of Liver Tumors for Augmented Reality in Robotic Assisted Surgery," in *ICRA*, Hong Kong, 2014.
- [24] D. Fofi, T. Sliwa and Y. Voisin, "A Comparative Survey on Invisible Structured Light," in *SPIE Electronic Imaging - Machine Vision Applications in Industrial Inspection XII*, San Jose, 2004.
- [25] G. Joerger, *Operating Room Awareness and Supervision in the Context of Laparoscopy*, Master Dissertation CS, University of Houston, 2015.
- [26] G. Toti, M. Garbey, V. Sherman, B. Dunkin and B. Bass, "Smart Trocar for Automatic Tool Recognition in Laparoscopic Intervention," *SURG INNOV*, vol. 22, pp. 77-82, 2015.
- [27] J. Schwartz, M. Denninger, D. Rancourt, C. Moisan and D. Laurendeau, "Modeling liver tissue properties using a non-linear visco-elastic model for surgery simulation," *Medical Image Analysis*, vol. 9, no. 2, p. 103–112, 2005.

- [28] S. o. A. G. E. S. (SAGES), "Framework for Post-Residency Surgical Education and Training—A SAGES Guideline," *Surg Endosc*, vol. 8, pp. 1137-1142, 1994.
- [29] R. Gish, T. Bui, C. Nguyen, D. Nguyen and H. Tran, "Liver disease in Viet Nam: screening, surveillance, management and education: a 5-year plan and call to action," *J Gastroenterol Hepatol*, vol. 27, pp. 238-247, 2012.
- [30] T. Langø, G. Tangen and R. Mårvik, "Navigated ultrasound in laparoscopic surgery," *Advances in Laparoscopic Surgery*, pp. 77-98, 2012.
- [31] E. Roan and K. Vemaganti, "The Nonlinear Material Properties of Liver Tissue Determined From No-Slip Uniaxial Compression Experiments," *J Biomech Eng*, vol. 129, no. 3, p. 450–456, 2007.
- [32] S. Kim, T. McCulloch and K. Rim, "Comparison of Viscoelastic Properties of the Pharyngeal Tissue: Human and Canine," *Dysphagia*, vol. 14, p. 8–16, 1999.
- [33] E. Mazza, A. Nava, M. Bauer, R. Winter, M. Bajka and A. Holzapfel, "Mechanical properties of the human uterine cervix: An in vivo study," *Medical Image Analysis*, vol. 10, no. 2, p. 125–136, 2006.
- [34] J. Kim and M. Srinivasan, "Characterization of Viscoelastic Soft Tissue Properties from In vivo Animal Experiments and Inverse FE Parameter Estimation," *Medical Image Computing and Computer Assisted Intervention*, vol. 3750, p. 599–606, 2005.
- [35] M. Ottensmeyer, "In vivo measurement of solid organ viscoelastic properties," *Medicine Meets Virtual Reality, Studies Health Technol Inform*, vol. 85, p. 328–333, 2002.
- [36] L. Huwart, F. Peeters, R. Sinkus, L. Annet and N. Salameh, "Liver fibrosis: non-invasive assessment with MR elastography," *NMR Biomed*, vol. 19, no. 2, p. 173–179, 2006.
- [37] K. Konishi, M. Nakamoto, Y. Kakeji, K. Tanoue, H. Kawanaka, S. Yamaguchi, S. Ieiri, Y. Sato, Y. Maehara, S. Tamura and M. Hashizume, "A real-time navigation system for laparoscopic surgery based on three-dimensional ultrasound using magneto-optic hybrid tracking configuration," *International Journal of Computer Assisted Radiology and Surgery*, vol. 2, no. 1, pp. 1-10, 2007.
- [38] K. Gavaghan, M. Peterhans, T. O. Santos and S. Weber, "A portable image overlay projection device for computer-," *IEEE Trans Biomed Eng*, vol. 58, p. 1855–1864, 2011.

- [39] P. Pessaux, M. Diana, L. Soler, T. Piardi, D. Mutter and J. Marescaux, "Towards cybernetic surgery: robotic and augmented reality-assisted liver segmentectomy," *Langenbecks Arch Surg*, vol. 400, p. 381–385, 2015.
- [40] S. Nicolau, L. Soler, D. Mutter and J. Marescaux, "Augmented reality in laparoscopic surgical oncology," *Surg Oncol*, vol. 20, no. 3, p. 189–201, 2011.
- [41] C. Vaopenstad, A. Rethy, T. Langø, T. Selbekk, B. Ystgaard and Hernes, "Laparoscopic ultrasound: a survey of its current and future use, requirements, and integration with navigation technology," *Surg Endosc*, vol. 24, no. 12, p. 2944–2953, 2010.
- [42] R. Shekhar, O. Dandekar, V. Bhat, M. Philip, P. Lei, C. Godinez, E. Sutton, I. George, S. Kavic, R. Mezrich and A. Park, "Live augmented reality: a new visualization method for laparoscopic surgery using continuous volumetric computed tomography," *Surg Endosc*, vol. 24, no. 8, p. 1976–1985, 2010.
- [43] H. Kenngott, I. Wegner, J. Neuhaus, F. Nickel, L. Fischer, T. Gehrig, H. Meinzer and B. Müller-Stich, "Magnetic tracking in the operation room using the da Vinci telemanipulator is feasible," *Robot Surg*, vol. 7, no. 1, p. 59–64, 2013.
- [44] B. Ma and R. Ellis, "Robust registration for computer-integrated orthopedic surgery: Laboratory validation and clinical experience," *Med. Image Anal*, vol. 7, no. 3, p. 237–250, 2003.
- [45] L. Clements, W. Chapman, B. Dawant, R. Galloway and M. Miga, "Robust surface registration using salient anatomical features for image-guided liver surgery: algorithm and validation," *Med. Phys.*, vol. 35, no. 6, p. 2528–2540, 2008.
- [46] K. H. Strobl, E. Mair, T. Bodenmüller, S. Kielhöfer, W. Sepp, M. Suppa, D. Burschka and G. Hirzinger, "The Self-Referenced DLR 3D-Modeler," in *IEEE/RSJ International Conference on Intelligent Robots and Systems*, St. Louis, 2009.
- [47] T. Rauth, P. Bao, R. Galloway, J. Bieszczad, E. Friets, D. Knaus, D. Kynor and A. Herline, "Laparoscopic surface scanning and subsurface targeting: implications for image-guided laparoscopic liver surgery," *Surgery*, vol. 142, no. 2, pp. 207–214, 2007.
- [48] G. Sirat and D. Psaltis, "Conoscopic holography," *Optics Lett.*, vol. 10, no. 1, pp. 4–6, 1985.

- [49] R. Lathrop, D. Hackworth and R. Webster, "Minimally invasive holographic surface scanning for soft-tissue image registration," *IEEE Trans. Biomed. Eng.*, vol. 57, no. 6, p. 1497–1506, 2010.
- [50] A. Hostettler, S. Nicolau, Y. Remond, J. Marescaux and L. Soler, "A real-time predictive simulation of abdominal viscera positions during quiet free breathing," *Prog Biophys Mol Biol*, vol. 103, pp. 169-184, 2010.
- [51] F. Tatar, J. Mollinger and A. Bossche, "Ultrasound system for measuring position and orientation of laparoscopic surgery tools," *Proceedings of IEEE*, vol. 2, pp. 98 -990, 2003.
- [52] F. Tatar, J. Mollinger, J. Bastemeijer and A. Bossche, "Time of flight technique used for measuring position and orientation of laparoscopic surgery tools," *Proceedings of IEEE*, vol. 3, pp. 1480-1483, 2004.
- [53] K. Ikuta, T. Kato, H. Ooe and S. Ando, "'Surgery recorder system' for recording position and force of forceps during laparoscopic surgery," in *Advanced intelligent mechatronics 2007 IEEE/ASME international conference*, 2007.
- [54] M. I. Miga, P. Dumpurib, A. L. Simpsona, J. A. Weisa and W. R. Jarnaginc, "Model-Assisted Image-Guided Liver Surgery Using Sparse Intraoperative Data," *Soft tissue Biomechanical Modeling for Computer Assisted Surgery*, pp. 7-40, 2012.
- [55] J.-C. Yuan, "A general photogrammetric method for determining object position and orientation," *IEEE Transactions on Robotics and Automation*, vol. 5, no. 2, pp. 129-142, 1989.
- [56] H.-C. Hur, D. Arden, L. E. Dodge, B. Zheng and H. A. Ricciotti, "Fundamentals of Laparoscopic Surgery: A Surgical Skills Assessment Tool in Gynecology," *JSLs*, vol. 15, no. 1, p. 21–26, 2011.
- [57] R. Case, J.-J. Sonke, D. Moseley, J. Kim, K. Brock and L. Dawson, "Inter- and intrafraction variability in liver position in non-breath-hold stereotactic body radiotherapy," *Int J Radiat Oncol Biol Phys*, vol. 75, no. 1, p. 302–308, 2009.
- [58] A. Khamene, J. Warzelhan, S. Vogt, D. Elgort, C. Ched'Hotel, J. Duerk, J. Lewin, F. Wacker and F. Sauer, "Characterization of internal organ motion using skin marker positions," *MICCAI*, vol. 90, p. 526–533, 2004.
- [59] D. Yang, W. Lu, D. Low, J. Deasy, A. Hope and N. I. El, "4d-ct motion estimation using deformable image registration and 5d respiratory motion modeling," *Med. Phys.*, vol. 35, no. 10, p. 4577–4590, 2008.

- [60] H. Fayad, T. Pan, O. Pradier and D. Visvikis, "Patient specific respiratory motion modeling using a 3d patient's external surface," *Medical Physics*, vol. 36, no. 6, p. 386–3395, 2012.
- [61] A. Sahih, O. Haas, K. Burnham and J. Mills, "Organ motion modelling and prediction for adaptive radiotherapy," *Proceeding IAR-ACD*, vol. 2, no. 89, p. 211–216, 2005.
- [62] V. Rajagopal, "Modelling Breast Tissue Mechanics Under Gravity Loading," The University of Auckland, 2007.